Universidade do Minho
Escola de Engenharia

Pedro Manuel de Lima Gomes Caldelas

Production and characterisation of composites materials based on Ge nanoparticles-doped dielectric layer

Junho de 2009

Universidade do Minho
Escola de Engenharia

Pedro Manuel de Lima Gomes Caldelas

Production and characterisation of composites materials based on Ge nanoparticles-doped dielectric layer

Tese de Mestrado
Processamento e Caracterização de Materiais

Trabalho efectuado sob a orientação da
Professora Doutora Maria Jesus Matos Gomes
e da
Professora Doutora Ana Maria Pires Pinto

Junho de 2009

Universidade do Minho, ___/___/_____

Assinatura: _____

Universidade do Minho
Escola de Engenharia

Pedro Manuel de Lima Gomes Caldelas

Production and characterisation of composites materials based on Ge nanoparticles-doped dielectric layer

Tese de Mestrado
Processamento e Caracterização de Materiais

Trabalho efectuado sob a orientação da
Professora Doutora Maria Jesus Matos Gomes
e da
Professora Doutora Ana Maria Pires Pinto

Junho de 09

É AUTORIZADA A REPRODUÇÃO INTEGRAL DESTA TESE/TRABALHO APENAS PARA EFEITOS DE INVESTIGAÇÃO, MEDIANTE DECLARAÇÃO ESCRITA DO INTERESSADO, QUE A TAL SE COMPROMETE.

Universidade do Minho, _____/ _____/ _____

_____

(Pedro Manuel de Lima Gomes Caldelas)

Acknowledgments

Many persons had, somehow, contributed to this work. First of all, I have to thank Prof.ª Maria de Jesus Gomes for the close supervision and Prof.ª Ana Pinto for all the help and guidance whenever required. Several other researchers colleagues and Professors working at the Physics Department of University of Minho also gave their contribute. I must not forget to thank Prof.ª Anabela Rolo for the all-fruitful discussions and help in performing the Raman measurements, as well as Dr. Adil Chahboun for the help in performing the photo-luminescence measurements and their results interpretation. Other people like Anatoly Khodorov, Carlos Batista, Sara Pinto, Sergey Levichev, and Prof. Mário Pereira must also be mentioned. It was a true pleaser to have the opportunity of working, discussing and fraternize with all of you.

Others, from outside the University of Minho, have also contributed to this work in performing several characterisation techniques not available at home. Their efforts are equality thankful and, because of that, their names are mentioned along the text when presenting each of the characterisation techniques on which they were involved.

Last but not least, I would like to address my special thanks to my wife Paula for all her support and understanding during all this time, and to dedicate this dissertation to my adorable baby daughter Sara, which has inspired me and gave me the strength to be able to complete it.

Abstract

**Production and characterisation of composites materials
based on Ge nanoparticles-doped dielectric layer**

The main goal of this project was the processing and structural, chemical and optical characterisation of nanocomposite thin film Germanium (Ge) semiconductor nanoparticles (NPs) embedded in Alumina (Al_2O_3) layer. Such type of materials structures has several potential applications, mainly in electronics and optoelectronic devices like it is the case of memory or light emitting devices (LED's). Stand-alone Alumina films were initially produced and studied as the reference starting point.

The nanocomposite were produced by *RF*-magnetron sputtering technique. A significant number of characterisation techniques were used in order to evaluate the nanocomposite properties, namely X-ray diffraction (XRD), Raman scattering, scanning and transmission electron microscopy (SEM and TEM), Rutherford backscattering spectroscopy (RBS), and photoluminescence (PL).

The results and discussion, based on the particular findings revealed by the detailed analysis of all data from each characterisation technique, are presented cautiously. The study of the deposition and annealing parameters led to processing parameters optimization. The ability to (re)produce such type of materials structures is discussed. The conclusions are presented in a concise way. Ultimately, some light emission that might be related to excitonic recombination in the Germanium nanocrystals was observed during PL measurements. The temperature dependence of the PL demonstrates the confinement effect.

Resumo

**Produção e caracterização de materiais compósitos baseados
em matriz dieléctrica dopada com nanopartículas de Ge**

Este trabalho teve como objectivo o processamento e a caracterização estrutural, química e óptica de filmes finos de nanocompósitos de Alumina com nanopartículas de Germânio. Estes materiais possuem várias potenciais aplicações, sobretudo em dispositivos electrónicos e opto-electrónicos como são o caso de dispositivos de memória ou emissores de luz (vulgarmente denominados *LED´s*). Filmes de Alumina foram inicialmente estudados para servirem como ponto inicial de referência.

Os filmes de nanocompósitos foram produzidos por pulverização catódica em magnetrão por rádio frequência (*RF*-magnetron sputtering). A avaliação das propriedades dos filmes foi efectuada recorrendo a diversas técnicas de carcaterização, nomeadamente difracção de Raios-X (*XRD*), difusão *Raman*, espectroscopia electrónica de varrimento e de transmissão (*SEM* e *TEM*), espectroscopia de retrodispersão de *Rutherford* (*RBS*), e fotoluminescência (*PL*).

Os resultados e a discussão, baseados nas conclusões individuais reveladas pela análise detalhada de todos os dados provenientes de cada técnica de caracterização, são apresentados de forma prudente. Os parâmetros de deposição e recozimento para a produção dos materiais nanocompósitos foram estudados e optimizados. A capacidade de (re)produzir tais estruturas de materiais é discutida. As conclusões são apresentadas de forma concisa. No final, os resultados de PL revelaram uma emissão de luz que poderá estar associada à recombinação excitónica dos nanocristais de Germânio. A dependência da temperatura do PL demonstra o efeito de confinamento quântico.

Index

List of abbreviations and acronyms

A – Optical **A**bsorbance or Optical density

a-Ge – **A**morphous **Ge**rmanium

c-Ge – **C**rystalline **Ge**rmanium

DOS – **D**ensity of **S**tates

FS – **F**used **S**ilica

GIXRD – **G**lancing-angle **I**ncidence **X-r**ay **D**iffraction

HRTEM – **H**igh **R**esolution **T**ransmission **E**lectron **M**icroscopy

MIS – **M**etal–**I**nsulator–**S**emiconductor

NCs – **N**ano**c**rystal**s**

NPs – **N**ano**p**article**s**

PL – **P**hoto**l**uminescence

PLE – **P**hoto**l**uminescence **E**xcitation

QDs – **Q**uantum **D**ots

R – Annealed (from the Portuguese word "**R**ecozida")

RBS – **R**utherford **B**ackscattering **S**pectrometry

RF – **R**adio **F**requency

RT – **R**oom **T**emperature

SAD – **S**elected **A**rea **D**iffraction

sccm – **s**tandard **c**ubic **c**entimetres per **m**inute

SEM – **S**canning **E**lectron **M**icroscopy

TEM – **T**ransmission **E**lectron **M**icroscopy

XPS – **X**-ray **P**hotoelectron **S**pectroscopy

XRD – **X-r**ay **D**iffraction

List of symbols

λ – mean free path

$\varPhi$ – magnetic flux

β_{FWHM} – full width at half maximum (*FWHM*) of the diffraction peak

B – magnetic field

d – thickness

D – mean diameter

ε – dielectric constant

k – extinction coefficient

n – refractive index

p – pressure

p_{Ar} – Argon pressure

P – power

P_{RF} – radio-frequency sputtering power

t – time

T_{dep} – deposition temperature

T_a – annealing temperature

v – volume

List of figures

Chapter 1

Fig.1.1 – Schematic showing the main procedural differences in films deposited by PVD or CVD: (a) conformity or uniformity, and (b) directionality.

Fig.1.2 – (a) Atomic interaction in the sputtering target, taken from [13]; (b) Basic schematic of the inside of a vacuum chamber showing the sputtering process.

Fig.1.3 – Draft of a generic rectangular planar magnetron showing (a) its quasi-rectangular sputter erosion track formed inside the magnetic field lines and (b) the cross section view taken through the plane B-B' showing: 1-nonmagnetic metal case, 2-insulater, 3-magnetizable rear yoke, 4-permanent magnets, and 5-magnetizable pole pieces. In (b), the vacuum seals and the cooling water channels are omitted for simplicity. Adapted from [15].

Fig.1.4 – Cross section draft of the field pattern produced by (a) a rectangular planar magnetron with balanced field and (b) a circular planar magnetron with unbalanced field, both having a matched set of magnets. Reproduced from [15].

Fig.1.5 – Helical orbit executed by an electron leaving the target in the presence of a magnetic field *B*.

Chapter 2

Fig.2.1 – The Alcatel SCM650 apparatus at the Thin Films Laboratory.

Fig.2.2 – Overall block diagram of the vacuum pumping system associated to the Alcatel SCM650 apparatus. Adapted from [25].

Fig.2.3 – Simplified schematic of the inside view of the vacuum chamber. Adapted from [25].

Fig.2.4 – Schematic cross-section view of the magnetron structure showing the Al_2O_3 target and anode plate properly mounted. (Note that relative dimensions are not in scale).

Fig.2.5 – Description of the three target configurations in terms of quantity and positioning of the Ge pieces placed on top of the alumina target.

Fig.2.6 – Schematic showing the placement of the samples-holder over the target (a) and criteria numbering established to label the samples of each series regarding their positioning on the holder.

Fig.2.7 – Annealing system used: (a) oven, (b) thermocouple, (c) temperature controller, (d) quartz tube, (e) gas lines, (f) rotary pump, (g) diffusion pump and (h) pressure gauges.

Fig.2.8 – Experimental annealing ramp obtained for the 800ºC/1hour annealing processes.

Fig.2.9 – Schematic representation of an X-ray diffraction measurement made with Bragg-Brentano geometry.

Fig.2.10 – Schematic representation of the system used in the Raman scattering measurements (microanalysis set up in backscattering geometry).

Chapter 3

Chapter 1
Introduction

1. Introduction

1.1   Importance of the research area

1.1.1 Semiconductor Nanocrystals, properties and applications

Semiconductor nanocrystals (NCs), sometimes also called quantum dots (QDs), are very small crystalline semiconductor material which contain tens or a few hundred atoms with sizes of a few nanometres. The term nanoparticles (NPs) is also frequently used when referring to materials at the nanometre scale. The first realization of QDs was linked to the inclusion of nano-size Cadmium Selenide (CdSe) and Cadmium Sulphide (CdS) semiconductors in glasses [1]. Such red or yellow coloured glasses have been commercially available as colour filters for decades. In 1985 Ekimov et al. [2] experimentally proved and theoretically modelled that these changes in colour were linked to the density of states (DOS) determined by the size of the crystalline material. Below a certain size, the properties of the crystalline material start to deviate significantly from bulk properties and strongly dependent on size. Finite size of the micro crystallites confines the motion of the *quasiparticles* (electron, hole and exciton) within its physical boundary. This is called *quantum confinement*. *Quantum confinement* modifies the DOS, which in turn leads to discretisation as well as enlarged spacing between the energy levels of electron and hole states. Thus one can observe an increase in the band gap as the optical absorption onset occurs at higher energies (*blue-shift*) in the case NCs.

Since a long period of time, most research effort concentrates on QDs made of III-V compound semiconductors having direct band gap. Due to the indirect optical transition properties of group IV materials, less interest has been paid on bulk Silicon (Si) or Germanium (Ge) semiconductor materials in that their light emission efficiency is not good enough for optoelectronic applications [3]. However, visible photoluminescence (PL) from Si quantum structures is reported in several works. Yet, bulk Ge has a larger dielectric constant and smaller carrier masses compared to bulk Si, leading to a larger Bohr radius (24.3nm) than that of bulk Si. Moreover, in Ge, the direct gap ($E_0 \sim 0.88$eV) is close to the direct gap ($E_g \sim 0.75$eV). Then, it is considered that *quantum confinement* effects would appear more pronounced in Ge than in Si, and Ge NCs would exhibit a direct-gap semiconductor nature

[4]. Therefore, Ge NCs would be easier to change in terms of electronic structure around the band gap, making them attractive for potential applications after all [3]. In fact, it was suggested that when the size of an indirect gap semiconductor is reduced to few nanometers, the NC starts to resemble to a direct gap material. Thus electrons and holes can be independently confined into the infinite spherical potential [5]. The lowest energy of the electron-hole pair E_1 could be obtained, as a first approximation, by Kayanuma model [6]:

$$E_1 = E_g + (\frac{\pi^2 \cdot \hbar^2}{2 \cdot \mu \cdot R^2}) - 1.786 \frac{e^2}{\kappa R} - 0.248 E_{Ry}^*, \qquad (1.1)$$

where *Eg* is the optical band gap of bulk crystalline Ge, μ is the reduced mass, $\hbar$ is the reduced Planck constant, and E_{Ry}^* the effective Rydberg energy. In this model, the nanocrystals are assumed to be spherical with sphere radius *R* and dielectric constant *k*.

Nowadays, and during the last two decades or so, huge scientific interests and progresses in understanding these NCs contributed to the new branch of science known as *Nanoscience*. In short words, as a result of the *quantum confinement* effects the emission colour of semiconductor NCs can be dramatically modified by simply changing their size [7]. This fact is the main reason why they have been studied as having high potential for possible applications over different fields of science: ultra sensitive, multicolour and multiplexing applications in molecular biotechnology and bioengineering; device fabrication like lasers, large area photovoltaic thin-films or light-emitting devices (LEDs); quantum optical applications including quantum cryptography and quantum computation; optoelectronic and signal processing; etc… . Among devices for optoelectronic and nano-electronic, the use of Metal–Insulator–Semiconductor (MIS)[1] structures using Si and Ge semiconductor NCs have also been reported to show good memory effects and low power operation at room temperature [8]. In fact, one of the most common structures used for memory or LED purposes is the metal or poly-Si/SiO$_x$/Si structure with Si NCs embedded in the SiO$_x$ layer. However, alumina[2] or stacked dielectrics are also used as dielectric matrix, and Ge and SiGe nanocrystals are also often formed inside those matrices [9] and [10]. Still, in most of the works found on the literature the nanocrystals have been grown inside a SiO$_2$ matrix.

It is clear, however, that for different applications, NCs are to be embedded in different matrices. Exploiting their potential applications, it is necessary to have a better understanding

---

[1] More commonly mentioned term is Metal-Oxide-Semiconductor (MOS), which are a type of MIS structures.
[2] Alumina, the commercial term used when referring to Aluminium Oxide (Al$_2$O$_3$).

on how the properties of the NCs are influenced by different environments. Some results showed that MOS capacitors with Al_2O_3 dielectric exhibit sensitivity greater than that obtained from MOS capacitors with SiO_2. This higher sensitivity is attributed to higher trapping efficiency in the Al_2O_3.

Constant shrinking of the thickness of gate dielectrics to below 2-3 nm has also led to a search for alternative materials, whose dielectric constant is higher than that of SiO_2, but whose other properties remain similar to SiO_2. Because of its similar band gap (9eV) and more than twice as high dielectric constant (ε_{Al2O3}=9 and ε_{SiO2}=3.9), Al_2O_3 is a good candidate to replace SiO_2 as a gate dielectric material and is starting to be used in today's modern electronic technology. At the same time Al_2O_3 presents good mechanical properties, which leads it to be, at least in theory, an ideal material for Si processing conditions [11] and [10]. After deposition, the final step of the production of such kind of structures containing NCs consists of an annealing process. This is, perhaps, the more effective way to change and control the size of the semiconductors NCs embedded in their dielectric matrices.

1.1.2 Scope of the Thesis

The first objective of the research work that has led to this thesis was to be able to produce composite films based on Ge nanoparticles-doped dielectric layer. The full characterisation of those produced structures and the results interpretation, both from the structural and the optical properties points of view, was the second goal of this work. Being mostly a practical work, no focus is given herein to theoretical formulations related with confinement regimes or density of states, for instance. Conclusions reflect almost exclusively the characterisation results and observations, rather than hypothesis formulation based on semiconductor theory.

By the end of the dissertation, the interpretation study of all the results and experiments that were carried out will, hopefully, be a useful reference contributing to further works in this field of knowledge.

1.2   PVD versus CVD processes

Thin films can be produced using a panoply of different techniques based on PVD (Physical Vapour Deposition) or CVD (Chemical Vapour Deposition) processes. In a very simple way, one can distinguish PVD from CVD by saying that PVD processes consist on a material release (either by vaporisation or sputtering) from a source (target) and its transference into a certain surface (substrate) to form what is called a thin film, while in CVD processes the film formation involves a chemical reaction that takes place inside a reactor to which one or more gases must be supplied.

There are several different techniques based on both processes (Table 1.1) that can be more or less complex and expensive, and more or less effective, in producing thin films for a certain type of application.

Table 1.1 – Some techniques based on PVD and CVD processes.

PVD	CVD
− DC-Glow Discharge Sputtering	− High Density Plasma CVD
− Evaporation (resistance, induction, e-beam)	− Hot-wire CVD
− Ion implantation	− LPCVD – Low Pressure CVD
− MBE – Molecular Beam Epitaxy	− MOCVD – Metal Organic CVD
− PLD – Pulsed Laser Deposition	− PECVD – Plasma Enhanced CVD
− RF Sputtering	

Choosing the most efficient technique to reach a certain goal can be a difficult task. Nevertheless, there are some consensual general differences that we can say for sure about films produced either by PVD or CVD processes. Among those differences, two of the more relevant ones are related to conformity and directionality as shown in Fig.1.1. In PVD, the film deposition is a highly directional process mainly perpendicular to the target. If the surface of the part that is to be covered is very far from being parallel to the target, and/or if that part has some kind of cavities or holes, most probably the process will not be very efficient. However, PVD is a very effective process if the substrate is flat and placed parallel to the target. A chemical vapour deposition is a much more multidirectional and conformal process than a PVD one. So, thickness homogeneity on irregular shape or non-parallel to the target substrates can be achieved in a much more effective way using CVD. Another consensual and considerable point is that, in general, a CVD technique involves much higher

risks and costs than PVD techniques due to the necessary use of the gaseous materials. Some of these gases can be very dangerous to health. This is, of course, a big disadvantage of CVD when compared to PVD techniques.
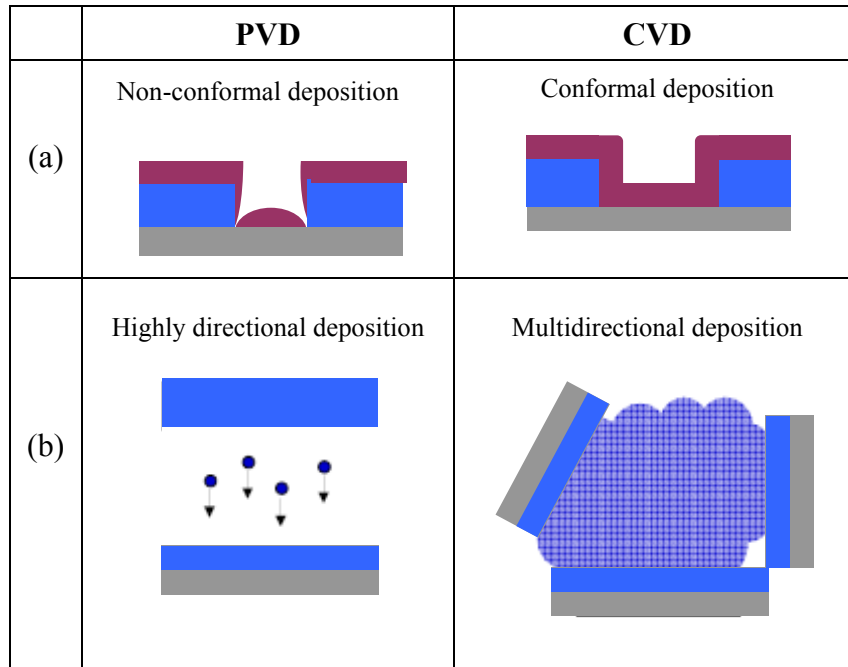
	PVD	CVD
(a)	Non-conformal deposition	Conformal deposition
(b)	Highly directional deposition	Multidirectional deposition

Fig.1.1 – Schematic showing the main procedural differences in films deposited by PVD or CVD: (a) conformity or uniformity, and (b) directionality.

1.3   Sputtering

Sputtering process is well known and one of the most commonly used methods for the deposition of thin films. It is widely used in the automotive, photovoltaic, recording and semiconductor industries. High melting point materials like ceramics and refractory metals, which are difficult to deposit by evaporation, are easily deposited using sputtering. Sputtering techniques range from a simple *dc* glow discharge sputtering which is limited to the sputtering of conductive targets, to *RF* sputtering where any target regardless of its conductivity can be sputtered, and to a more sophisticated ion beam sputtering (*IBS*) in which very well controlled deposition of material is possible [12].

The verb to *sputter* originates from Latin *sputare* (to emit saliva with noise). The phenomenon was first described about 150 years ago by Grove (1852) and Plücker (1858), who reported vaporization and film formation of metal films by sputtering . Sputtering usually

takes place at low pressure inside a vacuum chamber when the target (and cathode, a solid material plate) is "bombard" by atoms or ions that collide with it at a certain velocity (kinetic energy). These collisions and momentum transfer from the incoming particles cause the ejection of atoms and secondary electrons (Fig.1.2 (a)), starting a continuous erosion process in the superficial area of the target. In this area it is possible to observe a glow discharge, or plasma, which is a fluid of positive ions and electrons in a quasi-neutral electrical state [13].

In spite of being a highly directional process, all the atoms and secondary electrons released from the target in the sputtering process fly away from it in every direction and with different energies. The sputtered atoms (or atom clusters) that are "extracted" with enough kinetic energy will be deposited on the substrate placed in front of the target (Fig.1.2 (b)). The secondary electrons are accelerated and could originate new gas ions by colliding with new gas atoms, making possible the sustainability of the sputtering process. As we will see further on, a magnetron can increase the efficiency of this process.
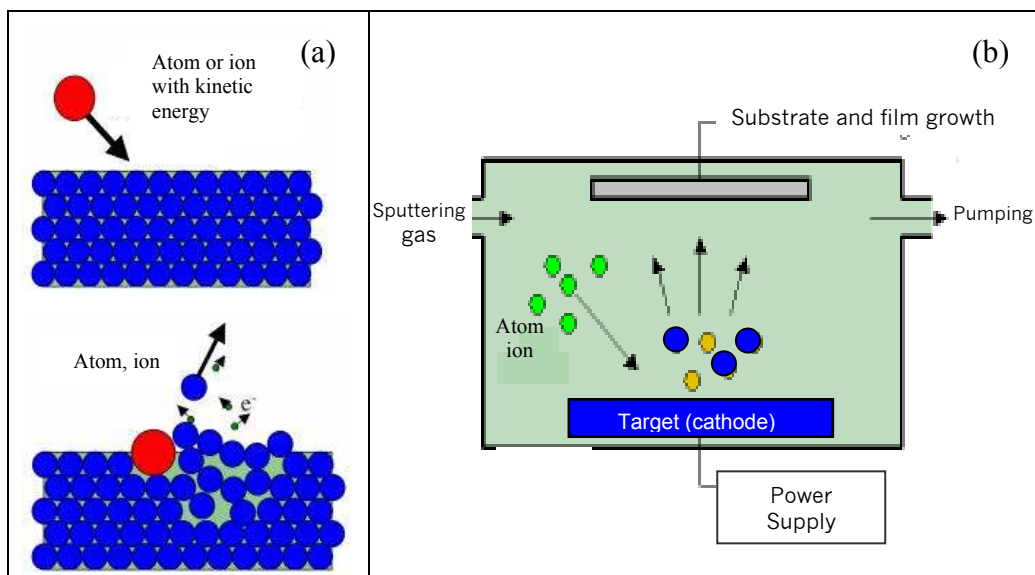
Fig.1.2 – (a) Atomic interaction in the sputtering target, taken from [13]; (b) Basic schematic of the inside of a vacuum chamber showing the sputtering process.

The number of target atoms being deposited on the substrate per unit of time is associated with the *deposition rate* value of the film, usually expressed in nm.min⁻¹. Considering the *kinetic theory of gases*, and knowing the values of the pressure (p) and temperature (T) of the sputtering gas inside the volume (v) of the chamber, it is possible to determine the number of particles per unit of volume (n_v) inside the chamber. This allows us to calculate

the average distance between collisions for a gas molecule, known as *mean free path* (λ), by using the simple expression $\left(\lambda = \sqrt{2}n_v\sigma\right)^{-1}$, where σ is the effective cross sectional area for collision that is equal to πd^2, being d the molecule diameter [14].

So, as we saw, at least one type of sputtering gas (usually inert and with heavy atoms, like Argon or Xenon) must be introduced inside the chamber in order that the sputtering process can be started. Part of the atoms of the gas being used, let say Argon, becomes ionized (Ar^+) by exchanging electrons with its surroundings, usually after a short thermo electronic discharge inside the chamber. If other not inert gas like oxygen is used, the process is called "reactive sputtering". Atoms of these gases will react with all the surfaces inside the chamber including, and most important, the film material(s) that are being deposited on the substrate surface. Some compounds different from the target(s) material(s) can be obtained in this way.

In the traditional sputtering process, a negative *dc* current is usually applied to the target(s) being used, which must be a conductor material. However, if the material we want to sputter is not a good conductor, it could not be used as an electrode because, in this case, positive charges will start accumulating on top of the target. After some time, the accumulation of charges would prevent the sputtering process to continue, since the gas ions inside the chamber will be repulsed from the target instead of being attracted to it. Changing the dc power supply by an ac power supply, able to deliver an alternating current polarisation to the target, can solve this problem. The frequency of this current is typically in the range of 5 to 30 MHz (radio-frequency, *RF*), being 13.56MHz one of the most used nowadays. During the negative cycle of the alternating polarisation of the target ions are attracted to the cathode (target) and sputtering occurs, while in the positive cycle only the electrons are attracted to the target and the electrical potential equilibrium is maintained, since the possible positive charge accumulation during the negative cycle can now be cancelled.

1.4   Magnetron sputtering

The magnetron sputtering is a more recent and clever way to increase the efficiency of the sputtering process by placing the target onto a magnetron with the appropriate geometry. We can describe a magnetron as a solid metallic structure in which a certain number of permanent magnets are placed and distributed in such a way that a magnetic field can be created around

them. The purpose of using a magnetic field is to make more efficient use of the electrons and cause them to produce more ionisation.

Based on reference [15], the first magnetron discharge device employing cylindrical-hollow cathodes with in-turned end flanges appeared in a 1936 article by F. M. Penning. The use of end flanges was a crucial development because it made possible the electrostatic containment of the plasma. At that time, when fitting his volt-ampere curve to an equation of the type $I \propto V^n$, a voltage index n of 6.5 was obtained. A few years later, and also based on reference [15], Penning and Moubis were able to reduce this value to 6, after communicating the first magnetron glow discharge device employing a cylindrical-post cathode with out-turned end flanges in 1939. Depending on design details, typical present day magnetrons have a voltage index which lies in the range 5 to 10. In the late 1960s and early 1970s, approximately thirty years after Penning's 1939 sputtering work, the surge in sputter magnetron development resulted in the recognition of three generic types of sputter magnetrons: conical magnetrons, cylindrical magnetrons and planar magnetrons [15]. Within each type there may be big variations of design. In particular, the planar magnetron designation includes devices in which the sputter erosion track is circular, square, rectangular, or oval (race-track like). Besides its shape, there may be a single erosion track or a nested series of tracks. At Fig.1.3 it is possible to see a draft of a simple planar magnetron (a) and its cross-section taken through the plane B-B' (b), including the connections to a power supply and the typical positioning of the substrate over the sputter target. The white dotted line in (b) indicates the original cathode (target) surface while the solid contours indicate the profile, which develops after a long period of sputter erosion.

An assembly of permanent magnets putted together inside a case produces the magnetic field in a "magnetron". The magnets arrangement, typically an outside ring of magnets and an inside central cylindrical magnet with inverted magnetization, are in such a way that the field lines emerge from, arch over, and re-enter the sputter target plate. The case is connected to ground potential and functions as the anode of the discharge. The plasma is mainly formed in the tunnel defined by the field line arches.
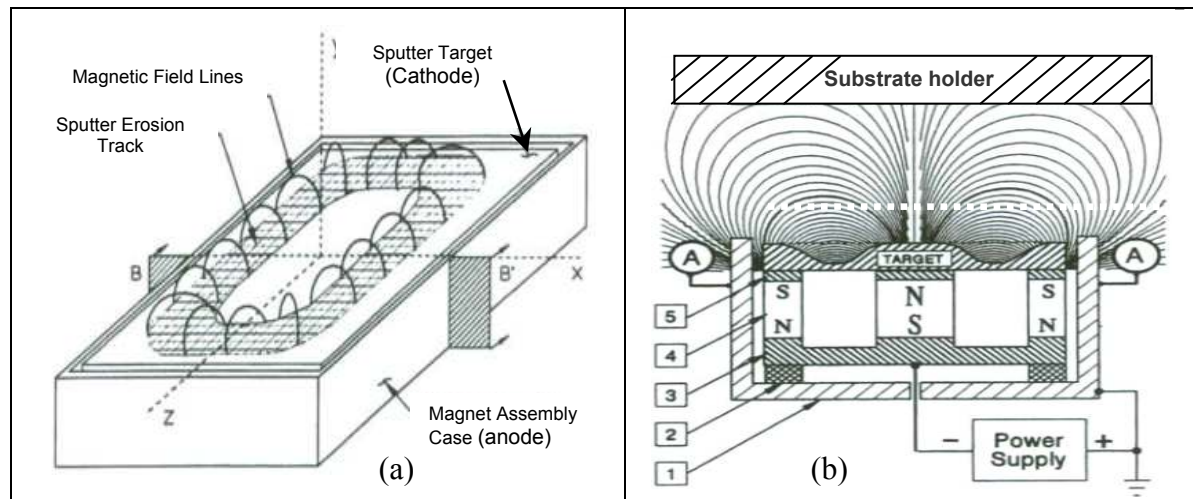
Fig.1.3 – Draft of a generic rectangular planar magnetron showing (a) its quasi-rectangular sputter erosion track formed inside the magnetic field lines and (b) the cross section view taken through the plane B-B' showing: 1-nonmagnetic metal case, 2-insulater, 3-magnetizable rear yoke, 4-permanent magnets, and 5-magnetizable pole pieces. In (b), the vacuum seals and the cooling water channels are omitted for simplicity. Adapted from [15].

1.4.1 Balanced vs unbalanced magnetron fields

In Fig.1.4 (a) the same field of Fig.1.3 (b) rotated through 90º is shown. All the field lines that emanate from the central "north pole" are collected by the outlying south poles. The magnetic flux (ϕ) is zero on the plane of symmetry. This magnetron has a "balanced" field.
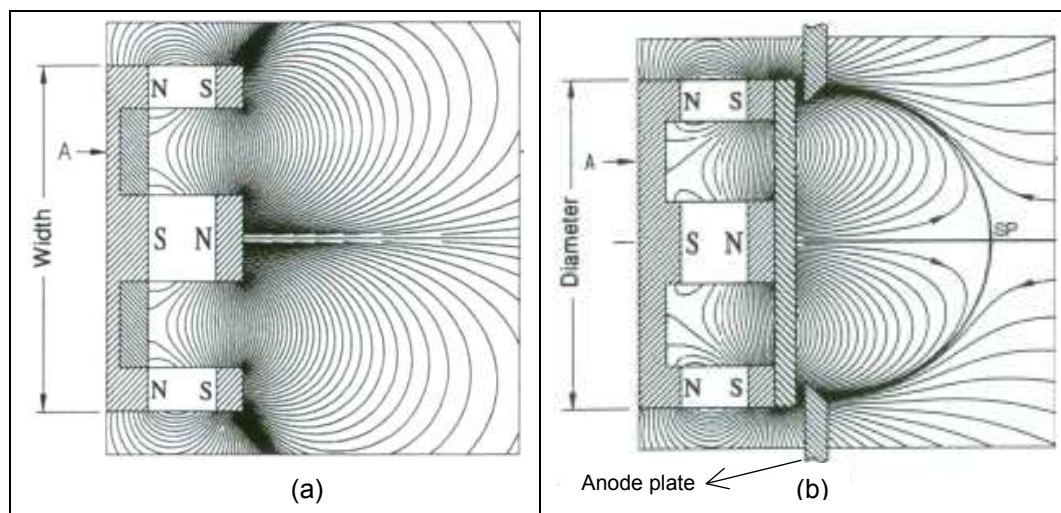
Fig.1.4 – Cross section draft of the field pattern produced by (a) a rectangular planar magnetron with balanced field and (b) a circular planar magnetron with unbalanced field, both having a matched set of magnets. Reproduced from [15].

Fig.1.4 (b) represents the field pattern produced by the same matched set of magnets but in the case when the system has rotational symmetry. It is possible to see that the differences between the two cases of Fig.1.4 are quite remarkable. The zero-flux contour has become almost circular, resulting in the creation of a saddle point (marked *SP* in Fig.1.4 (b)) located approximately at one-half the cathode diameter in front of the cathode. This magnetron has an "unbalanced" field.

In a system like the one of the Fig.1.4 (b), the behaviour of the plasma highly depends on the presence of the anode plate. Namely, it depends on the value of its inner diameter. If the anode plate is dimensioned and placed like shown on Fig.1.4 (b) the migration of plasma beyond the zero-flux line will be largely suppressed. However, if the anode plate presents a inner diameter value bigger than the diameter of the zero flux contour line then the moderate-to-low energy electrons escaping from the cathode magnetic trap will be able to execute helical orbits around field lines which guide them far downstream from the cathode [15]. Anyway, and providing it does not suffer any collision, an electron describing a circular motion around a magnetic field *B* (see Fig.1.5) is compelled to travel a much bigger distance before reaching the cathode surface again, enlarging the probability of ionisation of the sputtering gas and, in this way, increasing the efficiency of the sputtering process.
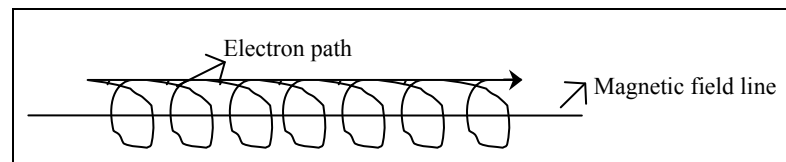
Fig.1.5 – Helical orbit executed by an electron leaving the target in the presence of a magnetic field *B*.

1.5   Annealing heat treatment

The production of most of the films included a post-deposition thermal treatment: the annealing treatment. This heat treatment annealing process is very common and applied in the nucleation and/or size increase of NCs or nanoparticles (NP's), even if they are inside some kind of matrix. It is, probably, the most important and effective method to control the NCs size. Independently of the production technique, several authors report different post-deposition annealing conditions (atmosphere and temperature) in order to control the nucleation and/or growth of semiconductor NCs embedded in dielectric matrixes. Some used

a rapid thermal annealing (*RTA*) system, others a more conventional furnace system. The differences between these two kinds of annealing systems mainly relays on the annealing time, which, in comparison with the conventional systems, can be very much reduced using an *RTA* system. In both cases, however, the main goal prevails: nucleation and/or growth of NCs. Nevertheless, it may be interesting to say that, based on experience, if not all the necessary cares are taken in order to eliminate high temperature gradient and/or if the adhesion between the film and the substrate is not as good as it should be, annealing on an *RTA* system can provoke the peeling of the film due to the stress induced by thermal shock.

Even if considering only Ge embedded both in silica (SiO_2) or alumina (Al_2O_3) dielectric materials, a lot of works can be found mentioning annealing as a crucial step for the NCs formation ([11], [16], [17]).

Germanium bulk material has a melting point of approximately 937ºC, a density of 5.32 g/cc, and a cubic structure (diamond like). Aluminium oxide, α-alumina, has a much higher melting point (around 2054ºC), a density of 3.96 g/cc, and a rhombohedral crystalline structure (Corundum). However, crystalline alumina presents five more different polymorphs (or crystalline phases). Besides the alpha (α) phase, also gamma (γ), kappa (k), theta (θ), delta (δ) and sigma (σ) phases exist, but it is α-alumina who has the best thermo-mechanical properties. More complete data sheets, including the physical, mechanical, electrical, thermal, and optical properties of alumina, germanium, and also silicon and silica materials are presented in Annex I.

The kind of substrate used to grow the films can some times limit the annealing temperature (T_a). If a normal glass substrate is used, let say microscope slides for instance, the usual annealing temperature will be limited to approximately 500-550ºC [11]. Above this value, the glass will start to soften. Annealing under temperatures in the range of 700 to 900ºC are the most reported as being suitable for the formation/grow of Ge NCs embedded in a dielectric film. This implies that films must be deposited over a substrate material that can stand higher temperatures, clearly above the Ge melting point. Not only because of this, but mostly due to technological reasons, silicon substrates are probably the most used ones to grow this kind of films (Si melting point=1412ºC). It was reported that Ge NCs embedded in sapphire melt at 955±15ºC [18], a value which is a little bit above the Ge melting point. The annealing time (t_a), which is the time during which the samples are kept at the T_a, is another important factor that needs to be controlled during the annealing process. It can usually vary

from a few minutes to several hours. Different kind of atmospheres including Nitrogen (N_2) ([19]), a mixture of Hydrogen and Argon (H_2+Ar) ([20] and [21]), Argon ([16] and [22]), or clean air, both at low ([23] and [24]) or atmospheric pressure [11] are also used in the annealing process of Ge embedded in dielectric matrix. The exact pressure value of the annealing atmospheres is usually not mentioned in the bibliography, although it seems more or less obvious, at least for me, that it must be also controlled as an important parameter. Independently of the kind of system, furnace, and related accessories available to perform the annealing (thermocouple, pumping equipment, gas lines, etc.), all these parameters (temperature, pressure, atmosphere, and annealing time) can influence a certain annealing result and should be controlled during the annealing process.

Chapter 2
Experimental procedures

2. Experimental procedures

2.1   Materials production

The production of the composite materials based on Ge nanoparticles-doped dielectric layer includes the films growth and the annealing processes. Both were done in *LFF-Laboratório de Filmes Finos* (Thin Films Laboratory), at the Physics Department of University of Minho in Braga.

2.1.1 Films growth

Films growth was based on PVD (Physical Vapour Deposition) processes. Samples were prepared by *RF*-magnetron co-sputtering technique on an Alcatel SCM650 apparatus. Co-sputtering is synonymous of more than one material being sputtered simultaneously, meaning that more than one material was used as targets at the same time, as described below. In short, the Alcatel apparatus shown in Fig.2.1 is composed of a chamber, a vacuum system, power supplies and controllers/matching boxes, and an automatic control system that allows the setting of parameters like temperature, deposition time, sample-holder positioning/rotation (including substrate to target distance), gas fluxes, etc.

Fig.2.1 – The Alcatel SCM650 apparatus at the Thin Films Laboratory. From the right to the left:

   1. Main block with deposition chamber (1.1), load-lock or pre-vacuum chamber (1.2), pumping system (1.3) and matching boxes (1.4);

   2. Control panels cabinet;

   3. Power supplies cabinet.

Fig.2.2 shows an overall block diagram of the vacuum pumping system and in Fig.2.3 a schematic of the inside of the vacuum chamber is shown.
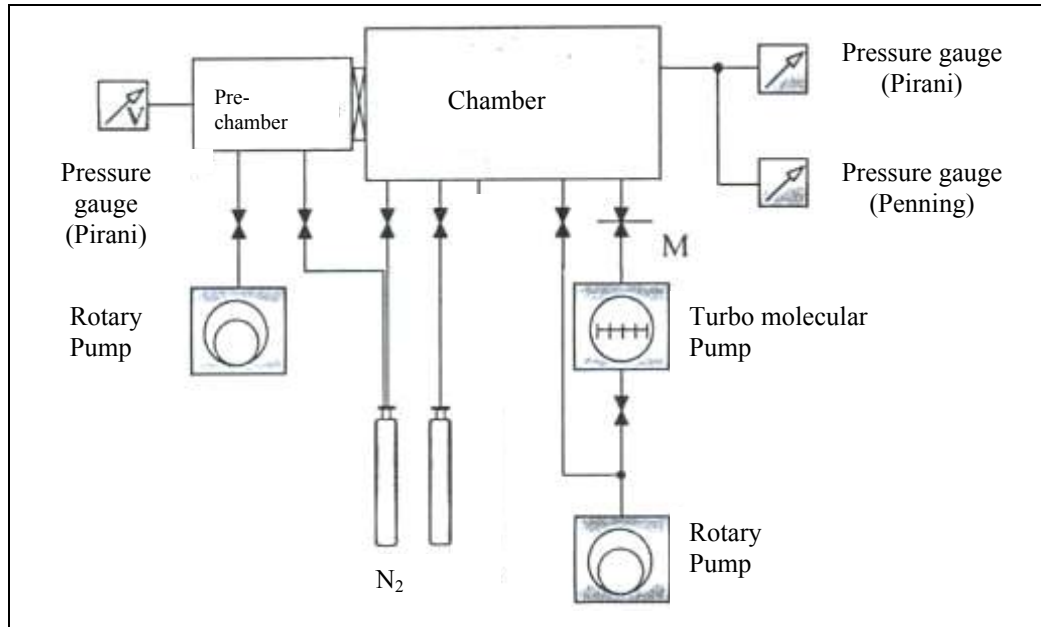
Fig.2.2 – Overall block diagram of the vacuum pumping system associated to the Alcatel SCM650 apparatus. Adapted from [25].
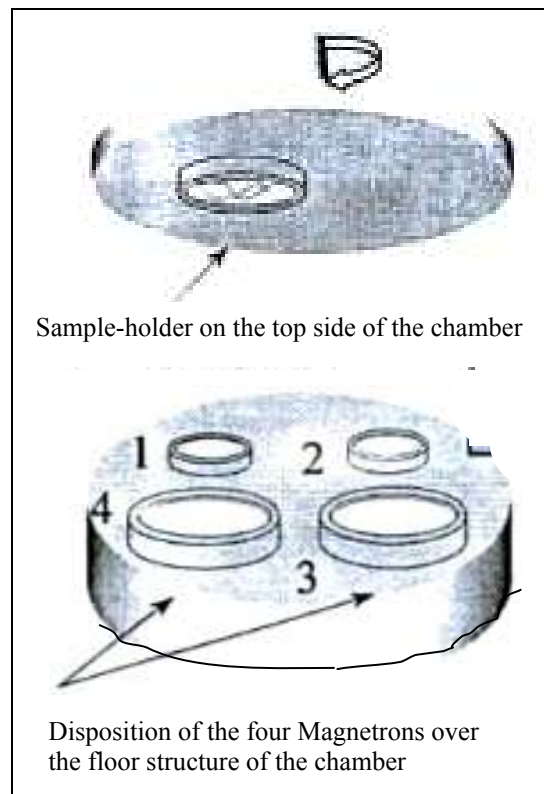
Fig.2.3 – Simplified schematic of the inside view of the vacuum chamber. Adapted from [25].

Two materials were simultaneously used as target to produce the composite materials: alumina (Al_2O_3), for the dielectric matrix, and Germanium (Ge) for the semiconductor NCs doping. An Al_2O_3 plate (purity of 99.99%, 50mm diameter) was initially glued on a brass backing plate using silver vacuum glue. After the drying period, they were properly mounted on the magnetron structure like is possible to observe on Fig.2.4. Here, we can see the cross section view of all the elements associated to the target. The anode plate used had a hole with 40mm in diameter in its centre. So, in practice, the useful area of the Al_2O_3 plate used as target was ~12,57cm^2.
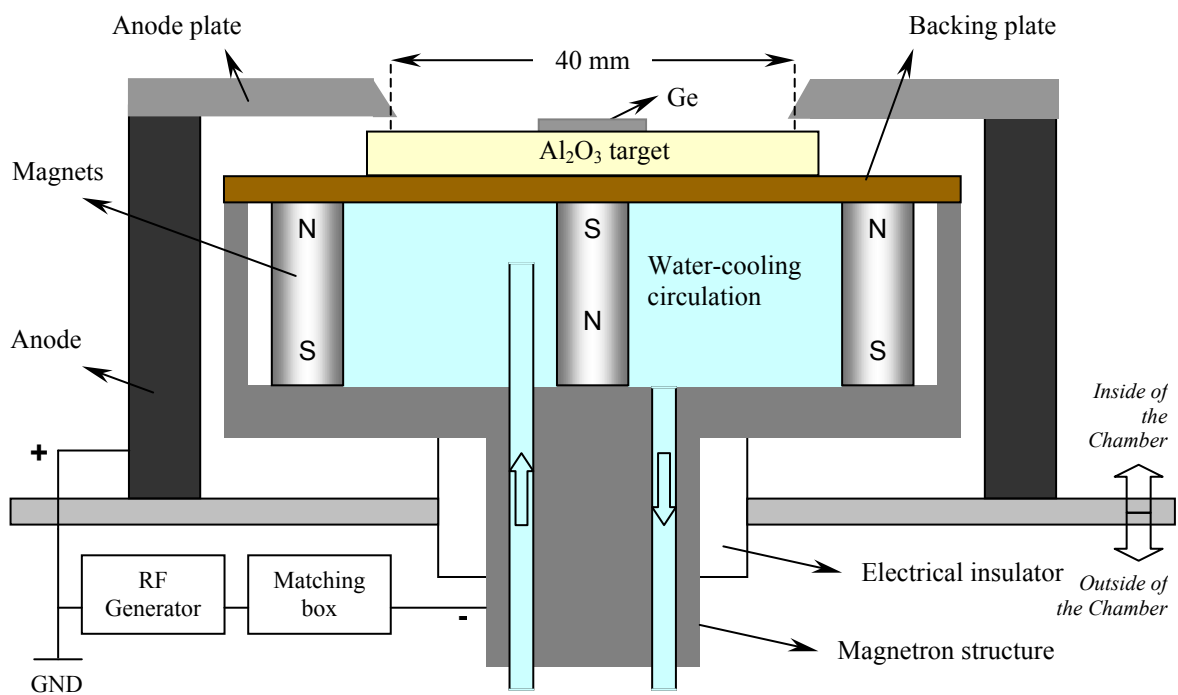
Fig.2.4 – Schematic cross-section view of the magnetron structure showing the Al_2O_3 target and anode plate properly mounted. (Note that relative dimensions are not in scale).

On top of the Al_2O_3 target, 1cm^2 piece(s) of unpolished polycrystalline Ge sheet (purity of 99.999%) were also placed as target(s) to produce the co-sputtered films. The number of the Ge pieces and their position over the Al_2O_3 target was initially changed in order that the concentration of Ge atoms in the films could be varied. This was done by using three different target configurations like shown in Fig.2.5. In configurations 1 and 2, two pieces of Ge covering 15.92% of the target total area were used, while in configuration 3 the percentage of the target total area covered by the Ge piece was 7.96%.

Three different kind of materials were used as substrates: normal glass microscope slides (ISO 8037), fused silica (*FS*), and n-type both sides polished *Si* wafers with (111) and (100) orientations. The electrical resistivity value of the *Si* wafers was in the range of 3-6Ω·cm and 0-100Ω·cm, respectively for (111) and (100) orientations. The glassy substrates were clean with alcohol inside an ultrasound machine for a period of time of 10 minutes and were let to dry on air (just a few seconds) before being mounted on the sample-holder.
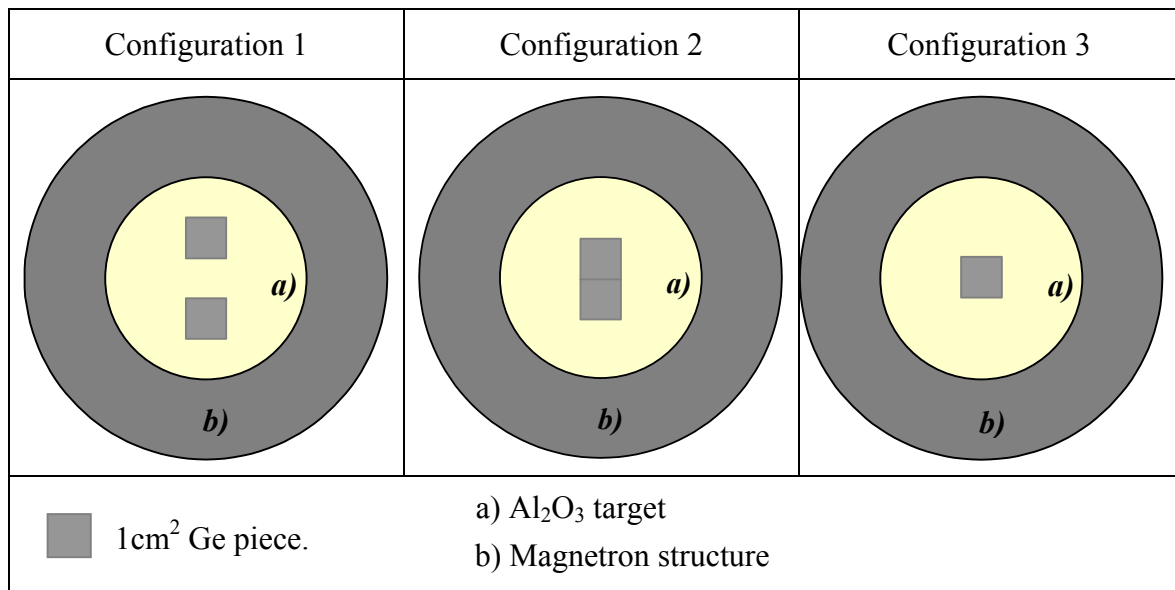
Configuration 1	Configuration 2	Configuration 3
a) *b)*	*a)* *b)*	*a)* *b)*
▨ 1cm^2 Ge piece.	a) Al$_2$O$_3$ target b) Magnetron structure	

Fig.2.5 – Description of the three target configurations in terms of quantity and positioning of the Ge pieces placed on top of the alumina target.

The samples-holder had a square-like shape. However, its useful area to place substrates was a 14.5cm diameter circle. This area was coincident with the size of a copper (*Cu*) heating plate attached to it, on top of which the substrates were placed and fixed. This heating plate is full of grooves on the backside Fig.2.6 (a). It acted as thermal conductor between the samples heating resistance and the samples. A circular stainless steel mask with nine square holes, approximately 2cm^2 each, was used to cover and fix the substrates placed on top of the front side of the *Cu* heating plate. This made it possible to have nine distinct areas of film deposited over the same or different kind of substrates in each deposition (nine different samples per deposition). Since a big number of samples were to be produced, it was necessary to establish how to label the samples. In order to distinguish the position of each one of the samples regarding their positioning over the target, they were marked as shown on Fig.2.6 (b). Meanwhile, each one of the depositions, or series, were labelled with capital letters as film

depositions were being carried on (series A, B, C, …, X, Z, AA, AB, …etc…). Also, it was important to know the kind of substrate used, so the samples were also labelled with FS, for fused silica substrates, and Si when the films were grown on n-type silicon (111) substrates, while for glass substrates nothing else was added on the labelling. So, depending on the deposition series, position over target, and type of substrate, a possible label to find in one sample could be, for instance, A11, B22FS or AC32Si.
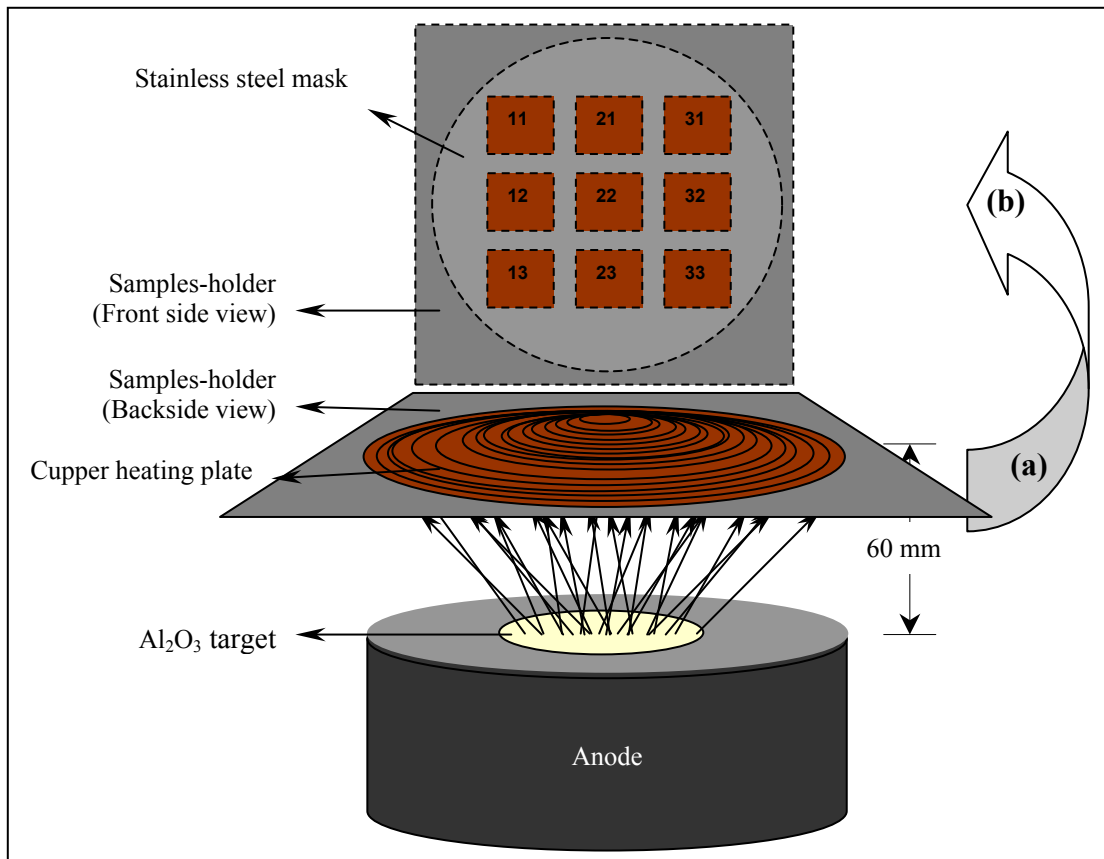
Fig.2.6 – Schematic showing the placement of the samples-holder over the target (a), and the criteria numbering established to label the samples of each series regarding their positioning on the holder (b).

After mounting the samples on the samples-holder, the set was immediately putted inside the pre-vacuum chamber (load-lock). Only after reaching a pressure value of 5.0×10^{-2}mbar in the load-lock the automatic transfer process of the samples-holder into the deposition chamber was allowed. Prior to sputtering, base pressure values of at least 3.0×10^{-5}mbar and 9.0×10^{-6} mbar was reached inside the chamber for the production of the alumina and the Ge doped alumina (Al_2O_3+Ge) films, respectively. *In situ* argon plasma treatment of target and substrates was performed in order to clean the surfaces before starting the growth of the films:

100W *RF* -power and an Argon flux of 100*sccm* were used during approximately 10 minutes for this process. The distance between the target and the samples-holder (or substrates) was maintained in a constant value of 60mm for all the depositions.

The deposition parameters of all the series of films that were produced, both Al_2O_3 films and Ge doped Al_2O_3 films, are presented in Annex II. Note that for the production of the series of films "BE" to "BL", and "Thin_Al_2O_3-1" to "Thin_Al_2O_3-9", a different type of silicon substrates together with a different samples-holder mask were used, which allowed for the production of films deposited over entire 2 inches n-type (100) Si wafers.

As you may find in Annex II, a big number of deposition series of films, both Alumina and Ge doped alumina, were deposited. Of course that most of them could not be fully characterised and studied, or even analysed in time to be part of this work. Nevertheless, I decided to include in Annex II all the series of films that were deposited. Note, however, that only the ones that appear in **bold** text have related results presented on or referred along the results and discussion on chapter 3. Table 2.1 presents the summary of the deposition parameters of all the produced series. Low *RF*–sputtering power values were mostly used because we intended to produce films with low deposition rates, in order to originate films with the lowest internal stress-strain as possible. Some deposition rate values are presented further on, when revealing the film thickness values that were estimated.

Table 2.1 – Amplitude values of the main deposition parameters used in the production of the films.

Parameter	Type of film	
	Al_2O_3 films	**Al_2O_3+Ge films**
Base pressure (mbar)	≤ 3.0 ($\times 10^{-5}$)	≤ 9.0 ($\times 10^{-6}$)
Argon pressure (mbar)	$2 - 8$ ($\times 10^{-3}$)	$2 - 10$ ($\times 10^{-3}$)
RF – power (watt)	$50 - 120$	$40 - 100$
Substrate temperature (ºC)	$100 - 500$	*R.T.* $- 500$
Time (minutes)	$2 - 270$	$5 - 270$

2.1.2 Annealing

The annealing system used to anneal all the samples was the one shown on Fig.2.7. It is mainly composed by a conventional oven from *TermoLab, Fornos Eléctricos LDA* Company, associated to a quartz tube passing through its interior ceramic heated tube, different gas lines

connections, a pumping system composed by a rotary pump plus a diffusion pump able to reach high vacuum pressure values, and pressure gauges. The temperature inside the glass tube was controlled by a *Eurotherm* temperature controller (model 2216L) connected to a *Thermocoax* type K thermocouple able to reach temperatures up to 1250ºC, with an error of 0.75% above 333ºC.

To make an annealing, the samples had to be positioned inside and at the centre of the quartz tube. Before doing this, they were always placed on top of an alumina "boat" (inset of Fig.2.7), with the thermocouple hanging on just above the samples. Usually, two to four samples were annealed at the same time. After this, and providing that the desired pressure and atmosphere inside the quartz tube was already reached, the heating process could be started. An average value of $30ºC.min^{-1}$ was used to increase the temperature. After the annealing time passed the oven was shut down and the samples were maintained inside the quartz tube under the same pressure and atmosphere until they reach room temperature (RT). Only in a few cases the temperature at which the samples were removed from inside the annealing quartz tube was above RT, but always below 100ºC. The representative annealing ramp used in the 800ºC/1hour annealing process is shown in Fig.2.8 as a function of time.

Fig.2.7 – Annealing system used: (a) oven, (b) thermocouple, (c) temperature controller, (d) quartz tube, (e) gas lines, (f) rotary pump, (g) diffusion pump, and (h) pressure gauges.
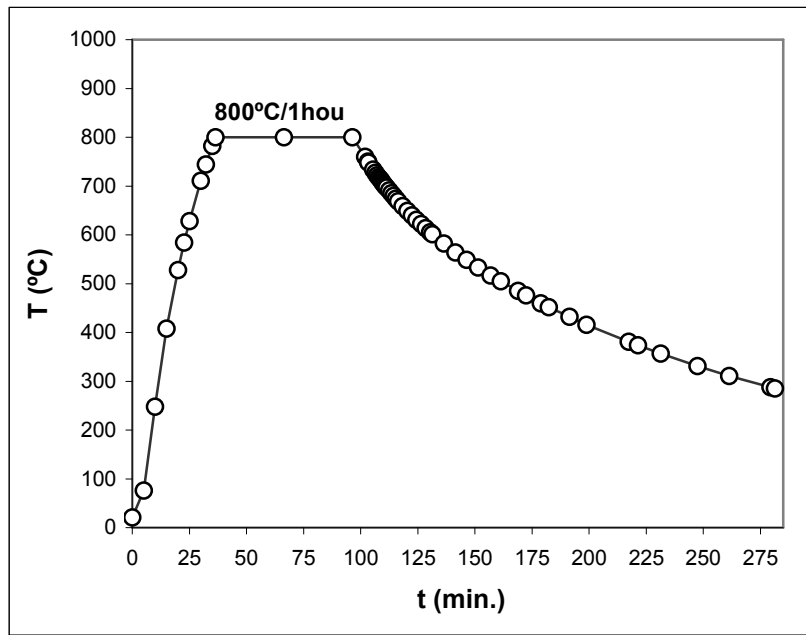
Fig.2.8 – Experimental annealing ramp obtained for the 800ºC/1hour annealing processes.

Different annealing conditions were performed in the as-grown films in order to improve/obtain the crystalline Ge (c-Ge) phase in the Ge doped alumina films and to try to achieve control over the Ge NCs. The deposited films were annealed at temperatures between 550ºC to 900ºC under different pressure atmospheres of air, Nitrogen, and Argon, most of which using one hour for the annealing time. While samples deposited over glass substrates were annealed at temperatures in the range of 550-580ºC, samples deposited on silicon substrates were annealed at temperatures above 800ºC. The annealing parameters of all the annealed samples, both of Al_2O_3 and Ge doped Al_2O_3 films, are presented in Annex III. Table 2.2 presents a summary of those annealing parameters.

Table 2.2 – Summary of the annealing parameters range used in the annealing of the films.

	Type of film	
Parameter	**Al_2O_3 films**	**Al_2O_3+Ge films**
Pressure (mbar)	$1000 - 8 \times 10^{-6}$	$1000 - 8 \times 10^{-6}$
Substrate temperature (ºC)	$800 - 1000$	$550 - 900$
Annealing time (min.)	$60 - 450$	$60 - 240$
Atmospheres	Air, Argon, Nitrogen	Air, Argon, Nitrogen

2.2   Materials characterisation

After the production of the films it was necessary to proceed with their characterisation, both structural and optical. Several characterisation techniques were employed to study the properties of the produced films. A brief introduction to all the techniques that were used to characterise the produced films, including an experimental description of their use, is presented at this sub-chapter.

For the structural/chemical characterisation the main results were obtained by X-ray diffraction (XRD), Raman scattering, Rutherford Backscattering Spectrometry (RBS), Transmission Electron Microscopy (TEM) and High Resolution TEM (HRTEM). A few complementary results using X-ray photoelectron spectroscopy (XPS), Scanning Electron Microscope (SEM), and small angle diffraction (SAD) were also obtained. The optical characterisation was made by means of spectrophotometry (optical absorption spectroscopy) in the near ultraviolet–visible–infrared (NUV–Vis–IR) range and PL (photoluminescence).

2.2.1   X-ray diffraction

X-rays are electromagnetic radiation of wavelength about 1 Å, which is about the same size as an atom. They occur in that portion of the electromagnetic spectrum between gamma rays and the ultraviolet radiation. Their discovery in 1985 by Wilhelm Conrad Röntgen (Noble prize of Physics in 1901) enabled scientists to probe crystalline structure at the atomic level. Nowadays, X-ray diffraction (XRD) is one of the most important characterisation tools used in solid-state chemistry and materials science and has been in use in two main areas: for the fingerprint characterisation of crystalline materials and the determination of their structure. Each crystalline solid has its unique characteristic X-ray powder pattern, which may be used as a "fingerprint" for its identification. Once the material has been identified, X-ray crystallography may be used to determine its structure, i.e. how the atoms pack together in the crystalline state and what the inter-atomic distance and angle are, etc. [26]. In other words, the size and shape of the unit cell for any compound can, in principle, be easily determined using the diffraction of X-rays.

An X-ray diffractometer is essentially composed of a power supply, an X-ray tube, a samples-holder, and a detector, all controlled by computer software. Two different analysis

methods (geometries) can be distinguished and are frequently used in XRD measurements: the symmetrical and the asymmetrical modes.

In the symmetrical method, also known as coupled θ-2θ or Bragg-Brentano geometry, both sample-holder and detector rotates. During the measurement process the incidence θ_i angle formed between the incident X-rays direction and the sample surface plane increases step by step due to the sample-holder rotation. As the sample-holder rotates, the detector also rotates in a coupled way, always maintaining $\theta_i = \theta_r$ (known as Bragg angle). The reflection angle, θ_r, is the angle defined by the sample surface plane and the detector normal direction (see Fig.2.9).
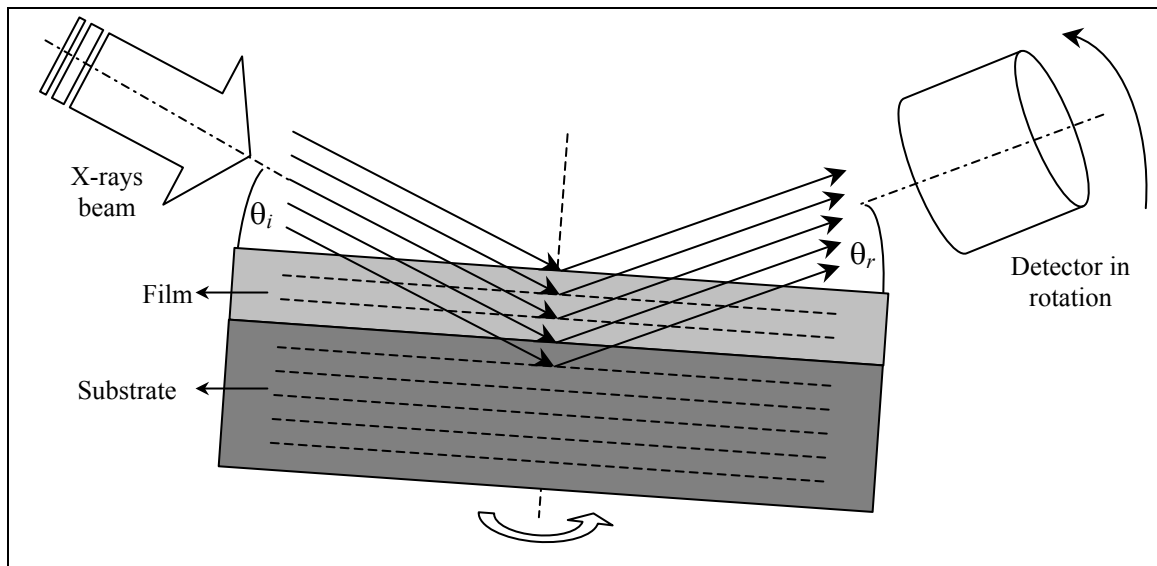
Fig.2.9 – Schematic representation of an X-ray diffraction measurement made with *Bragg-Brentano* geometry.

In the asymmetrical mode, or uncoupled θ-2θ method, the samples are placed on a sample-holder that is fixed in a certain position without rotation. While measuring, the incident angle θ_i is kept constant and only the detector moves, performing the scanning along different θ_r angle values. Among asymmetrical methods, glancing-angle incidence X-ray diffraction (GIXRD) technique is the most used one. GIXRD technique, sometimes also called grazing incidence XRD, is based in the fact that the incidence angle, θ_i, is a very small fixed angle (typically $0.5° < \theta_i \leq 3°$). This fact gives GIXRD the advantage of reducing dramatically the amount of X-ray radiation that penetrates the sample in depth. X-rays will, however, travel a bigger distance inside the film and, eventually, will not reach the substrate

of the sample. Because of this, GIXRD spectra are usually more "clean" spectra, containing a lot more information about the film(s) material(s) and less information coming from the substrate. GIXRD technique is, in fact, more appropriate to the study of thin films samples then the conventional Bragg-Brentano geometry [27].

X-ray diffraction technique allowed investigating the crystallographic structure and determining the average NCs size in the films. The determination/confirmation of the crystallographic structure based on XRD is made by comparing the known lattice spacing values, *d*, defined on the JCPDS tables with the experimental ones, using the well known Bragg's Law ($n\lambda = 2dsen\theta$).

The shape of the diffraction peaks depends on the size and defects of the present crystallites, and the relation between peaks intensities gives information about the sample's texture [27]. The full width at half maximum (FWHM) of the diffraction peaks, β_{FWHM}, allows the estimation of the apparent average size of the particles by using the Debye-Scherrer formula [28]:

$$D = \frac{0.9\lambda}{\beta_{FWHM}\cos\theta},$$
(2.1)

where *D*, the mean diameter of the NC, comes as a function of λ, the wavelength of the X-ray source, θ, half of the angle between incident and diffracted beam (Bragg angle), and β_{FWHM}. The value of 0.9 is the typical value of the dimensionless shape factor, which can varies with the actual shape of the crystallite. In order to be able to estimate the mean diameter values *D* of the Ge NCs on each sample, Lorentzian distribution functions fitting each peak of the XRD spectra had to be done to obtain β_{FWHM}.

XRD studies involved measurements performed at three different sites. Most of them were done at University of Minho (UM) using the Bragg-Brentano geometry. GIXRD technique was used in measurements performed both at the Physics Department of University of Lisbon (UL), using the collaboration of Prof. Olinda Conde, and at the European Synchrotron Research Facility (ESRF) in Grenoble, France, these last made by Prof. Maria Gomes in the

scope of SEMINANO[3] project. The measurements done both at UM and UL were carried out using Cu k$_\alpha$ radiation ($\lambda_{\alpha 1} \approx 1.54056$ Å and $\lambda_{\alpha 1} \approx 1.54439$ Å), 40 kV generator tension, 30 mA generators current, and a wavelength intensity ratio (alpha$_1$/alpha$_2$) of 0.500. At UM, measurements were performed in a Philips PW1710 diffractometer in a continuous scan type with monochromator, and a counting time of 1.25 to 2.5 seconds per 0.02° steps. GIXRD spectra obtained at UL were recorded in a Siemens D5000 diffractometer, without monochromator, a counting time of 16 to 20 seconds per 0.04° step, and an incidence angle of 1°. Concerning the GIXRD spectra obtained at the ESRF, measurements were obtained with an 0.25° incident angle, counting time of 3 to 4 seconds, and scan steps corresponding to approximately 0.145 to 0.18°.

2.2.2 Raman scattering

Raman spectroscopy technique is used in condensed matter physics and chemistry to study vibrating, rotational, and other low-frequency modes in a system. C. V. Raman discovered the inelastic scattering phenomenon, which bears his name in 1928. For it, he was awarded the Nobel Prize for Physics in 1930. Physicists welcomed Raman's finding as proof of quantum theory. Chemists found it an invaluable tool for analyzing the composition of liquids, gases, and solids. The introduction of lasers in the 1960s made it even more useful. Today, and being a non-destructive characterisation technique, Raman spectroscopy is used to monitor everything from manufacturing processes to the onset of life-threatening illnesses [29].

When light is scattered from an atom or molecule, most of the photons are elastically scattered (Rayleigh scattering), maintaining the same energy (frequency) as the incident photons. However, a small fraction of the scattered light (approximately 1/1000 photons) is scattered from excitations with optical frequencies different from, and usually lower than, the frequency of the incident photons [30]. This small fraction of light is due to Raman scattering, which produces scattered photons that differ in frequency from the radiation source that originated it (also known as the Raman Effect). In other words, we may say that Raman scattering relies on the inelastic scattering of monochromatic light, usually from a laser in the visible, near infrared, or near ultraviolet range, that interacts with phonons or other excitations

---

[3] SEMINANO – Full title of the research project is "Physics and Technology of Elemental, Alloy and Compound Semiconductor Nanocrystals: Materials and Devices".

in the system, resulting in the energy of the laser photons being shifted up or down. The shift in energy gives information about the phonon modes in the system. Phonons are elementary excitations present in the ordered solid materials due to the atomic vibrations. The scattered light carries out information not only about the vibrations themselves but also on the structural and electronic properties of the materials through the electron-phonon coupling [31].

Since the intensity of the Raman scattered light is much lower than the intensity of the incident light, Raman scattering technique demands for intense radiation sources and high sensibility detector devices. The technique has become more prominent in the years since powerful monochromatic laser sources could provide the necessary scattering power, and detection systems like photomultipliers (PM) or charge coupled devices (CCD) could improve the detection resolution [27].

Raman measurements were performed at the Physics Department of the University of Minho (DFUM), with the help of Prof. Anabela Rolo. However, due to temporary unavailability of the Raman equipment at the UM, some measurements had also to be done at the Physics Department of University of Aveiro (UA), with the help and collaboration of Prof. Rosário Correia. The systems and equipments that exist both at UM and UA are exactly the same. They are based on a Jobin-Yvon T64000 system with an Olympus BH2-UMA microanalysis system and a CCD detector. The systems are computer controlled and possess a triple monochromator. With the help of a microscope objective lens (Olympus BH2-UMA), the laser beams is focused in a spot area of approximately $1\mu m^2$ of the sample's surface, and in a backscattering geometry (see Fig.2.10). This means that incident and scattered beams make an angle of 180º between them. A small screen (AH-SPS) allows the visualisation of the micro-spot beam at the sample's surface [27].
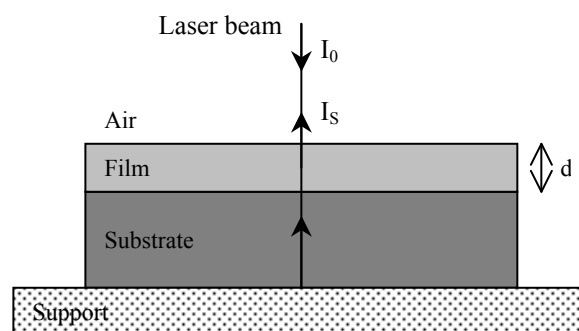
Fig.2.10 – Schematic representation of the system used in the Raman scattering measurements (microanalysis set up in backscattering geometry).

Raman spectra were obtained using the more intense lines of the Argon laser (Coherent Innova 92 Ar$^+$), λ= 514.5nm (3.0W) and λ= 496.5nm (1.5W). Values in parenthesis are the maximum possible power of the laser for the correspondent wavelength. However, the system allows controlling the power in a *quasi*-continuous way, ranging from few miliwatt to the maximum power value. In order to avoid the possibility of local crystallisation of the Ge in the samples, the laser power values on the samples were always optimized in order to avoid thermal effects and local crystallisation on the sample (typical laser power on the sample about one miliwatt). All measurements were performed at room temperature (21ºC), with an approximate resolution of 2cm^{-1} and a 578 pixels CCD detector.

2.2.3 RBS

Rutherford Backscattering Spectrometry (RBS) is a standard technique in the analysis of materials. It is used to determine the elements present in a given sample, their stoichiometry, and their depth distribution. Besides being a non-destructive technique, its main advantages are that it is fully quantitative, i.e., the use of external standards is not necessary, and that a precision better than 1% can be achieved with careful analysis [32]. The technique involves measurement of the number and energy distribution of energetic ions (usually MeV light ions such He$^+$) backscattered from atoms within the near-surface region of solid targets. The targets (samples) are irradiated with light ions (usually 2-3MeV α-particles or protons) and the elastically backscattered projectiles at large angles are detected (Fig. 2.11 (a)), usually by semiconductor detectors Si (Au). The mass of the target atoms could be identified from the energy of the backscattered projectile (Fig.2.11 (b)) [33].

Rutherford Backscattering Spectrometry measurements were performed at the *Instituto Tecnológico e Nuclear* (ITN) in Sacavém, Portugal, using the collaboration with Dr. Eduardo Alves and Dr.ª Ana Ramos. Citing the samples report received from these collaborators, RBS spectra were obtained with 2 Schottky barrier detectors placed in IBM geometry at 140º and 180º scattering angles, with resolutions of 15 and 25keV respectively, using a 2.0MeV He$^+$ beam. Analyses were performed with samples tilted at 0º and 30º (angle between beam direction and sample normal). All spectra obtained for the same sample were simultaneously analysed with WINDF [32] and a unique solution was found. Extra information/descriptions that I believe are interesting to cite were also contained within the collaborators report, quoting: "RBS simulation results are presented as layer distributions. Thickness units are

nanometers (nm). However, the natural units in RBS used by the simulation programs are atoms per square centimetre (at/cm^2). In order to obtain thicknesses in nm, a density value has to be given. As the film density is usually unknown, an average density value is assumed (according to Bragg's rule). This average density value depends both on the concentration of each individual element and on the elemental densities, and it is therefore different for each layer. Note that the thickness of the substrate layer (the last of the layers in the layer structure given) cannot be assessed, as it is above the range of analysing beam. A nominal value of 100000×10^{15} at/cm^2 is therefore given. The concentration values in the graphs are presented in atomic % and are subject to a relative error of 5%."
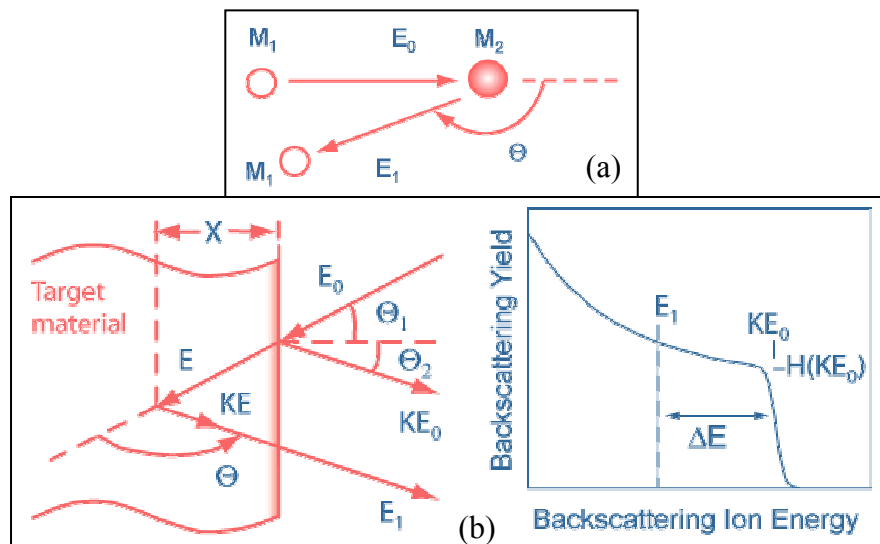
Fig.2.11 – (a) Schematic of a classic collision and backscattering of a lighter projectile of mass M_1 with a heavier target particle of mass M_2 initially at rest inside a target material (the recoil of the target particle is not plotted); (b) Schematic of backscattering event from a thick elemental sample and a typical resulting spectrum. Adapted from [33].

2.2.4 XPS

X-Ray Photoelectron Spectroscopy (XPS) was developed by K. Siegbahn and his research group in the mid 1960s. Siegbahn was awarded the Nobel Prize for Physics in 1981 for his work in XPS. The phenomenon is based on the photoelectric effect outlined by Einstein in 1905 where the concept of the photon was used to describe the ejection of electrons from a surface when photons impinge upon it [34].

Also known as Electron Spectroscopy for Chemical Analysis (ESCA), XPS is a surface analysis technique used for obtaining chemical information about the surfaces of solid

materials. Both insulators and conductors can easily be analysed from areas a few microns and larger. The method uses an X-ray beam to excite a solid sample resulting in the emission of photoelectrons. An energy analysis of these photoelectrons provides both elemental and chemical bonding information about the material comprising the sample surface. With exception for hydrogen and helium all elements can be detected. XPS is a surface sensitive technique because only those photoelectrons generated near the surface can escape and become available for detection. Due to collisions within the sample's atomic structure, those photoelectrons originating much more than about 20 to 100Å below the surface are unable to escape from the surface with sufficient energy to be detected [35].

Samples analysis by XPS requires an ultrahigh vacuum environment and a low-energy monochromatic X-ray source. X-ray excitation causes the emission of photoelectrons from the atomic shells of the elements present on the sample's surface. Energy analysis of the emitted photoelectrons is the primary data used for XPS. These energy values are characteristic of the element from which they are emitted. By counting the number of electrons as a function of energy, a spectrum representative of the surface composition is obtained. The area under peaks in the spectrum is a measure of the relative amount of each element present, and the shape and position of the peaks reflect the chemical state for each element [35].

If compared to RBS, it can be said that XPS technique allows obtaining accurate values about the surface elemental composition of materials (only a thickness of a few nanometres is affected during measurement). XPS analysis in depth is possible, but those levels must be reached first, for instance using ion sputtering. On the other hand, RBS technique is more appropriate for measurements that may need to be performed in samples having high thickness, up to approximately 1μm or more. While in RBS all the atomic structure levels contribute to the final result, XPS measurements are only valid for a certain depth level.

During XPS measurements, analytical information was obtained by *Survey Scan* and *Depth Profile* measurements. Energy peaks in the survey scan identify the elemental composition of the uppermost 20 to 50Å of the analyzed surface. All elements, except hydrogen and helium, are detected. Detection limits are approximately 0.1 atom percent for most elements. Concerning depth profile, the elemental composition is measured as a function of depth into the sample by alternating AES (Auger Electron Spectroscopy) analysis with ion sputtering to remove material from the sample surface. Depth resolution of <100Å is possible [35].

X-ray photoelectron spectroscopy (XPS) was performed at the *Servicio de Nanotecnología y Análisis de Superficies* (C.A.C.T.I.) inside the facilities of University of Vigo, Spain. Based on the description given in the results samples report that was received, the analysis of the samples was performed using an VG Escalab 250 iXL ESCA instrument (VG Scientific), using monochromatic Al-k$\alpha_{1,2}$ radiation (hν=1486.92 eV) X-ray source. Due the non-conductor nature of samples it was necessary to use an electron flood gun to minimize surface charging. Neutralization of the surface charge was dome by using both a low energy flood gun (electrons in the range 0 to 14eV), and an electrically grounded stainless steel screen placed directly on the sample surface. Photoelectrons were collected from a take-off angle of 90º relative to the sample surface. The measurement was done in a Constant Analyser Energy mode (CAE) with a 100eV pass energy for survey spectra and 20eV pass energy for high resolution spectra. Setting the lower binding energy C1s photopeak at 285.0eV C1s hydrocarbon peak did charge referencing[4]. The spectra fitting are based on "Chi-squared" algorithm used to determine how good the peak fit is. Chi-squared < 2 implies a good fit. The components of the peaks can be free or coupled of ways reflecting the chemistry of the sample. In most of the cases the FWHM (full width at half maximum) value was fixed to defined values. Surface elemental composition was determined using the standard Scofield photoemission cross section. The chemical functional groups identification was obtained from the high-resolution peak analysis of carbon-1s (C1s) and oxygen-1s (O1s) envelopes.

2.2.5 SEM

Scanning Electron Microscopy (SEM) is an imaging technique mostly used in studying surface morphology. However, the number of practical applications in which SEM images are used is enormous and is usually related with materials evaluations, failure analysis, and/or quality control screening. Information like grain size, particle size distributions, surface roughness, porosity, material homogeneity, inter-metallic distribution and diffusion, contaminants location, electrical conductivity, electrostatic discharge effects, film and coating thickness, etc… can be obtained by SEM analysis. Fig.2.12 shows the example of a SEM image used for film thickness determination.

---

[4] Practical Surface Analysis. Vol. 1, Edited by D. Briggs and M.P. Seah.

The principle of operation of this technique is based on a highly focused high-energy electrons beam being projected into the sample surface in a raster scan pattern. Those electrons interact with the atoms that constitute sample's structure, generating secondary electrons, back-scattered electrons, and characteristic X-rays. All these "signals" can be collected by detectors to form images of the sample displayed in real time on a screen.

Secondary electrons imaging, the most common or standard detection mode, can produce very high-resolution images of a sample surface, revealing surface topography details about 1 to 5nm in size. Back-scattered electrons (BSE) are beam electrons that are reflected from the sample by elastic scattering. BSE are often used in analytical SEM along with the spectra made from the characteristic X-rays. Since the intensity of the BSE signal is strongly related to the atomic number (Z) of the specimen, BSE images can provide information about the distribution of different elements in the sample. In fact, the possibility of having analysed the X-ray fluorescence generated from the atoms in the path of the high-energy electrons beam is a great feature of SEM, enabling for a fast elemental composition analysis using EDS (Energy Dispersive X-Ray Spectroscopy). All elements with an atomic number greater than Boron and with concentrations on the order or grater than 0.1% can be detected using EDS.

All the SEM images of this work were obtained at Science School of University of Minho using a LEICA Cambridge S360 microscope, which possessed a secondary and scattered electrons detector. Measurements were carried out in vacuum at approximately 10^{-6}mbar. Due to the insulator nature of samples, films had to be coated with a high conductivity material before measuring, preventing from charge accumulation on the samples surfaces. A thin film of gold was deposited over the analysed samples using a sputter coater SC502 from Fisons Instruments.

2.2.6 TEM, HRTEM, and SAD

Transmission Electron Microscopy (TEM) is an imaging technique that allows determining the internal structure of materials. The first practical transmission electron microscope was built by Albert Prebus and James Hillier at the University of Toronto in 1938 using concepts developed earlier by Max Knoll and Ernst Ruska.

In the same way that light is transmitted through materials in conventional optical microscopy, materials for TEM analysis have to be prepared in such a way that electrons must be able to pass through the sample. Since they interact strongly with matter, electrons are

attenuated as they pass through a solid requiring the samples to be prepared in very thin sections. This implies that, most of the times, samples preparation for TEM measurements are very time-consuming and delicate. An example of a sample prepared for TEM can be observed in Fig.2.12, presented next page. A beam of electrons is transmitted through the specimen, then an image is formed, magnified, and directed to appear either on a fluorescent screen or layer of photographic film, or to be detected by a sensor such as a CCD camera. As the wavelength of electrons is much shorter than that of light, the resolution attainable in a TEM is many orders of magnitude greater than that from a light microscope. As a consequence, TEM images can reveal finest details of internal structure. However, if we need to obtain images of the crystallographic structure of a sample down to the atomic scale we must use high resolution TEM (HRTEM), which is an imaging mode of the TEM. Because of its high resolution, it is an invaluable tool to study nanoscale properties of crystalline materials such as semiconductors and metals.
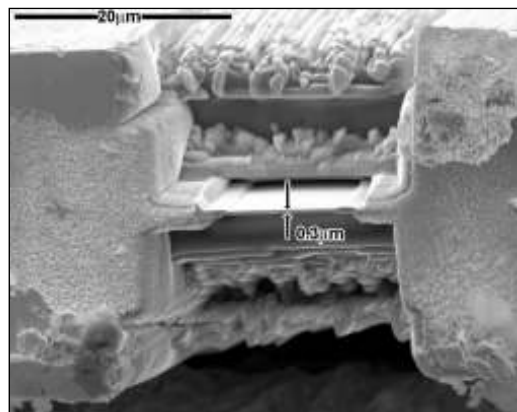
Fig.2.12 – SEM image of a thin TEM sample milled by focused ion beam. The thin membrane is suitable for TEM examination; however, at approximatelly 300nm thick, it would not be suitable for High-Resolution TEM without further milling. Adapted from non-specified source.

Prof. Terje Finstad and Dr. Steiner Foss performed TEM and HRTEM measurements at University of Oslo, Norway, in the scope of SEMINANO project. The cross section TEM-samples were prepared by gluing two substrates together with film side facing each other. This sandwich was then cut, and mechanically polished down to 50μm. Finally the sample was ion milled to electron transparency. A JEOL 2000FX was used for the TEM analysis.

Besides the acquisition of the TEM images, the colleagues at Norway also made a quick analysis of the films by EDS (Energy Despersive X-ray Spectrometry), to find Ge:Al composition ratios, and SAD (Selected Area Diffraction). Selected area (electron) diffraction,

abbreviated as SAD (SAED), is a crystallographic experimental technique that can be performed inside a transmission electron microscope. As a diffraction technique, SAD can be used to identify crystal structures and examine crystal defects. It is similar to X-ray diffraction, but unique in the way that as small as several hundred nanometres in size can be examined, whereas X-ray diffraction typically samples areas several centimetres in size.

2.2.7 Optical absorption

Most materials absorb some light. The amount of absorption is, for most of the substances, a function of the wavelength of the incident light. Absorption spectroscopy refers to a range of techniques employing the interaction of electromagnetic radiation with matter. Absorption is the process by which the energy of a photon is taken up by another entity, for example, by an atom whose valence electrons make transition between two electronic energy levels. The photon is destroyed in the process, and the absorbed energy may be re-emitted as radiant energy or transformed into heat energy. In other words, a material's absorption spectrum shows the fraction of incident electromagnetic radiation absorbed by the material over a range of frequencies. The absorption spectrum is, in a sense, the opposite of an emission spectrum. It may be reasonable to say, then, that by looking at a certain sample absorption spectrum it may be possible to find "promising" samples regarding the possibility of having light emission phenomenon that might be associated to the presence of NPs as part of the composition of that sample structure.

A spectrophotometer, as it is called, is an instrument that measures the amount of optical absorption in a certain material as a function of wavelength (exciting energy). There are four main components that can be distinguished in a spectrophotometer: the light source (1), the monochromator (2), the sample chamber (3), and the detector (4). Fig.2.13 schematically represents the basic setup of measuring the absorption (or transmission) of light through a sample.
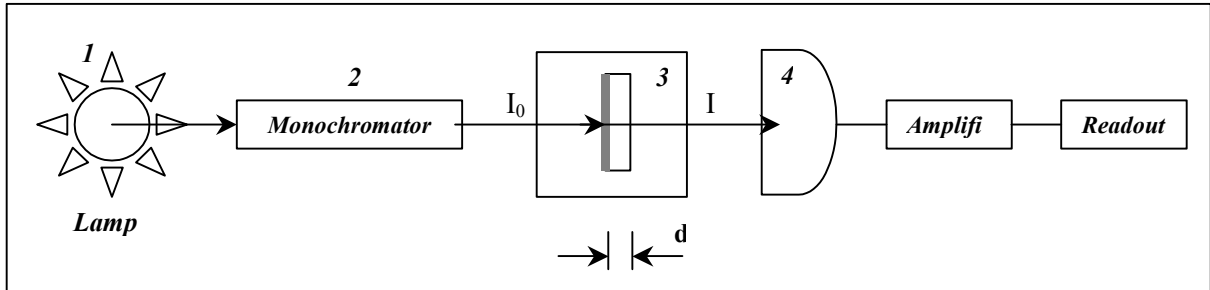
Fig.2.13 – Representative schematic of the absorption measurements. Light of intensity I_0 incident upon a sample of thickness **d** undergoes a loss in intensity upon passing through the sample. The final intensity measured is ***I***.

Light of some wavelength λ having reference intensity I_0 is incident normally on some sample of interest. Upon passing through the sample the intensity of the light is reduced to a value *I*, perhaps due to absorption within the sample and reflection at the surfaces of the sample. A measurement of I_0 and *I* can then be used to determine the transmission of the sample at wavelength λ. For example, if a detector voltage is measured as 1.50mV at 532nm for the reference, and 1.35mV at 532nm for the sample, the transmission (*T*) of the sample is 0.90 (=1.35/1.50). Thus, 90% of the incident light is transmitted through the sample.

There are two basic types of spectrophotometers, single-beam and dual-beam. In a single-beam spectrophotometer both the reference intensity (I_0) and the intensity of the light after passing through the sample (*I*) are obtained sequentially. In a dual-beam instrument, the two spectra are obtained simultaneously. The advantage of the dual beam instrument is that any time-dependent variations in the intensity of the light emitted by the source can be compensated, thus improving sensitivity and reducing uncertainty.

The absorbance, *A*, also called *optical absorbance* or *optical density*, is a dimensionless quantity defined as the negative of the base -10 logarithm of the transmission, *T*, ($A=-log_{10}T$), which is another useful way to report the optical absorption.

The absorption measurements were performed in a Shimadzu UV-3101PC dual-beam spectrophotometer, with the possibility of measuring in the wavelength range of 200–3200nm. One of the beams passes through the sample (film deposited over the substrate) and the other one through a reference material (in our case air). The samples were placed in such a way that the incident beam is perpendicular to the sample's plane. All the measurements were performed at room temperature and atmospheric pressure, and recorded in a computer with the help of specific acquisition software.

2.2.8 Photoluminescence

Photoluminescence (abbreviated as PL) spectroscopy is a contactless non-destructive method of probing the electronic structure of materials. Light is directed onto a sample, where it is absorbed and imparts excess energy into the material in a process called photo-excitation. One way this excess energy can be dissipated by the sample is through the emission of light, or luminescence. In the case of photo-excitation, this luminescence is called photoluminescence. The intensity and spectral content of this photoluminescence is a direct measure of various important material properties. In short, one can say that PL is a process in which a substance absorbs photons (electromagnetic radiation) and then re-radiates photons. In terms of Quantum Mechanics, this can be described as an excitation to a higher energy state and then a return to a lower energy state accompanied by the emission of a photon. The period of time between absorption and emission is typically extremely short, in the order of 10 nanoseconds. That is the case of *resonant radiations*, the simples PL process, in which a photon of a particular wavelength is absorbed and an equivalent photon is immediately emitted. Under special circumstances, however, the period of time between absorption and emission can be extended into minutes or hours. (Just to mention, other forms of photoluminescence are *fluorescence* and *phosphorescence*). So, photo-excitation causes electrons within the material to move into permissible excited states. When these electrons return to their equilibrium states, the excess energy is released and may include the emission of light (a radiative process) or may not (a non-radiative process). The energy of the emitted light (photoluminescence) relates to the difference in energy levels between the two electron states involved in the transition between the excited state and the equilibrium state. The quantity of the emitted light is related to the relative contribution of the radiative process. The most common radiative transition in semiconductors is between states in the conduction and valence bands, with the energy difference being known as the band gap, but may also involve localized defect levels. Non-radiative processes are, in general, associated with localized defect levels, whose presence is detrimental to material quality and subsequent device performance. Thus, material quality can be measured by quantifying the amount of radiative recombination [36]. In fact, recombination mechanisms as well as impurity levels and defect detection are important issues to consider when studying photoluminescence processes, and they should not be forgotten. However, they are not mentioned and/or presented in more detail along the thesis.

For the luminescence measurements, all samples were placed in a closed cycle cryostat. Photoluminescence spectroscopy was performed using a 514.5nm Argon laser source, with a laser power of approximately 200mW. The sample's PL signal intensity was obtained as a function of temperature, which was varied from *RT* down to 10K. The spectra were recorded with a SPEX grating monochromator, using standard lock-in techniques. An *InGaAs* detector was used to record the sample PL intensity signal in the range of 800-1700nm [10]. The schematic presented on Fig.2.14 represents the PL experimental setup.
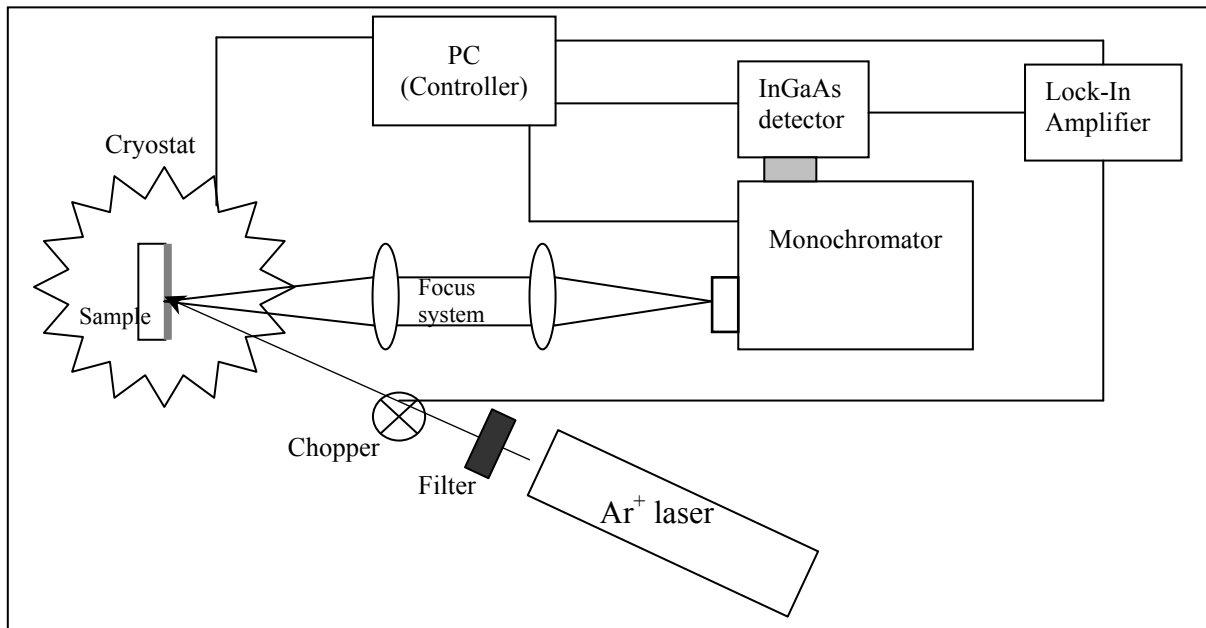
Fig.2.14 – Schematic of the PL experimental setup.

Chapter 3
Results and discussion

3. Results and discussion

Results and discussion are presented in a way that, I hope, is the most perceptible one. With this intention, and insofar as possible, they are generally divided according to the chronologic sequence of the films production, i.e., first the Al_2O_3 films, then the Ge doped Al_2O_3 films deposited over glassy substrates, and finally the Ge doped Al_2O_3 films deposited over silicon substrates. All the argumentation and discussions are made along the presentation of the results. Remember that: "the main objective in this work is to develop fundamental and technological knowledge on the production and characterisation of layer structures based on semiconductor nanocrystals…" and that "It includes mainly:

- The growth of composite films containing Germanium nanoparticles formed in Aluminium Oxide matrix using the magnetron sputtering technique;

- The structural and optical characterisation of above composite material." [5]

In general terms, the structural characterisation was started by using XRD and Raman for qualitative analysis regarding to, first, the structural nature of the Alumina films standing alone and, second, the presence or not of c-Ge nanoparticles embedded on the Alumina matrix. Spectra from XRD and Raman techniques were also used to estimate the average NCs size. SEM analysis was not easy to make because of the very low contrast of the dielectric matrix, but still it was possible to estimate the thickness of some of the films. RBS measurements gave us the information about the elements present in our films, their atomic percentage, and a first estimation about the average density and thickness of the films. XPS allowed us to find chemical bondings, ratios and stoichiometry, as well as for comparisons with RBS results about the elements present on samples and their concentrations. TEM and HRTEM images made it possible to clearly see the morphology of the films as well as to obtain some statistics concerning the NCs size distribution.

Concerning the optical characterisation, optical absorption and photoluminescence measurements could be performed. Mainly, the optical absorption (and transmission) measurements were useful for an initial indication about the potential emission properties of the films. The refractive index and extinction coefficient were obtained from the ellipsometry spectra. Finally, PL spectroscopy was performed to evaluate the possibility of having some kind of light emission that could, eventually, be attributed to the presence of Ge NCs on the produced composite materials.

---

[5] - Translated from the Master Degree's Work Plan.

3.1 X-ray diffraction elements identification

The identification of all the chemical elements expected to appear at the X-ray diffractions spectra of the produced films was made using the JCPDS - *Joint Committee on Powder Diffraction Standards* data base cards. Each one of these cards contain all the information about the X-ray diffraction planes of the material in question, namely its lattice spacing values (d), the relative diffraction intensity values (I/I_0), the values of twice the corresponding diffraction angles (2θ), as well as the Miller indexes (*hkl*). As mentioned in sub-chapter 2.2.1, using Bragg's Law it becomes possible to plot the graphs of the relative intensities (I/I_0) as a function of the diffraction angle (θ) for each material, and compare them with the experimental XRD results. The materials that were considered for this kind of comparison were Germanium (Ge), all Aluminium Oxide (Al_2O_3) polymorphs, and, for the films deposited over Silicon (Si) substrates, also Si was considered. The numbers of the JCPDS cards used to identify/confirm the presence of these materials in the films, as well as the minimum relative intensity values of the diffraction planes of the JCPDS cards that were considered for comparison, are presented in Table 3.1.

Table 3.1 – JCPDS card numbers and the minimum relative intensity values corresponding to the diffraction planes, which were used and considered during XRD identification of the elements.

Chemical element and polymorph	JCPDS card number	Minimum relative intensity values (%) considered
c–Germanium	4-0545	All considered
α–Al_2O_3	46-1212	14
δ–Al_2O_3	46-1215	10
γ–Al_2O_3	50-741	All considered
κ–Al_2O_3	52-803	8
σ–Al_2O_3	47-1292	7
θ–Al_2O_3	23-1009	8
c–Silicon	27-1402	All considered

3.2   Al$_2$O$_3$ films

Before producing the Ge doped Al$_2$O$_3$ films it was important to have an idea of what kind of alumina films we could expect to have as a matrix. So, in order to get a better understanding of the Ge doped Al$_2$O$_3$ films, some alumina films with different deposition and annealing parameters were firstly produced. An effort was made to use the same deposition parameters as we intended to use in the subsequent production of the Ge doped alumina films. However, due to equipment useful time, only a few Al$_2$O$_3$ films were produced for this purpose and very few of them were deposited on Silicon substrates. Nevertheless, some good alumina samples were studied, with a particular emphasis being given to the study of the annealing temperature of those films.

It was reported that in layers deposited at substrate temperatures of 500-1000ºC one obtains metastable γ, δ, and θ phase, as well as k phase [37]. Within the same reference paper it was also stated that it seems to exists a general agreement that amorphous alumina layers are deposited when substrate temperature is less than 500ºC, and that those amorphous metastable PVD-Al$_2$O$_3$ films are used as dielectric layers, barrier layers, and optical layers [37]. Our Al$_2$O$_3$ films were produced maintaining the substrate temperature at 500ºC. This was the maximum substrate temperature that was considered to be "safe" to use by the deposition system. Since we previously new that higher temperatures would be needed to form Ge NCs, our study about the alumina films was focused not on the substrate temperature during growth but on the post annealing temperatures of the films. Nevertheless, all growing parameters, including substrate temperature during growth, must be, of course, taken into account when analysing the final results.

Figures 3.1 a) and b) presented below show the X-ray spectra of two different alumina samples grown on Si(111) substrate, samples AC22Si and AE22Si from series AC and AE respectively, obtained with Brag-Brentano geometry. Besides the XRD results from the as-grown samples, also the XRD spectra obtained after each one of the three different thermal treatments that were performed on this samples are shown on the graphs (see all annealing parameters on Annex 3). It must be notice that these two samples were always annealed simultaneously, and that the same two initial peaces of samples were consecutively used to perform the three thermal treatments mentioned above, using different annealing temperatures of 800 (R), 900 (R2), and 1000ºC (R3). Due to the very low number of alumina samples that were grown on Si(111) substrates, no "fresh" independent as-grown samples could be used for this study.
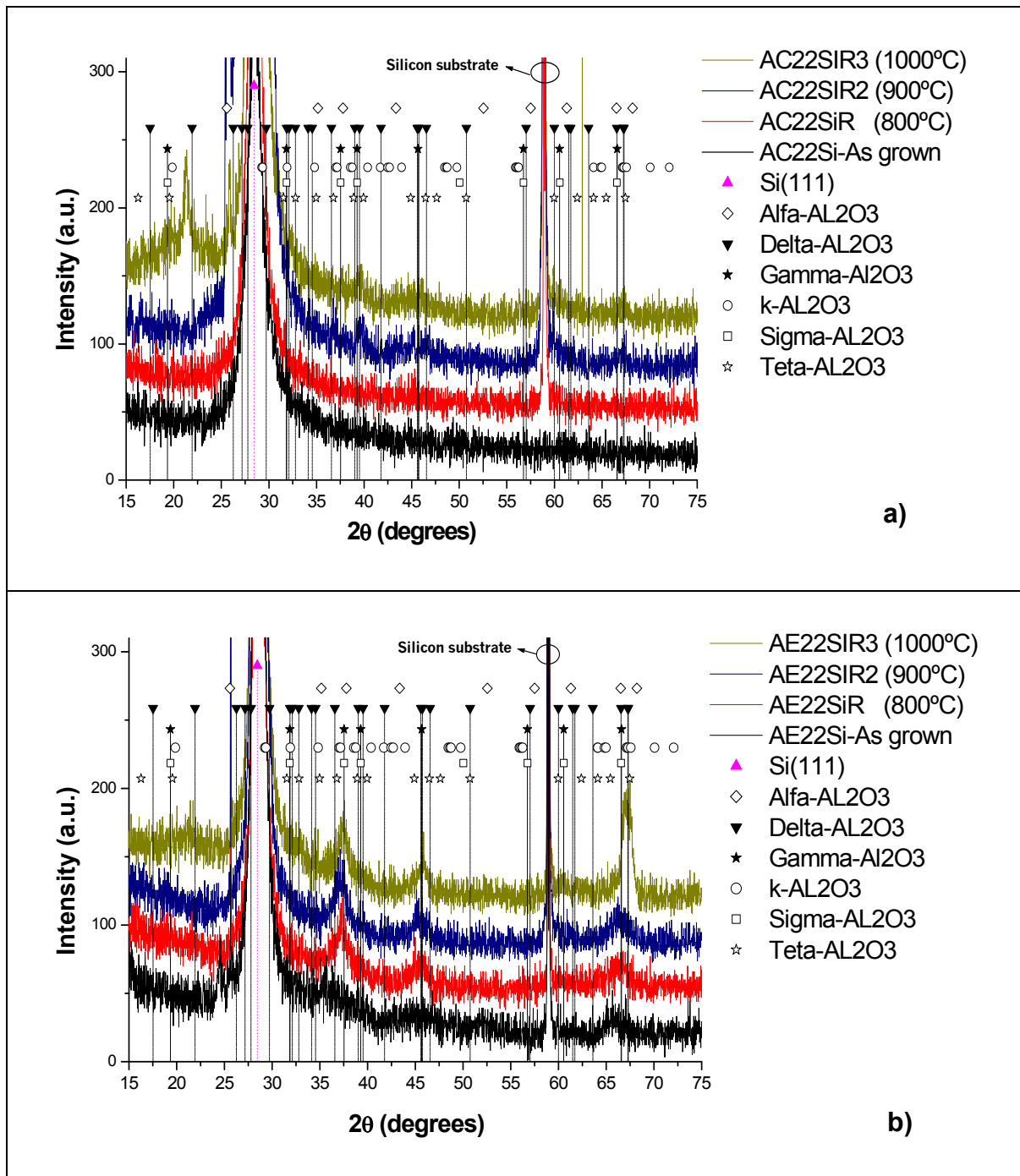
Fig.3.1 – X-ray diffraction spectra of two different samples of Al_2O_3 films obtained with Brag-Brentano geometry: **a)** sample AC22Si, deposited at 500ºC using 50W *RF*-power for 5,5 hours under an Argon pressure of 4.0×10^{-3} mbar; **b)** sample AE22Si, deposited at 500ºC using 80W *RF*-power for 3 hours under an Argon pressure value of 2.0×10^{-3} mbar.

Looking at the graphs of Fig.3.1 above and considering the fact that those two films were produced using different deposition parameters, it can be said that, in general, alumina films produced with $P_{RF} = 50W$ and $p_{AR} = 4.0 \times 10^{-3}$ mbar (Fig.3.1 a)) tend two be mostly amorphous, even if annealed up to 1000ºC, while alumina films deposited with $P_{RF} = 80W$ and $p_{AR} = 2.0 \times 10^{-3}$ mbar (Fig.3.1 b)) seems to have a tendency to form some crystalline γ–Al_2O_3 and δ-Al_2O_3 grains. γ–Al_2O_3 seems to be predominant until 900ºC annealing temperature, while for

1000ºC an increase of the δ–Al$_2$O$_3$ phase is clearly observed. If we take a more detailed look at both graphs of Fig.3.1, one can also observe that a very small amount of non-amorphous δ–Al$_2$O$_3$ phase is also present when annealing temperature is equal or higher than 900ºC in graph a), and that in graph b) even the as-grown sample already indicate the presence of a non completely amorphous alumina. So, it seems that the nucleation of the first Al$_2$O$_3$ grains from the AC series sample (Fig.3.1 a)) must have been formed originally during the annealing treatment performed at 900ºC, while for the sample of series AE (Fig.3.1 b)) alumina grains probably started to form already during growth at 500ºC. This proves that, as it was expected, the use of different deposition parameters can give rise to alumina films with different crystalline structures. Even so, and admitting that the ideal situation, for this preliminary study about the matrix alumina material, would be to have "fresh" as-grown samples before each one of the different thermal treatments, I believe the results are interesting, reliable and could be considered as a good starting point reference.

Later on, during experiments time it was possible to perform some XRD measurements at the ESRF using GIXRD technique. Samples AC22SiR3 and AE22SiR3 (annealing at 1000ºC) were analysed. The obtained spectra presented on Fig.3.2 indeed confirm the first results obtained using the Brag-Brentano geometry. On the contrary of spectra shown on Fig.3.1, graphs on Fig.3.2 are clear from any contribution resulting from high X-rays penetration and diffraction at the Si(111) substrate, which was only possible to "eliminate" with GIXRD geometry. The diffraction peaks are now sharper and it becomes much easier to characterise now the samples. Sample AC22SiR3 clearly processes some δ-Al$_2$O$_3$ grains as well as γ-Al$_2$O$_3$ ones, with a considerable amount of amorphous alumina still being present. In the case of sample AE22SiR3, the degree of crystallization is without any doubt higher, but the type of structure is quite similar: both γ and δ phases coexist.

Besides samples AC22SiR3 and AE22SiR3, also an as-grown alumina sample (AC2.1Si) was measured at ESRF (inset of Fig.3.2), confirming the amorphous nature of alumina films produced using deposition parameters similar to those of series AC. Unfortunately, a similar as-grown sample from series AE could not be measured, preventing us from having a more "clear picture" of the kind of alumina phase(s) that are formed in as-grown films produced with deposition parameters similar to those of series AE.
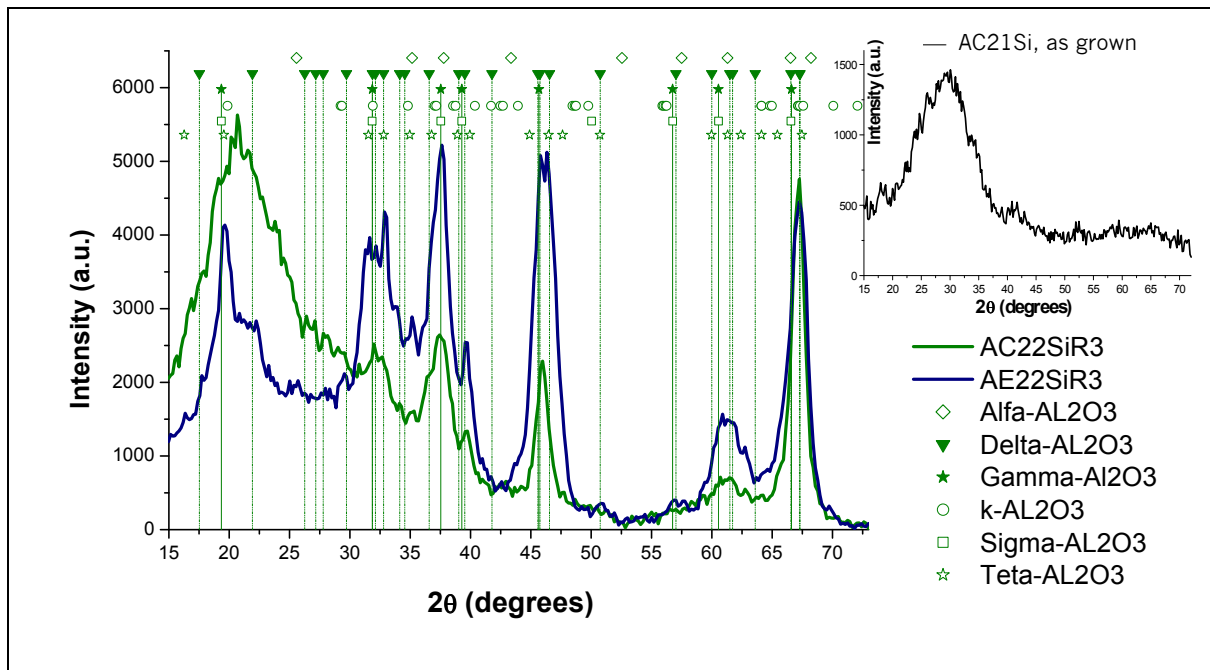
Fig.3.2 – Comparison of the GIXRD spectra of the annealed samples AC22SiR3 and AE22SiR3. Spectrum obtained from sample AC21Si is shown at the inset. All three spectra obtained at the ESRF.

One of the objectives in producing the Ge nanoparticles embedded dielectric layer films was, by the end, to be able to form the Ge NCs but without crystallizing the Al_2O_3 matrix. The results of the annealing study of samples AC22Si and AE22Si NCs suggests that 1000ºC annealing temperatures should be avoided, otherwise there will be risk of having a considerable degree of matrix crystallisation. Because of this result 1000ºC were not used for annealing the Ge doped alumina films, and even the temperature of 900ºC was avoided.

A similar experimental study to that one presented just above could not be done for alumina films deposited over the glass substrates (microscopic slides). Due to the low temperature tolerance of the normal microscopic slides, the temperature of annealing had to be limited to 580ºC, otherwise they would start to bend when placed on top of the alumina "boat" (see inset of Fig.2.7), creating extra stress on the films structure. Nevertheless, it was possible to observe good optical and structural properties on as-grown Al_2O_3 films deposited at 500ºC over glassy substrates, i.e. high transparency visual appearance and amorphous films. Data presented respectively on Fig.3.3 a) and b) indeed confirms this. Please, see also on Fig3.4 the representative pictures of Al_2O_3 films deposited over Silicon (inset) and glassy substrates.
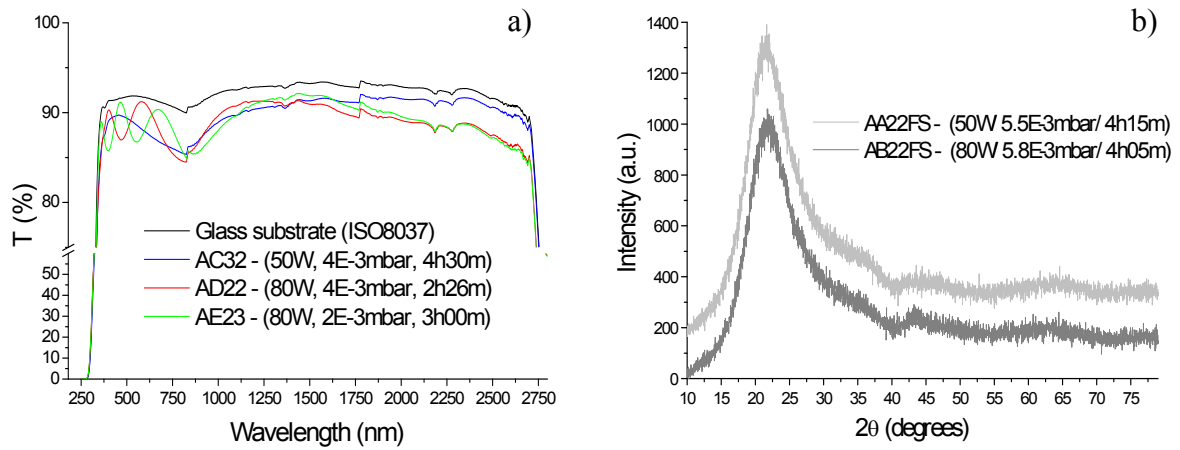
Fig.3.3 – a) transmission spectra of three different Al$_2$O$_3$ films deposited at 500ºC over glass substrates, presenting very high transparency across all wavelength UV-visible-NIR; b) XRD spectrum from two as-grown Al$_2$O$_3$ films deposited at 500ºC over Fused Silica substrates, revealing their amorphous nature. (Deposition parameters P_{RF}, p_{Ar} and t shown between parentheses).
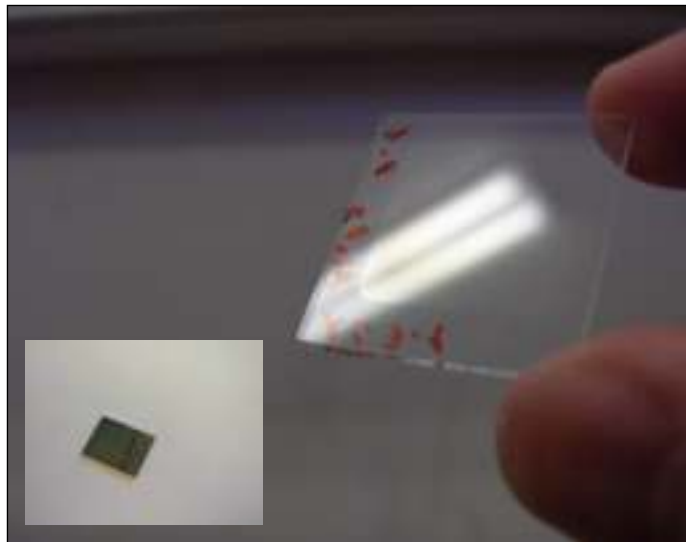
Fig.3.4 – Picture of a typical Alumina film (sample AC3.1) deposited on glass. Although it is a quite transparent sample, the contour of the film is still visible. For comparison, the inset picture shows the look of a piece of a sample from the same series deposited on Silicon substrate (sample AC21Si).

3.3   Ge doped Al$_2$O$_3$ films

In order to tune some initial features like the amount and ideal position of the polycrystalline Ge sheets to be placed over the Al$_2$O$_3$ target, the production of the first Ge doped Al$_2$O$_3$ films was started using glass slides as the substrate. After this initial phase, a few films were grown over FS substrates and Si substrates were also used. The majority of the series were produced using both normal glass and Si substrates placed at different locations of the samples-holder.

Three very important aspects of this work were investigated, mainly by X-ray diffraction and Raman spectroscopy. Firstly, the effect of the deposition Argon pressure (p_{Ar}) on samples deposited over FS substrates was tested. Secondly, using the p$_{Ar}$ that were concluded to be the best, new films deposited over Si(111) substrates were produced in order to study the *RF*-sputtering power (P$_{RF}$) parameter variation. Last but not least, the annealing effects on the crystalline nature of the films were also evaluated. The final intention was to assure the ability to (re)produce films having suitable Ge NCs which could be fully characterised, both structural and optically.

3.3.1 SEM analysis

The SEM measurements were done to estimate the thickness of some of the produced films and compare those values to the ones that we previously knew from the RBS measurements (presented below, point 3.3.2). Due to the insulating nature of the alumina and to the insufficient time to have a better sample preparation, it was not easy to obtain good pictures that could allow for a optimal visual estimation of the thickness. Still, some pictures like the one presented at Fig.3.5 allowed to estimate some thickness values, but only on a few samples. In the particular case of sample Z22Si, an approximate thickness of 611nm was estimated. Table 3.2 presents all the thickness values that were possible to obtain from the remaining samples analysed by SEM (pictures not shown). Values are in accordance with what was expected based on the deposition parameters and disposition of the samples over the target. Some other to view SEM pictures also revealed a very smooth films surface, like the one presented on Fig.3.6, which represents the SEM surface morphology of all the films that were analysed.

Table 3.2 - Average thickness values, stipulated by the SEM pictures, and deposition rate values, determined by the thickness value divided by the corresponding series deposition time.

Sample name	d (nm)	Dep. Rate (nm/min.)
U21	897	3.32
U22	972	3.60
U33	800	2.96
X22	1045	3.87
Z22	611	2.4
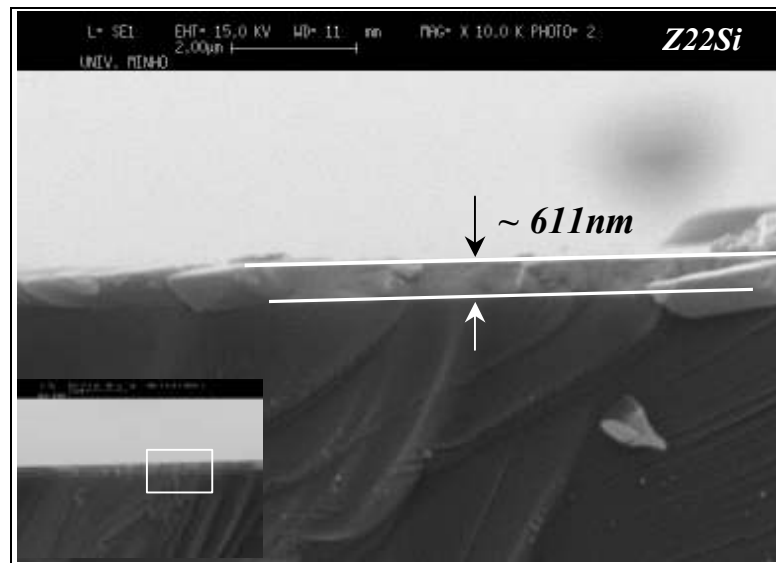
Fig.3.5 – Cross-section SEM picture obtained for sample Z22Si: estimated thickness of 611nm.

Fig.3.6 – Top view surface picture of sample Z21Si, obtained by SEM. Darkest dots on the picture were not possible to identify. Some of them may possibly be small areas with higher Ge concentration.

3.3.2 RBS and XPS chemical analysis

As described previously at sub-chapter 2.1.1 and shown previously on Fig.2.5, three different target configurations were tested in order to check the concentration of Ge at the co-sputtered films. By visual observation of the produced films, we quickly realise that configuration 1 originate films having very high concentration of Ge NPs, which was not a desirable thing. This was confirmed by some preliminary optical absorption measurements (not shown herein), with results giving very low optical transmission percentage values, indicating that a lot of Ge (maybe more than 50 atomic percent) was in fact inside the film. So, we tested configuration 2. The results were not as bad as those in configuration 1 but still a lot of Ge was present in the films. Unfortunately, neither the films produced with configurations 1 or 2 could be submitted to chemical analysis, so no proof confirming this can be presented. After excluding configurations 1 and 2, it was then proposed to reduce the amount of Ge on the target to half (only one peace) and positioning it at the centre of the target. This was called configuration 3 and it proved to be more suitable in obtaining Ge doped Al$_2$O$_3$ films with more reasonable Ge atomic concentration values. After this initial comparison process, all the films were deposited using target configuration 3.

The identification of the chemical elements and atomic concentrations of some selected as-grown samples, deposited using target configuration 3, could be determined and estimated using both RBS and XPS chemical analysis techniques. Data concerning the atomic percentage of the elements in depth, ratios, and stoichiometry of the films could also be stipulated.

The results of the RBS analysis are summarised on next page at Table 3.3. The AlO(Ge) film compositions, thicknesses, and the Bragg densities are listed. The Ge atomic percentage (at.%) inside those films was found to be in between 14 to 20%. Note that, except for the samples H22 and P22 (deposited on glass substrates), all other samples were deposited on Si(111) substrates. It was not a surprise to find that it was for the samples positioned at the centre of the samples-holder ("central samples"[6], with position reference 22) that the lowest Ge concentration was found (14 at.%), while those positioned at the corners of the samples-holder have the highest amount of Ge, up to 20 at.%. In fact, most of the samples analysed with RBS were central samples from different series, except for samples U21Si and U33Si.

---

[6] "Central sample" stands for a film that was positioned on the centre of the samples holder during deposition process (labelled with 22 at the samples name). For this reason, central samples are the most homogeneous ones of each series.

Table 3.3 – Simulation results obtained for samples analysed by RBS technique.

Sample name	O (at.%)	Al (at.%)	**Ge** (at.%)	Thickness (x10^{15} at/cm^2)	Average Density (x10^{22} at/cm^3)	Thickness (nm)
H22*	53	33	14	4450	4.89	909
P22	49	35	16	3950	4.93	801
T22Si*	53	29	18	3530	4.82	732
U21Si	49	33	18	6150	4.89	1257
U22Si	50	34	16	8200	4.90	1672
U33Si	48	32	20	5850	4.88	1198
V22Si	52	31	17	4150	4.86	853
X22Si	50	34	16	8500	4.91	1733
Z22Si	50	33	17	4750	4.90	969

*Average value.

Concerning Ge at.% values on table 3.3, the maximum difference among all central samples (corresponding to different deposition parameters) is about 4%. The exact same difference (4%) is encountered when comparing the Ge at.% among the three samples of the U series (corresponding to different positions at the samples-holder over the target). This means that the position of the samples over the target may induce similar differences on the Ge atomic percentage as the ones resulting from changing deposition parameters. It was important, although, to confirm that, as suspected, elemental atomic percentage differences among samples from the same series do exist and must be considered. However, it is also important to mention that, for similar samples produced using the same deposition parameters and having the same position over the target, like it is the case of samples U22Si and X22Si, equal results were found. This proves that both the results and deposition methods are consistent and reliable. Nevertheless, we must not forget that RBS technique is used to determine the elements present in a given sample, their stoichiometry and their depth distribution, and that the concentration values presented in atomic percentage are subject to a relative error of 5%. The thickness values in Table 3.3 are only shown as a plus, and must not be considered as absolute since that is not the purpose of the RBS technique (more details and comments about those thickness values are mentioned on the last text paragraph of page 64).

Once again, the reasons for having different Ge concentration values in samples from the same series are due to geometrical aspects, mainly related to the magnetron, target and samples-holder configurations issues. Even if further technical explanations about this are not very important for the purpose of the present research work, I would like to say that I am convinced that some optimization processes related to those parts of the deposition chamber should be implemented in a future work, in order to be possible for the user to diminish or enlarge the differences of the at.% of the semiconductor embedded in the films matrix the way he pleased.

On Fig.3.7 the result of the RBS measurement made on sample U22Si is shown. It represents the typical RBS spectra and simulation (inset) of an as-grown sample deposited over Silicon. Results demonstrate that the sample shows a homogeneous composition profile, with approximately 16% of Ge atoms. The other two elements present, Aluminium (Al) and Oxygen (O), are also distributed rather uniformly across the majority of the films. In the particular case of sample U22Si there are about 34% of Al atoms, and 50% of O atoms in that film. All RBS spectra and simulation results are presented in Annex IV.
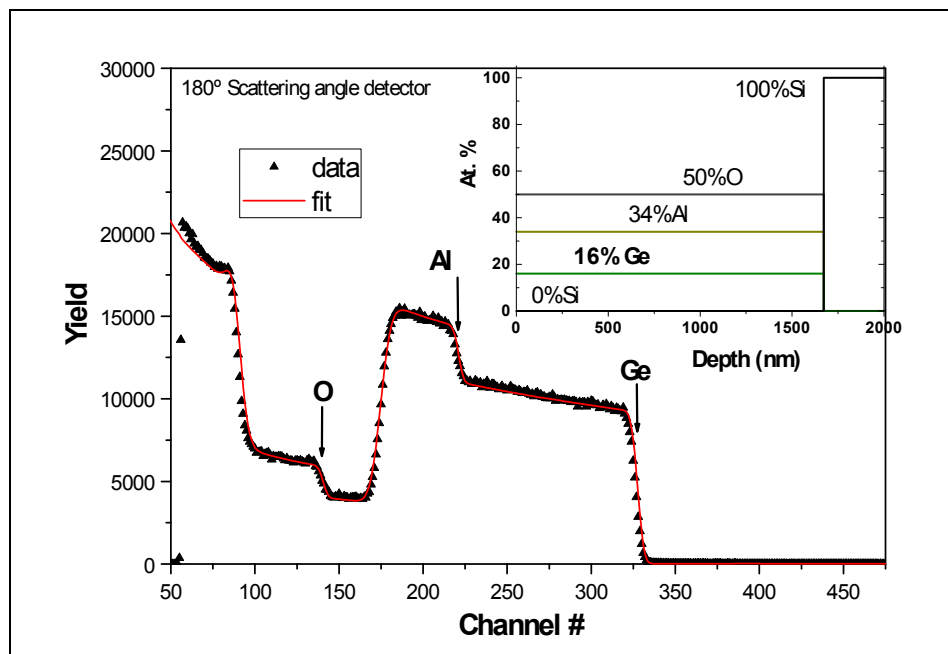
Fig.3.7 – Typical fitting and simulation (inset) spectra obtained after RBS measuring of a Ge doped Al₂O₃ film (in the case, sample U22Si). Adapted from [38].

The other samples deposited on silicon also have homogeneous composition depth distribution. The only exception is sample T22Si, with a decreasing Al/O ratio in depth (the Ge/O ratio remains more or less constant). About samples deposited on glass, sample P22 has a homogeneous composition depth distribution. In the case of sample H22, an increase in the Ge/O ratio with increasing depth is observed (Al/O ratio remains constant). The spectra of sample H22 also indicate some possible glass/film mixture, which may be the result of interface roughness. However, the effect is small and therefore was not included in the simulation done by our collaborators at the ITN. Finally, sample F22 [7], the most difficult one. About this particular sample our collaborators from ITN made the following comments: "… several contaminations are observed: C (signal @ channel # 95 – annular detector) and two other heavy contaminants corresponding to signals @ channels # 356 and # 378 – annular detector. The two heavy contaminants cannot be unambiguously identified. If they correspond to a surface impurity, the masses should be around 200-210 (signal @ channel # 378) and 115-125 (signal @ channel # 356). The spectra of sample F22 also indicate some glass/film mixture, which may be the result of interface roughness or film porosity. The effect has been included in the simulation." The two heavy elements were identified by XPS as being Copper (Cu) and Lead (Pb); see XPS results below.

Concerning RBS measurements, a final attention must be given to the thickness values presented above on Table 3.3. In fact, since we had previously estimated the thickness of some of those samples by SEM (Table 3.2), we knew that those values are not correct. This is due to the fact that the densities of the films are unknown, so an average density value is assumed (according to Bragg's rule), as previously mentioned in chapter 2.2.3. The thickness values directly obtained in the RBS measurement are in at/cm^2. In order that those values can be presented in nanometres they must be divided by an assumed average density having units of at/cm^3. Table 3.4 presents the calculated average density values based on the thicknesses estimated by the SEM measurements. Samples are ordered by decreasing thickness. The associated errors were calculated using the normal propagation errors formula and considering that a maximum error of 50nm was committed in SEM estimations.

---

[7] Results for this sample are merely indicative.

Table 3.4 – Calculated average densities of the films using the thickness values that were determined by SEM.

Sample name	O (at.%)	Al (at.%)	Ge (at.%)	Thickness (x10^{15}at/cm^2)	Thickness by SEM (nm)	Average Density (x10^{22} at/cm^3)	Average Density (g/cm^3)
X22Si	50	34	16	8500	1045	8.13±0.39	2.75±0.13
U22Si	50	34	16	8200	972	8.44±0.43	2.86±0.15
U21Si	49	33	18	6150	897	6.86±0.38	2.32±0.13
U33Si	48	32	20	5850	800	7.31±0.46	2.48±0.16
Z22Si	50	33	17	4750	611	7.77±0.64	2.63±0.22

Note: for comparison, the density of ceramic Al$_2$O$_3$ is 3.97g/cc (or 11.72x10^{22} at/cc), and the density of a sapphire monocrystal is about 5.3g/cc.

The calculated average densities of samples U22Si and X22Si (simulated with the same at.% composition) are the two closest ones, with a difference of about only 3.8%. They present also the two highest density calculated values (2.75 and 2.86g/cc, respectively). The remaining three samples (U21Si, U33Si, and Z22Si) have lower densities. However, since all these three samples possess a higher Ge atomic content than samples U22Si and X22Si, and considering the fact that the density of Ge is as high as twice the density of Aluminium, it could be expectable that the density values of samples U22Si and X22Si were the lowest ones instead of being the highest. So, a question must be made: what is the explanation for this? For the case of samples U21Si and U33Si the reason must lie on the geometrical disposition of samples, namely the fact that they are not central samples. This implies that the Ge atoms coming to their substrates are arriving from the target in a non-perpendicular direction, which is less energetic since atoms have to travel bigger distances before reaching the substrate. For the case of sample Z22Si the explanation for this must be related to the deposition parameters. Although if Z22Si is a central sample, the use of a lower *RF*-sputtering power of 50Watt combined with a higher Argon pressure of 5x10^{-3}mbar must be the reason for having a lower average density than samples U22Si and X22Si.

XPS results

Meanwhile, it was also possible to perform chemical analyses on three samples using XPS technique: samples F22, U22Si, and X22Si, these last two already measured by RBS. The XPS depth profile experiments analysis, included measurements at five different points for each one of them up to approximately 60nm in depth.

In terms of elements identification and uniformity XPS and RBS results are in general agreement:

− XPS elements identification survey spectra confirmed the presence of Ge, Al, and O in samples U22Si and X22Si, and the presence of contaminants in sample F22, in accordance with RBS measurements. A big quantity of Cu and small amounts of Pb and also Na were detected on sample F22. Survey spectra of sample Z22Si is presented at Annex V. [8]

− In terms of uniformity and Ge concentration (values presented in Table 3.5), XPS results indicate that samples U22Si and X22Si are uniform and maintain the concentration in depth. They also have similar Ge*3d* atomic percentage. On the contrary, sample F22 does not possess a uniform concentration in depth and its Ge*3d* at.% is a factor of about 4 times higher than in samples deposited over Si substrate.

However, regarding the Ge content, comparing the c of Ge at.% values of samples U22Si and X22Si, obtained by RBS, to the same values obtained by XPS there is quite a big difference: ~16% Ge at. by RBS and ~6% Ge at. determined by XPS. The use of non-accurate correction factors on the XPS measurements must be the reason for this discrepancy. RBS Ge at.% values are the ones that must prevail, since they are, definitely, much more reliable. Nevertheless, one must not forget that XPS measurements are highly localized measures (in just a few cubic nanometres of material), while RBS data is "coming" from across the entire sample's thickness. Another aspect that must be mentioned regarding XPS measurements is related to the samples preparation for the in depth measurements; it is possible that while performing the etching to reach the desired depth, Ge atoms are being removed with a higher rate from the sample's surface, which could be the reason for the low Ge at.% values that were found.

---

[8] Results with the survey spectra of samples F22 and U22Si cannot be shown due to unsolved graphical compatibility problems.

Table 3.5 – XPS data of Ge*3d* and Ge*3d* Oxide atomic percentage values as a function of depth levels for samples F22, U22, and X22.

	F22		U22Si		X22Si	
	Ge*3d*	Ge*3d* Oxide	Ge*3d*	Ge*3d* Oxide	Ge*3d*	Ge*3d* Oxide
Levels	At. %		At. %		At. %	
0	8.21351	14.436	9.01889	6.88697	8.46006	5.32205
1	12.9891	10.5697	7.45836	0.881912	7.82654	0.782943
2	18.7618	5.80696	6.37653	0.406324	6.12043	0.361372
3	25.0553	6.46298	6.34081	0.412965	6.00976	0.406133
4	13.5649	2.80586	6.39545	0.38225	6.14563	0.448843
5	4.45337	0.458487	6.32596	0.410254	6.02933	0.373211

The main goal of using XPS analysis was to be able to determine the order of magnitude of the Ge Oxide that could be present in the films. It was found that Ge Oxide is present in all three samples. In samples U22Si and X22Si after one sputter cycle the oxide disappeared, indicating that Ge Oxide is a surface phenomenon. However, in sample F22 the oxide is present in a higher proportion than in the other two samples: after one sputter cycle the oxide is still present and remains along the entire depth, indicating that Ge oxide is not a surface phenomenon in sample F22. Please see Fig.3.8, which is representative of all data contained at Table 3.5.
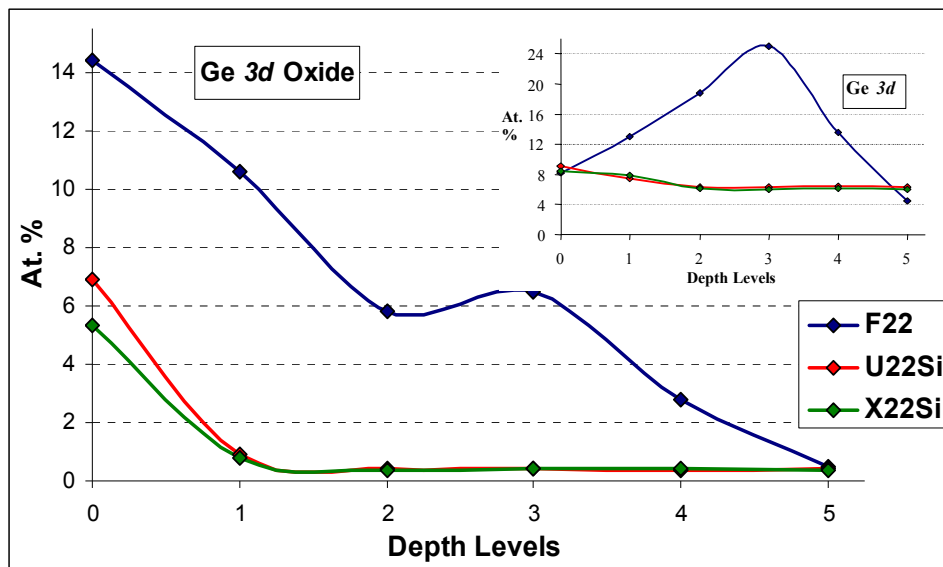
Fig.3.8 – In depth comparison of the Ge*3d* Oxide and Ge*3d* (inset) atomic percentages that were obtained for all three samples analysed by XPS.

Table 3.6 – XPS results of *Al2p*, *Ge3d* and *Ge3d Oxide* atomic percentage and ratios calculated at depth level 3.

	F22	**X22Si**	**U22Si**
At.%			
Al*2p*	46.5001	35.3067	35.4813
Ge*3d*	25.0553	6.00976	6.34081
Ge*3d* Oxide	6.46298	0.40613	0.41297
Ratios			
Al*2p* / Ge*3d*	1.86	5.88	5.60
Al*2p*/(Ge*3d*+Ge*3d* Oxide)	1.48	5.50	5.25

The XPS results made it possible to determine the stoichiometry of the Al_xO_y matrix. Based on the data presented at Table 3.6 above, calculated at level 3 (around 30nm in depth), the results for x and y are as follows:

- sample U22Si, $x = 2$ and $y = 2.8$ ($Al_2O_{2.8}$);
- sample X22Si, $x = 2$ and $y = 3.25$ ($Al_2O_{3.25}$).

After the chemical analysis, it was clear, both by RBS and XPS results, that sample F22 was contaminated. For this reason, all samples from this series were excluded from further analysis or studies. The same happened to all the other series in which a suspicion of possible contaminations also existed.

3.3.3 XRD and Raman

Both techniques were basically used to investigate, in a non-destructive way, the presence of Ge NCs embedded on the films alumina matrix. They were initially used to conduct a study concerning the effect of the deposition parameters on the crystalline structure and quality of the films. With the final intention of assuring the presence of Ge NCs in the films, to different studies were conducted: the first one to evaluate different deposition parameters, and the second regarding the optimization of annealing parameters. The following pages describe and present the results that were obtained from both studies.

Study of the deposition parameters

The XRD and Raman results of three central samples deposited over FS substrates, J22FS, O22FS, and P22FS, are presented below on Fig.3.9. Their deposition temperature (T_{dep}) and the *RF*-sputtering power parameters were the same, kept constant at 500ºC and 50Watt, but different Argon pressures were used: 5.8×10^{-3}, 4.0×10^{-3}, and 2.0×10^{-3}mbar, for the series J, O and P, respectively. Based on the diffractograms that are presented in there, there is no doubt that $p_{Ar} = 4.0\times10^{-3}$mbar (sample O22FS) is the most suitable in obtaining the Ge NCs embedded in the alumina matrix films. On Fig.3.9 a), the (111) and (220) XRD reflection intensities of sample O22FS are slightly higher when compared to the ones of sample P22FS ($p_{Ar} = 2\times10^{-3}$mbar). In the case of sample J22FS ($p_{Ar} = 5.8\times10^{-3}$mbar), no refraction peaks are visible from the XRD pattern. At the inset of Fig.3.9 a), the GIXRD spectrum of sample O22FS clearly revealed the (111) and (220) reflections as well the (311) and (400) ones, resulting from the diamond structure of crystalline Germanium (c-Ge). However, Raman spectra of all three samples (Fig.3.9 b)) indicate the presence of Ge NCs, revealed by the asymmetric peaks located at about 298.9cm⁻¹ which can be identified as a confined phonon mode from Ge NCs. If compared with Raman spectra of bulk Ge ($\omega_{TO-LO} = 300.4$cm⁻¹, FWHM ≈ 3.0cm⁻¹, [39]), the film produced with $p_{Ar} = 4.0\times10^{-3}$mbar presents the best Ge crystalline structure [38].
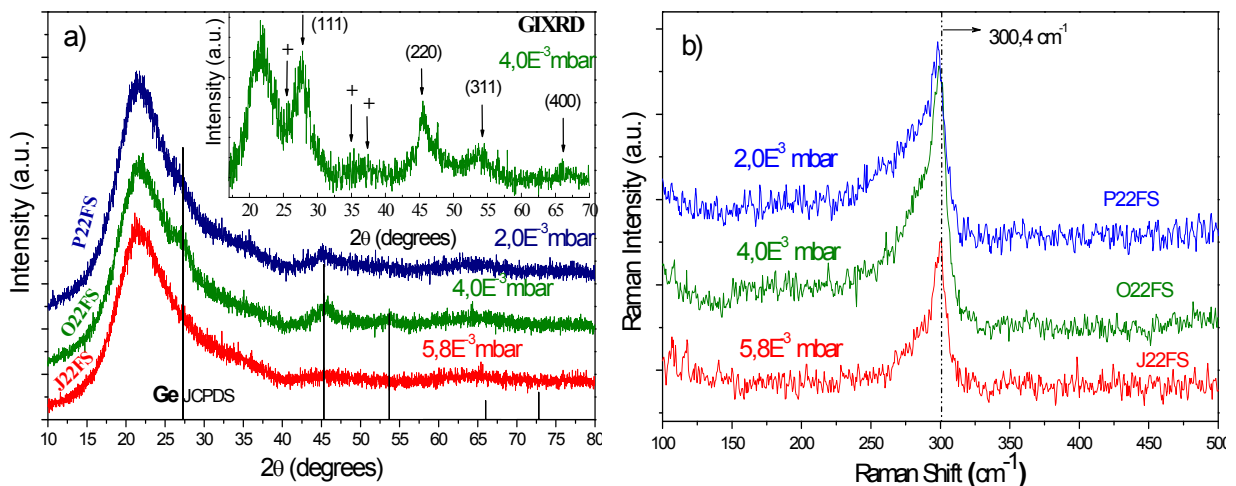
Fig.3.9 – a) X-Ray diffraction spectra and b) Raman spectra from as-deposited Ge doped Al₂O₃ films, grown on FS substrates with $P_{RF} = 50$W and three different Argon pressures. GIXRD spectrum from one of the samples (obtained with 1º theta incidence) is shown in the inset for comparison with the conventional XRD. The peaks marked with the symbol "+" are attributed to the possible presence of very small alumina NCs. Adapted from [38].

We saw previously, for the case of alumina films deposited over Si substrates, that using a deposition parameters of P_{RF} = 50W and p_{Ar} = 4.0×10^{-3}mbar originates amorphous alumina films (a-Al$_2$O$_3$). However, very small intensity "peaks", marked with "+", are visible at the inset GIXRD spectrum on Fig.3.9a). It suggests the possibility of having small grains of δ-Al$_2$O$_3$ and/or γ-Al$_2$O$_3$ on the matrix, although it was not expected that these deposition parameters would be able to induce any crystalline phases in the alumina matrix [39].

So, after finding that an Argon pressure value of 4.0×10^{-3}mbar would, most probably, be the best in obtaining Ge NCs doped alumina films, the study of the effect of a *RF*-sputtering power variation was then carried out, and for that we started to use silicon substrates instead of the FS ones. *RF* power values in between 40 to 100Watt were tested. Results are on Fig.3.10.
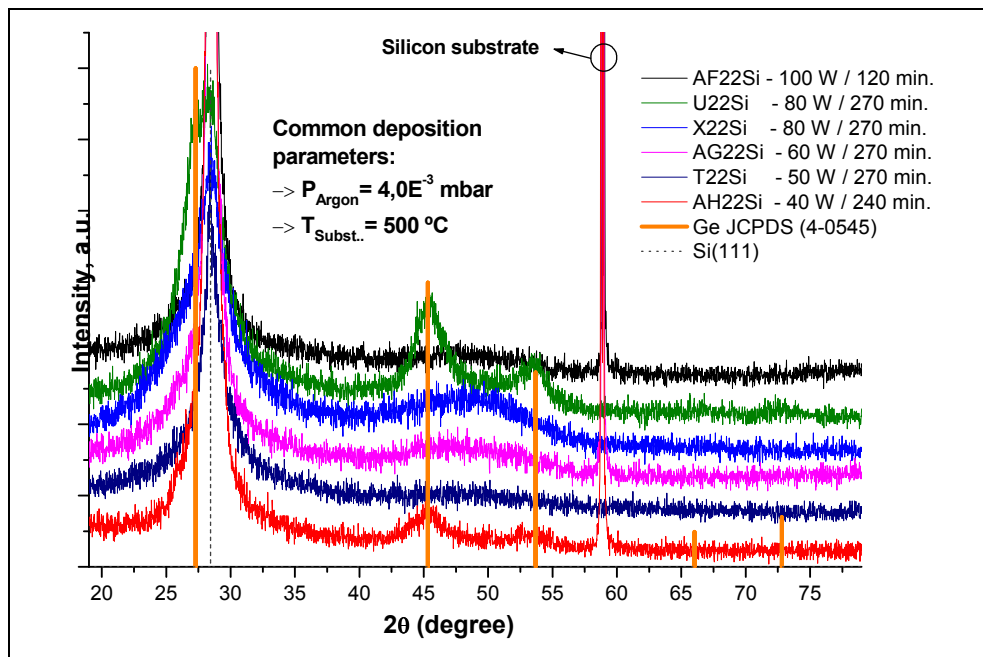
Fig.3.10 – X-ray diffractograms corresponding to the study of the different *RF*-sputtering power values that were tested. All samples corresponding to films deposited on Silicon(111) substrates, under the same Argon pressure (4.0×10^{-3}mbar) and substrate temperature (500ºC) deposition parameters.

The first data, presented on Fig.3.10, indicated that the value of P_{RF} = 80W may well be the best choice. The sample deposited with P_{RF} = 40W did also showed some potential to grow the Ge NCs doped Alumina layer films. However, the depositions performed with *RF*-sputtering power values lower than 50W and higher than 80W revealed to be quite difficult to perform due to the Power Supply instability when running behind those limits. For several times, plasma breakage during deposition time was observed. For this reason, the experiments

were then focused on testing only two different *RF*-sputtering power values: 50 and 80Watt. So, after excluding all the other potential values for the *RF*-sputtering power, another look at the XRD results on Fig.3.10 was done, but this time also including the Raman data of the selected samples. Results are presented below on Fig.3.11.

The XRD spectrum of sample T22Si on Fig.3.11a) shows that, when using Si(111) as substrate, the combination of a $p_{Ar} = 4\times10^{-3}$mbar and an $P_{RF} = 50$W might not be the best for obtaining films containing c-Ge. In fact, broad Raman spectrum with a band centred at $\approx$ 275cm⁻¹, like the one of sample T22Si on Fig.3.11b), are typical of a-Ge [38]. However, when applying 80Watts for the *RF*-sputtering power (keeping $p_{Ar} = 4\times10^{-3}$mbar), the presence of the Germanium phase with diamond structure becomes clear by XRD (111), (220), (311) and (331) reflections of the U22Si sample shown in Fig.3.11 a).
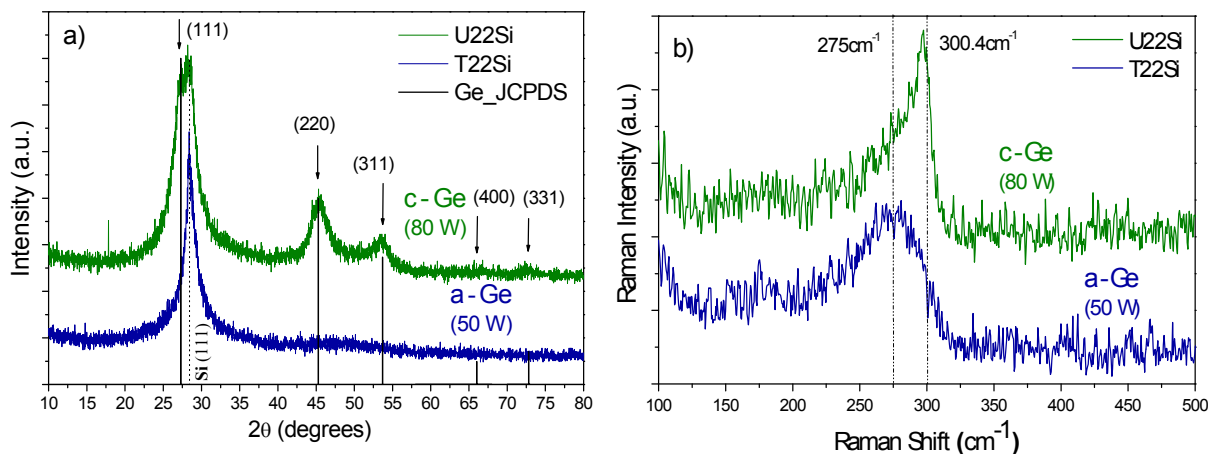
Fig.3.11 – X-ray diffractograms (a)) and Raman spectra (b)) from as-deposited Ge/Al₂O₃ films grown on Si(111) substrates using $p_{Ar} = 4\times10^{-3}$mbar; comparison between the central samples of series T and U. Adapted from [38].

The Raman spectrum revealing an asymmetric peak with a maximum peak at $\omega_1 = 297.3$cm⁻¹ (Fig.3.11 (b)) also confirms the presence of Ge NCs on sample U22Si. For this particular sample a rough estimate of the NC mean size (*D*) was made from the shift between ω_1 and ϖ_{LO-TO} using the bending parameters of bulk optical phonon dispersion curve β_{LO}, according to the formula $\omega_1^2 = \omega_{LO-TO}^2 - \beta_{LO}(\pi/D)^2$, which results in a value of $D \approx 3.5$nm [38]. This is quite in agreement with the mean size value of ~2.5nm that could be estimated from the XRD data using the *Debye-Scherrer* formula described above in equation 2.1. The β_{FWHM} value was determined after *Lorentzian* fitting the peaks. The table on Annex VI presents the

average NCs size of all the samples whose XRD spectra allowed for the estimation by fitting the peaks corresponding to the c-Ge phase.

Among all the as-deposited films over Si(111) substrates that were submitted to XRD analysis, only XRD spectra of samples from the series U and Z revealed the presence of c-Ge embedded in the dielectric matrix. Fig.3.12 presents the XRD spectra of samples U22Si and Z22Si as reference samples. For all the other series, it was always necessary to perform some kind of post-deposition annealing before the crystalline phase of Ge could be observed. However, if we take a close look to the deposition parameters of series Z, we find the following values: p_{Ar} = 5×10^{-3}mbar, P$_{RF}$ = 50W and T_{dep} = 500ºC. This was a little bit surprising, since the only different deposition parameter between T22Si and Z22Si samples was a very small change in the deposition Argon pressure from 4×10^{-3} to 5×10^{-3}mbar. So, a small variation of the deposition Argon pressure (p_{Ar}) may result on a similar effect to the one of increasing the radio-frequency sputtering power (P$_{RF}$). However, this is not a complete surprise, since it is known from the Vacuum Technology that, independently of the type of substrate being used, the deposition rate and quality of the grown films is mainly dependent both on the deposition pressure and sputtering power parameters, as well as of the type of used gas and the deposition temperature.
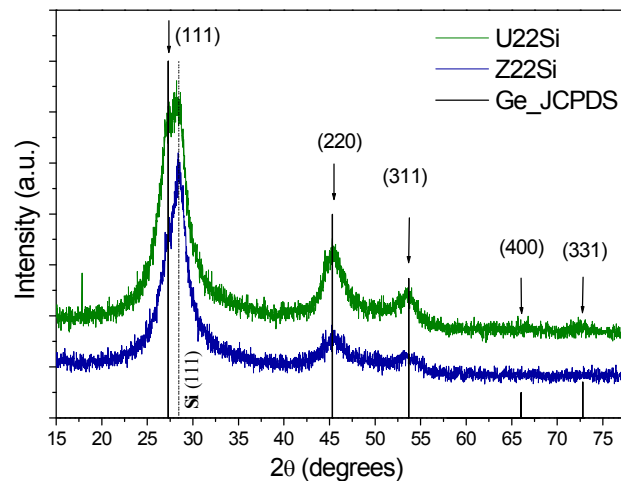
Fig.3.12 – X-ray diffractograms of the central samples from the only two series (U and Z) that showed the presence of Ge NCs in the as-deposited Ge/Al₂O₃ films on Si(111) substrates.

Study of the annealing parameters

Several dozens of samples were annealed using different annealing parameters. Different temperatures and atmospheres could be tested. Due to the conclusions found on chapter 3.2, the annealing temperatures were limited to 800 and 900ºC. The different used atmospheres

were Air, Argon (Ar) and Nitrogen (N_2). An evaluation considering different annealing atmosphere pressures was not done. A considerable number of the annealing experiments was performed very close to the limit time that I had to finish the experimental work. Because of that, and also because a lot of other data was already available and waiting for analysis, a big quantity of the annealed samples were not characterised, and so this study could not be more complete.

Regarding different annealing atmosphere gases, a first conclusion can be already stated: none of the samples annealed under N_2 atmosphere showed the presence of c-Ge. Conventional XRD performed at University of Minho did not showed the presence of c-Ge on those samples. One of them was sample V21SiR2N_2, annealed at 900ºC. This sample was analysed on the ESRF using GIXRD. The result is the one shown on Fig.3.13.
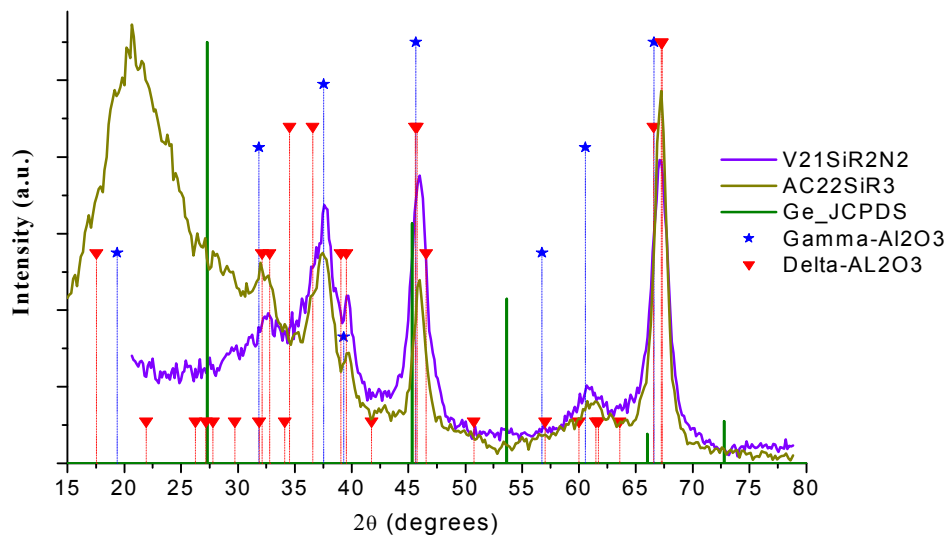
Fig.3.13 – GIXRD spectrum of sample V21SiR2N_2, annealed under Nitrogen atmosphere, where a mixture of gamma and delta alumina phases seems to be favoured. Spectrum from the alumina sample AC22SiR3 is shown for comparison.

It seems to indicate that an N_2 atmosphere is not a good one to grow Ge NCs. In fact, this spectrum is quite similar to the one of the alumina sample AC22SiR3, previously presented on Fig.3.2. So, one can conclude that annealing of Ge doped Al_2O_3 films under Nitrogen atmosphere may favours not the formation of the crystalline Ge phase but a mixture of gamma and delta alumina phases instead.

I believe that the fact that the annealing of sample V21SiR2N_2 had been done at 900ºC is not enough to cause such a drastic difference, when comparing the GIXRD results between

samples V21SiR2N$_2$ and V22SiR (annealed on a low pressure Air atmosphere and 800ºC). Fig.3.14 shows the GIXRD results of this sample before and after annealing on Air. An average Ge NCs size of approximately 5nm could be estimated from the annealed sample V22SiR after Lorentzian fitting of the XRD reflection peaks. On the as-grown sample perhaps some very small Ge crystals of around 1.3nm may already exist, but the a-Ge phase is, without any doubt, in majority.
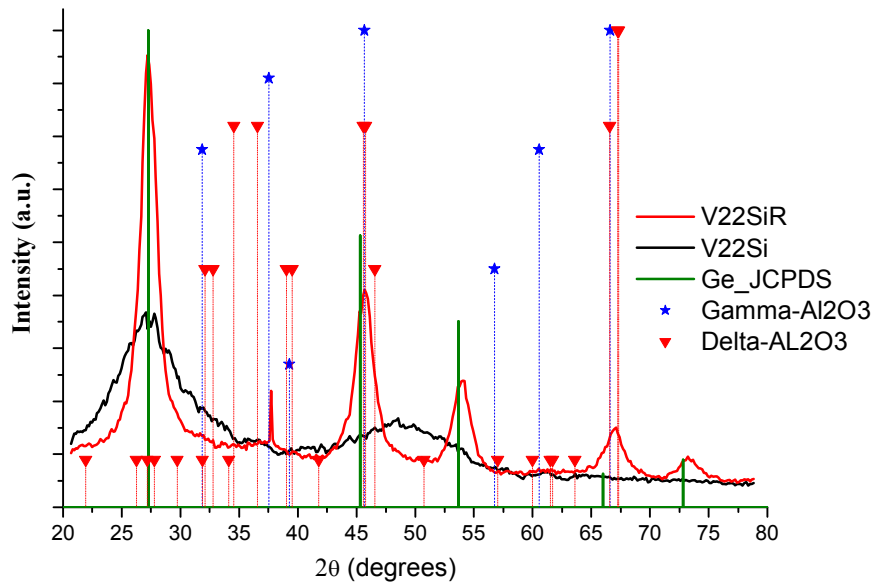
Fig.3.14 – GIXRD spectra of V22Si vs V22SiR, clearly reveals the annealing effect on the c-Ge when using an (low pressure) air atmosphere.

On the contrary to the samples annealed on Nitrogen atmosphere, some samples annealed under Argon atmosphere did revealed a development or an improvement of the Ge crystalline structure. That was the case of sample X32Si. The XRD pattern of sample X32SiRAr is shown on Fig.3.15 presented next page. Very sharp peaks at the Ge diffraction planes (220) and (311) are quite obvious. Using again the *Debye-Scherrer* formula, an average NCs size of approximately 22nm was estimated on this sample. This was, in fact, the highest size value estimated among all samples.
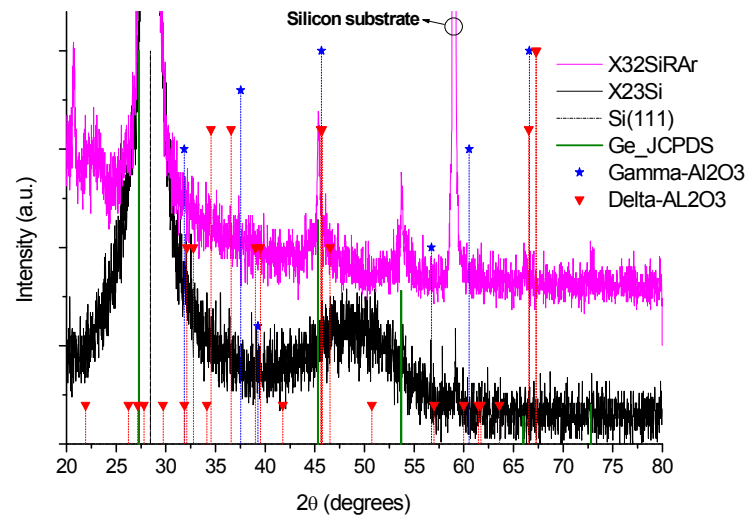
Fig.3.15 – XRD spectra of sample X23SiRAr vs X32Si, shown as the as-deposited reference sample. Figure clearly reveals the results of the annealing on the films crystallographic structure, namely the formation of c-Ge phase.
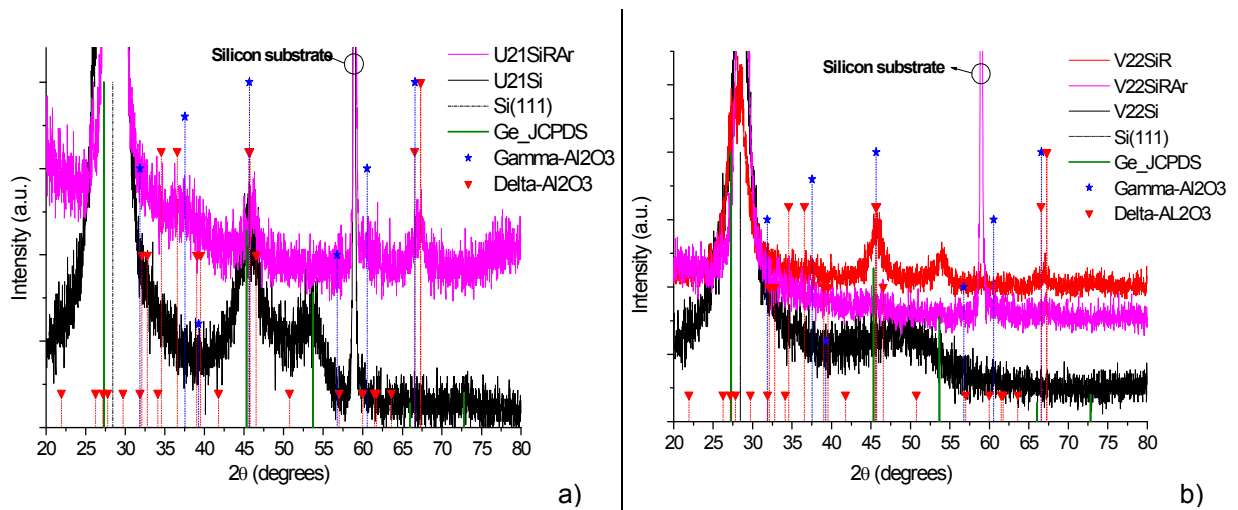
Fig.3.16 – XRD spectra of samples U21Si and V22Si were no reflection peaks were found for the annealing performed under Argon atmosphere. Spectrum from sample V22SiRAr in b) revealed no peaks besides the ones expected from the Silicon substrate, and the peaks on the spectrum of sample U21SiRAr in a) are most probably a result of some Alumina grains.

However, not all the samples annealed under Argon atmosphere revealed the same behaviour. For instance, XRD spectra of samples U21Si and V22Si, both also annealed under Argon atmosphere, do not revealed any XRD reflection peaks that could be attributed to Germanium (see Fig.3.16). So, the use of an Argon atmosphere during annealing may result on the formation and growth of Ge NCs, but not always. The reason why is still to understand. Although, one obvious explanation may lie on different Argon pressures during annealing, but

in the specific case of samples X32SiRAr and V22SiRAr that is not the case, since both of them were annealed at an Argon flow pressure of 5×10^{-3}mbar.

In the case of different annealing temperatures, some increasing of the Ge NCs size was observed when increasing the annealing temperature from 800 to 900ºC. That finding was revealed by the XRD data from samples BD22Si and BN22Si. Those results are shown on the XRD spectra of Fig.3.17 below. On the first case, sample BD22Si, the increase of the Ge NCs was rather small (estimated average NCs size increased only from 6.79 to 7.13nm), but on the second one the estimated average NCs diameter increased by ~54%, from 6.75 to 10.41nm.
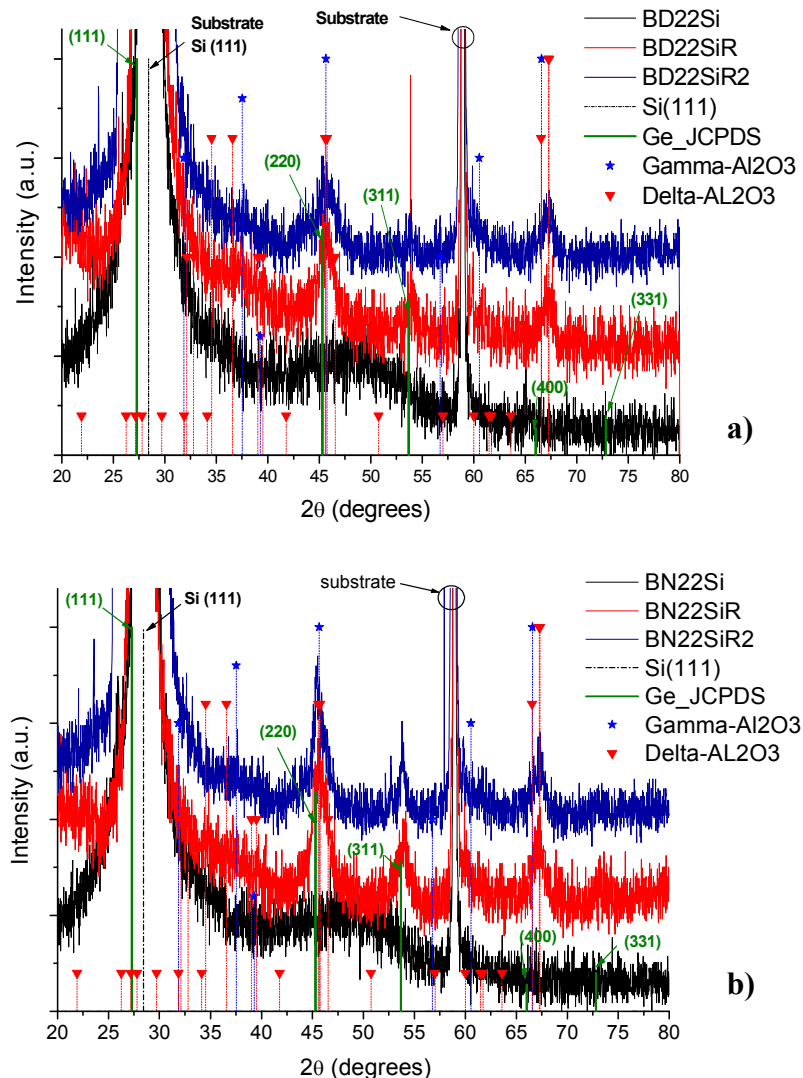
Fig.3.17 – XRD spectra of the central samples from series BD a) and BN b) presented as a function of the annealing temperatures of 800ºC (R) and 900ºC (R2). The increase of the average NCs size can be related to the increase of the annealing temperature.

After the experiments about the annealing parameters, it turned out possible to conclude that annealing at 800ºC, during one hour, under a low air pressure of approximately 4×10^{-3} mbar would be the best choice in obtaining good and reproducible Ge NCs doped Al$_2$O$_3$ layer. XRD and Raman results presented in Fig.3.18 are a good example to confirm it. Taking sample U12Si as an example, the NCs average size was estimated to increase up to 6.0nm. The peaks marked with "+" are, again, attributed to a crystalline phase(s) of the alumina matrix, most probably a mixture of δ and γ alumina phases. Also for practical, safety, time consuming and economical reasons, the best choice would have to be the annealing at 800ºC under air atmosphere. Most of the annealing was then performed using these parameters.
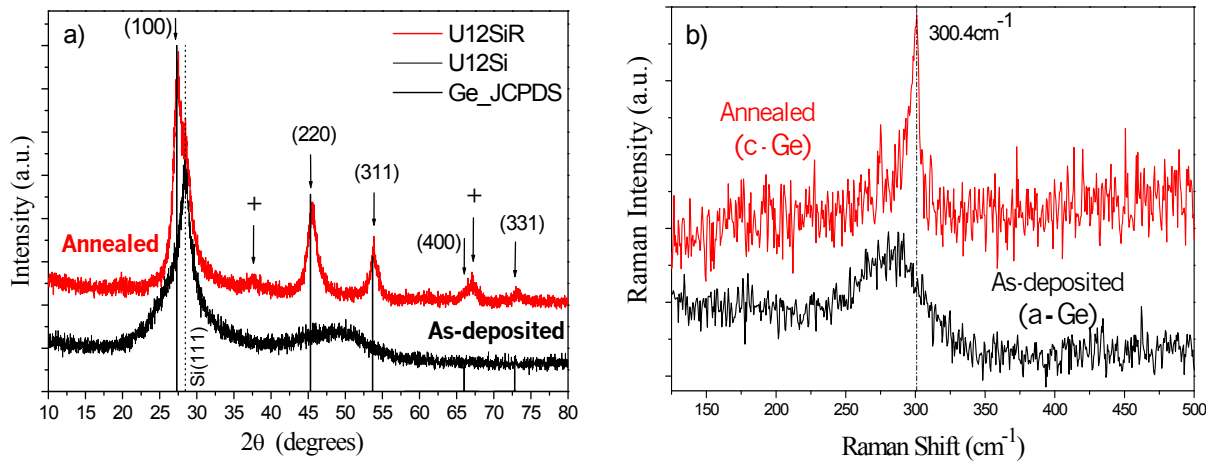
Fig.3.18 – X-ray difractograms (a) and Raman spectra (b) of the as-deposited (U12Si) and annealed (U12SiR) sample grown on a Si(111) substrate. Annealing was performed during one hour at 800ºC on a low air pressure atmosphere. Adapted from [38].

On the following and last figures concerning the X-ray diffraction data (Figures 3.19 to 3.21), some other XRD (and GIXRD) spectra for samples annealed at a low Air pressure and 800ºC for one hour are also shown. I consider them important because they represent some of the best obtained XRD spectra that one might expect to observe again when characterising Ge doped Al$_2$O$_3$ films. In principal, samples presenting results like this might be expectable to be able to present some NCs-dependent light emission.

For sample U22SiR (Fig.3.19), Ge NCs sizes in the range of 6.3 to 7.6nm could be estimated. This particular as-grown film already possessed Ge NCs with sizes of approximately 2.5nm. Besides samples from the deposition series U, only samples from series Z and AH also revealed, some how, Ge NCs on as-deposited films. Their average estimated

NCs size estimated by XRD was found to be around 2 to 3nm. However, the majority of the X-ray diffraction spectra from the as-grown films didn't presented any reflection peaks attributed to the presence of a Ge crystalline phase. When it comes to performing the structural characterisation of this kind of composite films, GIXRD is, by far, a better technique/geometry than the traditional θ-2θ XRD, and must be, in my opinion, used always whenever available.
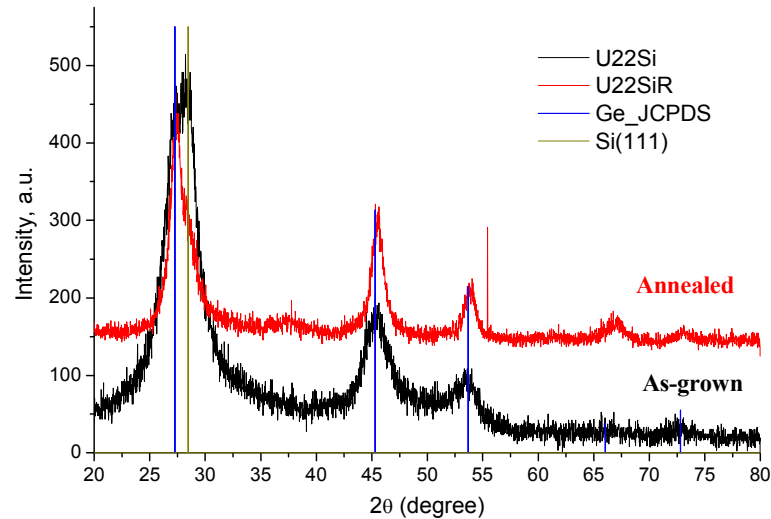
Fig.3.19 – Comparison between XRD spectra of as-grown vs. annealed U22Si sample. The Ge NCs mean diameter, estimated based on these spectra, showed a clear increasing improvement of the Ge Crystalline phase (*D* (U22Si) = 2.5nm; *D* (U22SiR) = 6.9nm).
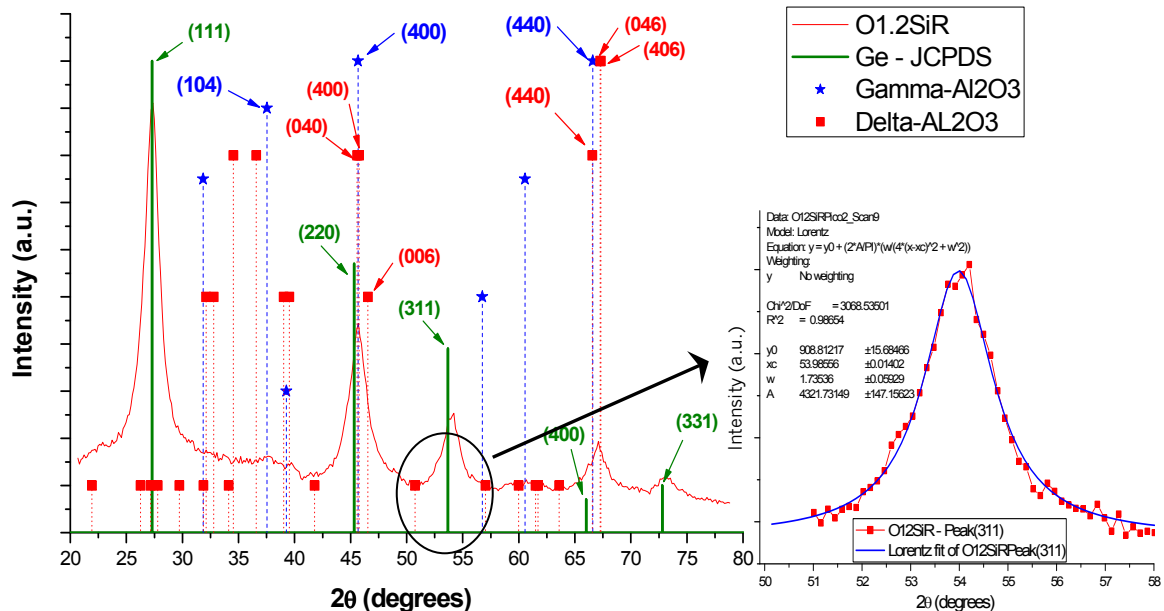
Fig.3.20 – GIXRD spectrum of the annealed sample O12SiR. Ge NCs with an average size of approximately 4.8nm could be estimated after Lorentzian fitting of all five Ge reflection planes. Fitting of the (311) reflection peak is shown as an example. If considering only this peak the estimated size would by 5.1nm.
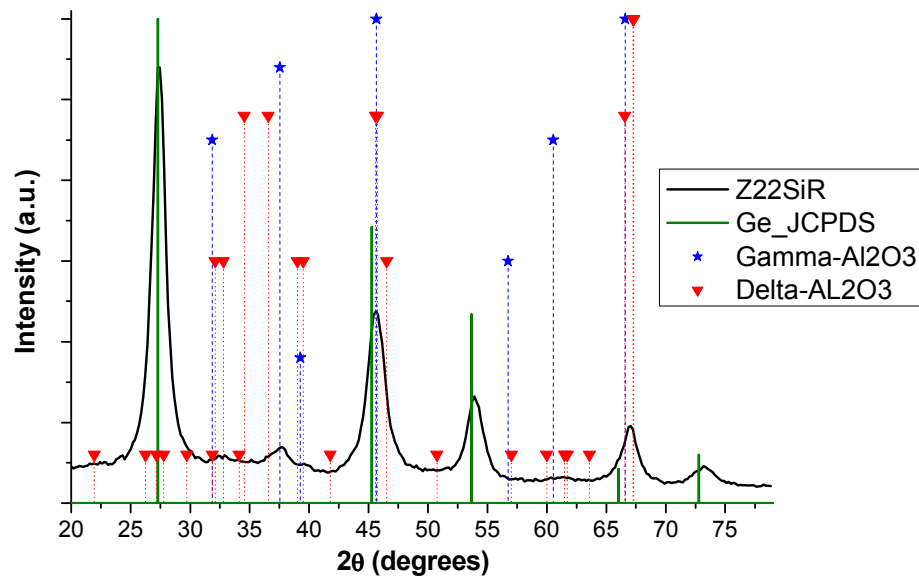
Fig.3.21 - GIXRD spectrum of the annealed sample Z22SiR. Average estimated Ge NCs size of 5.5nm could be estimated, after Lorentzian fitting all the five reflection peaks.

3.3.4 TEM, HRTEM, and SAD

The analysis of a limited number of samples when submitted to these techniques helped to confirm the existence of Ge nanocrystals embedded in the structure of the produced films. Besides that observation, real images visualisation of the Ge NCs embedded on the Al_2O_3 matrix allowed for NCs size measuring and counting.

Fig.3.22 (a) and (b) shows the cross-section view of U22SiR and Z22SiR samples, representing the typical morphology of the (annealed) Ge doped Al_2O_3 films. It is possible to observe that the density seems to decrease as the thickness increases, with the highest value (more compact structure) being close to the film-substrate interface. However, even if presenting slightly different thickness values, both U22SiR and Z22SiR cross-section morphology look pretty much the same. HRTEM pictures from sample U22SiR are shown on the insets (c) and (d). They show us two quite different Ge nanocrystals in size and shape: one spherical Ge NC with approximately 6nm in diameter (Fig.3.22 (c)) and an elliptical one about 13nm long by 7nm width (Fig.3.22 (d)).

Germanium NCs size distribution, determined by the NCs size measuring and counting based on the HRTEM pictures, was found to be much similar on both the analysed samples (U22SiR and Z22SiR, annealed using the same parameters). Average values of 8.0 ± 3nm for

sample U22SiR and 8.0 ± 2.6nm for sample Z22SiR could be calculated. Ge NCs size histograms are presented on Fig.3.23. Note that these NCs size values are in accordance with the Ge NCs mean diameter values estimated by the XRD and GIXRD spectra, despite the small discrepancy of values on sample Z22SiR.
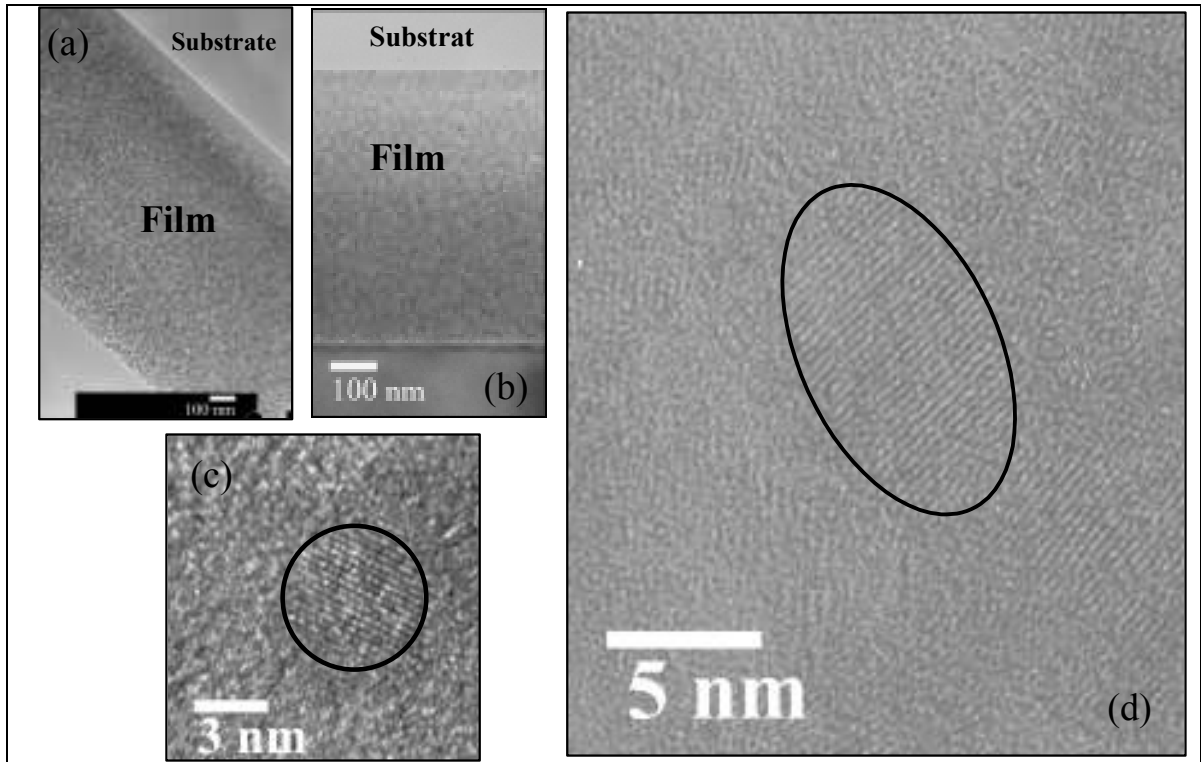
Fig.3.22 - TEM images from U22SiR (a) and Z22SiR (b). HRTEM images of film U22SiR (c) and (d) (data provided by U. Oslo).
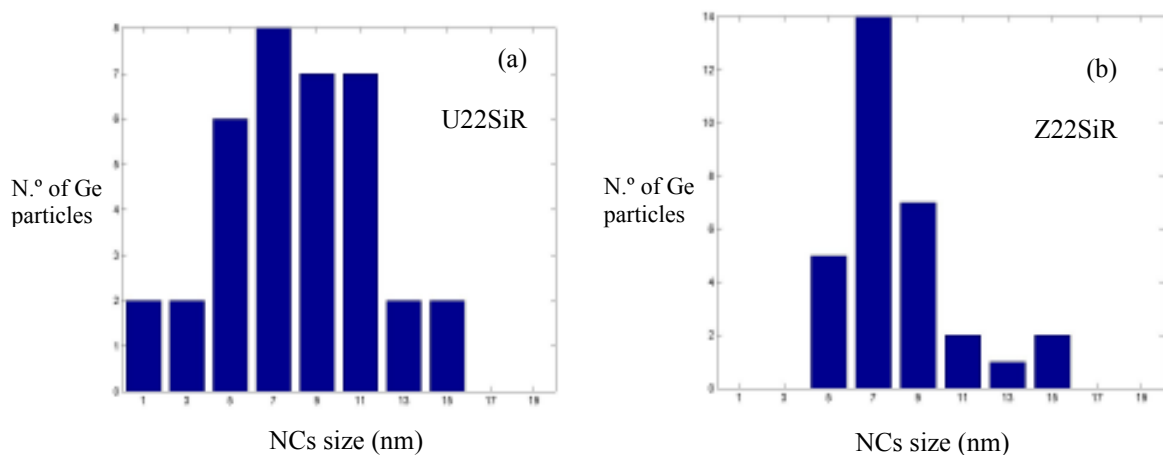
Fig.3.23 - Histograms of the NC sizes found in samples U22SiR (a) and Z22SiR (b) (data provided by U. Oslo).
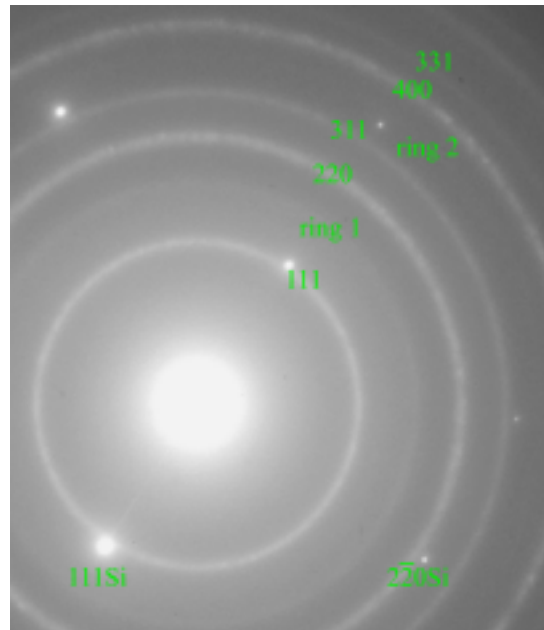
Fig.3.24 – Selected area diffraction from sample Z22SiR. The brighter spots are from the Si substrate while the rings are from the many different orientations of the Ge crystals. The rings labeled 'ring 1' and 'ring 2' are unidentified but could originate from an Al$_2$O$_3$ phase.

Based on the EDS results on Fig.3.25, the Ge to Al concentration was determined to be slightly about 1:3 for both samples (C_{Ge} / $C_{Al} \approx 33\%$) by using the following formula (Table 3.7 summarizes the results): C_{Ge} / C_{Al} = (k_{Ge} / k_{Al})*(I_{Ge} / I_{Al}), with k_{Ge} =0.5 and k_{Al} =1.3 [9].
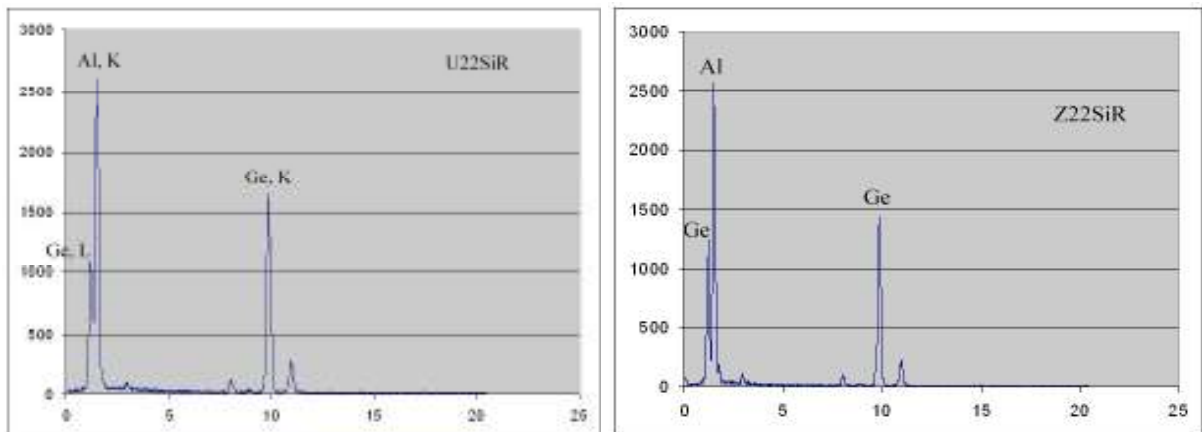
Fig.3.25 – EDS analysis of samples U22SR and Z22SiR.

Table 3.7 –	Sample	Ge, K Counts	Al, K Counts	C_{Ge}/C_{Al}
	U22SiR	30946	36109	**0.3296**
	Z22SiR	40421	47824	**0.3251**

---

[9] - From Olsen, A. (Institute of Physics Report Series, 85-10, 1985).

3.3.5 Absorption

Some absorption measurements were made as a way to find "promising" samples regarding the possibility of having some light emission phenomenon that might be associated to the presence of Ge NPs as part of the composition of the samples materials structure. Typical Absorption and Transmission spectrum as a function of wavelength is shown on Fig.3.26, for samples deposited over the Si(111) substrate a) and glass substrate b). Below approximately 1000nm Si substrate completely absorbs light, which is the reason why the transmission curves go to zero percent. Glass substrate is more than 90% transparent to light above 360nm, being transmission less than 1% only below 288nm.
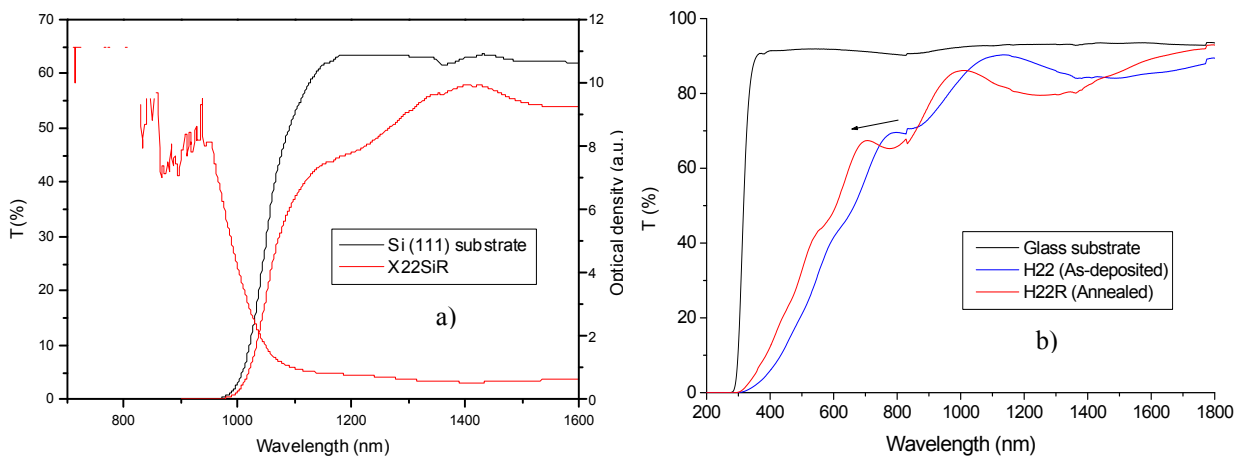
Fig.3.26 – Typical Absorption/Transmission spectra for samples deposited on a) Silicon or b) glass substrates.

Although the absorption spectra could look interesting to analyse, the fact is that it couldn't give much information. In fact, the kind of behaviour that was suppose to be observed for the samples deposited over glass should be something similar like in Fig.3.26b), where the optical absorption band limit is clearly shifted to the ultra-violet, with the possibility of attributing those shifts to quantum confinement effects. However, such was not clearly observed for the majority of the samples. The indirect transition nature of the Ge semiconductor together with the fact that the presence of Ge NCs on the samples deposited over glass substrates couldn't be assured (due to the impossibility of performing high temperature annealing on those samples) must have been the reason.

Nevertheless, it was possible (in what was the very last measurement performed in the aim of this Thesis) to perform Ellipsometry measurements, for a limited number of samples, in new equipment at the Physics Departmentof University of Minho. Samples AE22Si (Alumina), and V12Si, Z22Si and Z22SiR were chosen, as well as a small peace of Ge material that was used as target for the Ge doped Al$_2$O$_3$ films. A natural SiOx layer formed on the surface of the low resistivity Si(111) substrates was considered in the ellipsometry fittings. Based on the spectra presented on Fig.3.27, it was possible to obtain the spectral dependences of a) the refractive index and b) the extinction coefficient of Ge QDs. The dependences were obtained by processing the spectral ellipsometry data using classical dispersion based on Lorentz diffusion model for the alumina (AE22Si) film, and a Forouhi-Bloomer formulation derived expression for the other films.
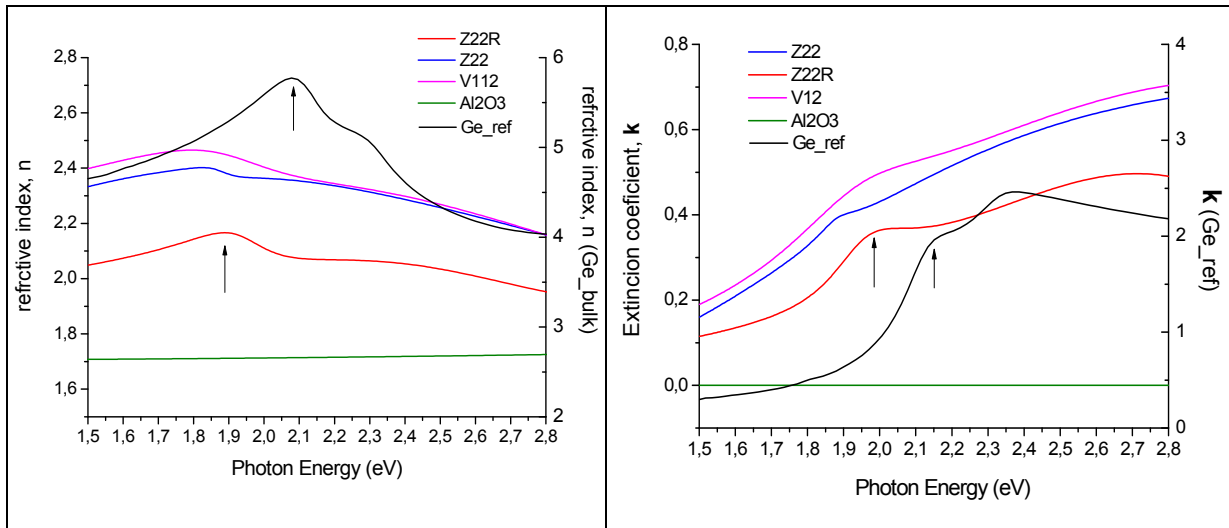
Fig.3.27 – Spectral dependences of a) the refractive index (n) and b) the extinction coefficient (k) of the Ge QDs.

As we can see from the above spectra, it seems that the refractive index (n) decreases as the Ge NCs size increases. The spectrum of the extinction coefficient (k), which is proportional to the absorption coefficient in the first order, could provide useful information of band-structure critical point transitions. However, very few works using ellipsometry to study a system with this type of materials structure have been published [3]. On the contrary to absorption measurements, the ellipsometry results seem quite interesting and consistent, but more studies need to be carried out in order that more concrete explanations can be given.

3.3.6 Photoluminescence

The PL measurements were the ultimate characterisation analyses that were performed. A limited number of samples could be measured but, yet, some interesting and promising results could be found. The best PL result that could be encountered was in sample U2.2SiR, and it is published in the article corresponding to reference [10]. The results and discussion that are presented here below are, in a way, a summary of the results contained at that paper. It is a good start, although, to show the PL spectrum of the Si(111) substrate that was used to grow the films (please see Fig.3.28). This was considered to be the reference PL spectrum before measuring the Ge doped Alumina films.
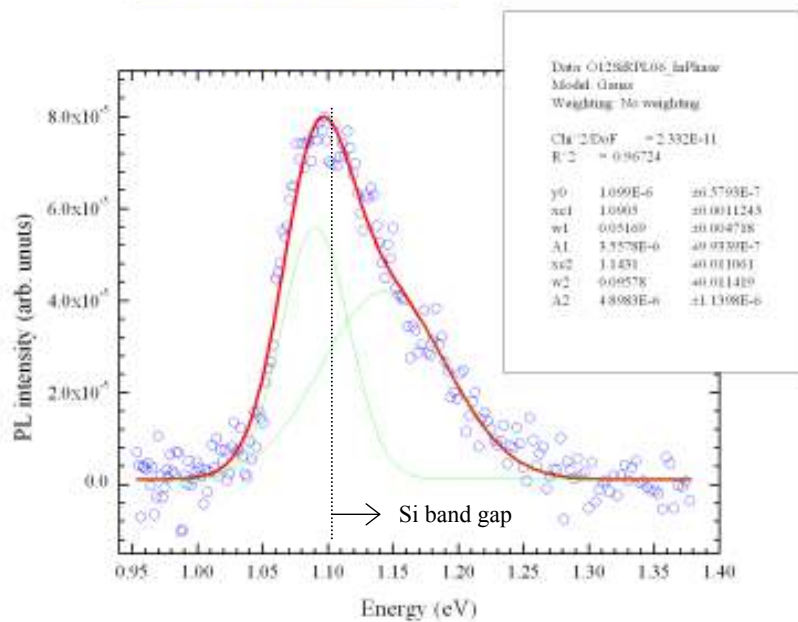
Fig.3.28 – Reference PL spectrum for the Si(111) substrates. A line with the Silicon band gap value at 1.107eV is shown as reference. Peak is not symmetrical, so it is shown fitted by two Gaussians.

Regarding the PL spectrum for sample U2.2SiR, it is shown on Fig.3.29 presented next page. That spectrum represents the typical PL spectrum obtained from the produced Ge/Al₂O₃ structures when measured at very low temperatures.
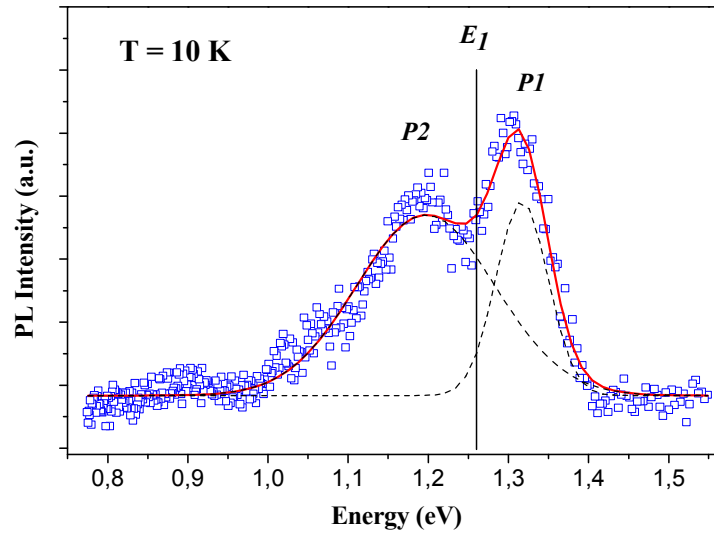
Fig.3.29 – A typical PL spectrum from Ge NCs/Al_2O_3 system, obtained at 10K for sample U22SiR. Adapted from [10].

The spectrum is fitted by the convolution of two Gaussians centered at 1.31 eV (P1) and 1.19 eV (P2). It suggests the participation of two NCs sizes to the overall emission. In fact, the estimated average Ge NCs size for sample U22SiR range between 6.3 and 7.6nm (see Annex VI), which in any case corresponds to an average Ge NCs radius largely smaller than the effective Bohr radius of 24,3nm.

Applying equation 1.1, the Kayanuma model presented on chapter1, and using E_g= 0.7469eV (at 10K), R = 3.5nm and μ = 0.028m_0, one obtain E_1 = 1.26eV. This energy value is between 1.31eV (P1) and 1.19eV (P2) locations of the two Gaussians that were used to fit the PL spectrum obtained at 10K (see Fig.3.29). Two arguments could be advanced to explain the PL spectrum. The first hypothesis is that the different PL energy peaks result from a bi-modal distribution NC sizes. This explanation has some credibility, since the size distribution that could be obtained with TEM for this sample cannot easily be obtained with precision and high statistical accuracy, and the estimate of the NCs diameter from XRD measurements are an approximation having, of course, some degree of error. These different observed PL peaks (P1 and P2) could express a multi-modal distribution, phenomenon already observed in InAs/GaAs systems [40] e [41]. The second argument is that P1 and P2 are due to defects in Al_2O_3, which could also participate to the PL emission. In fact, annealing the samples leads to the decomposition of GeO_2 in the Al_2O_3 matrix. Non-bridging oxygen centers can trap electrons and became light emitting centers. This phenomenon was observed by Wan et al.

[19] in CV characteristics of Ge/Al$_2$O$_3$ structure, where these centers became negatively charged.

It is known that the band gap of bulk Ge evolutes from 0.747eV at 10K to 0.66eV at 300K. Ge NCs are expected to have the same thermal behavior. Assuming that P1 corresponds to ground states recombination of Ge NCs, Fig.3.30 shows the evolution of P1 position with the temperature compared with the evolution of Ge bulk calculated with the empirical *Varshni* relationship [42]:

$$E_g(T) = E_g(0) - \frac{\alpha T^2}{\beta + T},$$

where β is the Debye constant for Ge (360K), and α is a constant (4×10^{-4}). Fig.3.30 illustrates the red shift of P1 when increasing the temperature. We can see also that it follows slightly the evolution of the Ge band gap. This gives some weight to the argumentation about the quantum confinement hypothesis, meaning that the observed peaks may be signatures of Ge NCs [10].
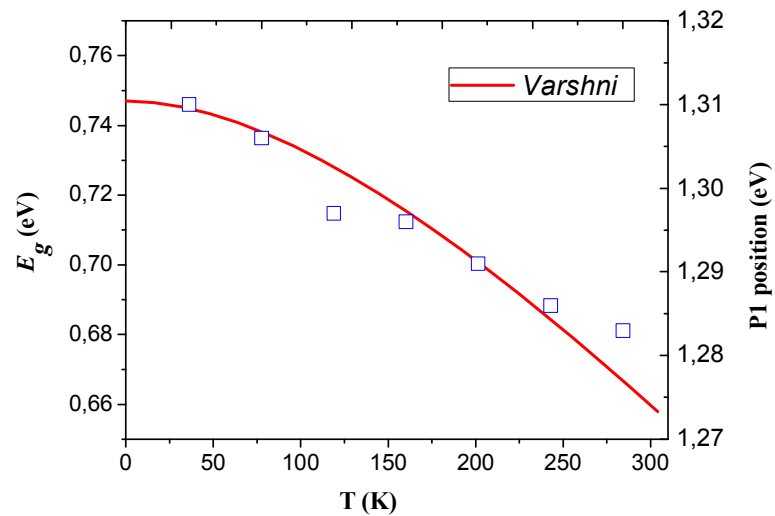
Fig.3.30 – Evolution of the peak P1 with temperature (squares), compared with the red shift of the Ge bulk band gap (E$_g$), calculated with *Varshni* relationship (continuous line). Adapted from [10].

Fig.3.31 shows the evolution of the normalized PL intensity of the peak P1, with a slight increase at low temperature (T<130K) followed by an exponential quenching. A practically identical behavior was found when plotting the peak P2 against the temperature. The slight growth at low temperature is usually explained by a thermal activation of carriers captured at traps in the matrix [43] e [44]. The photoluminescence (PL) quenching effect is commonly

attributed to thermal escape of the carriers from NCs to the surrounding matrix, followed by their non-radiative recombination.
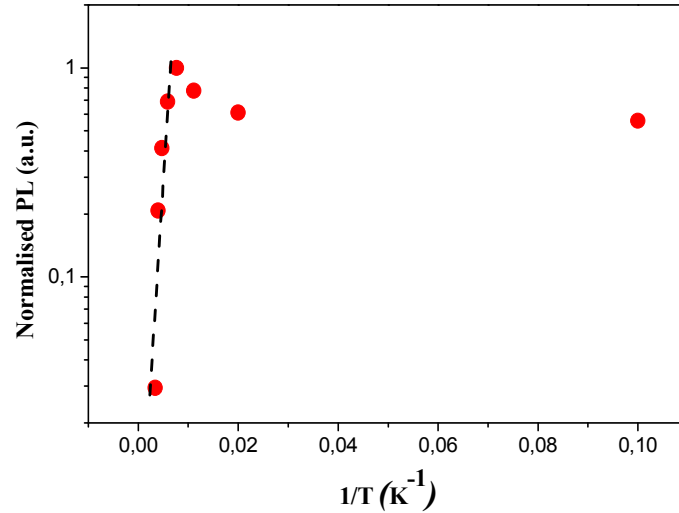
Fig.3.31 – Temperature dependence of the peak P1 in between 10 to 300K. The dashed line is guide for eyes. Adapted from [10].

The PL intensity for P1 tends towards a straight line (T >130K) as illustrated in Fig.3.31. This line is characteristic of an exponential quenching $\propto \exp(E_a / kT)$ owing to the thermal escape from the dots, where E_a is the activation energy. It has been deduced by measuring the slope of the dashed line in Fig.3.31, giving a value of 28meV. If the main thermal escape process was excitons dissociation from the bound NC state to the Al₂O₃ barrier, the fitted E_a should be close to the confinement energy. However, the obtained value of 28meV is probably too small to be attributed to hole jumps over the potential barrier to the matrix. Another possibility is to assume that some other traps, already present in the matrix, participate in the electron or hole escape from the dots [10].

Chapter 4
Conclusions

4. Conclusions

The production of Ge doped alumina films by sputtering was the first objective of the work performed in the aim of this thesis. The second goal of this work was to be able to fully characterise the produced films. Extended characterisation of the produced films were performed by analysing all data obtained by the several structural and optical characterisation techniques that were used, namely XRD, Raman, SAD, SEM, TEM, HRTEM, XPS, RBS, Absorption, and Photoluminescence.

It was proved that different deposition and annealing parameters, namely RF-power, deposition Argon pressures, as well as annealing temperature and gas atmosphere, gives rise to films with different structural and optical properties. In general, alumina films produced with RF-power of 50W and deposition Argon pressure of about 4.0×10^{-3} mbar tend two be mostly amorphous, even if annealed up to 1000ºC, while alumina films deposited with 80W *RF*-power and 2.0×10^{-3} mbar Argon pressure seems to have a tendency to form $gamma-Al_2O_3$ and delta-Al_2O_3 grains. $Gamma-Al_2O_3$ seems to be predominant until 900ºC annealing temperature, while for 1000ºC an increase of the $delta-Al_2O_3$ phase was observed. More detailed analysis of the XRD spectra, allowed to conclude that the nucleation of the first Al_2O_3 grains for the samples produced with $P_{RF} = 50W$ and $p_{AR} = 4.0 \times 10^{-3}$ mbar (AC series) must have formed originally during the annealing treatment performed at 900ºC, while for the sample produced with $P_{RF} = 80W$ and $p_{AR} = 2.0 \times 10^{-3}$ mbar (series AE) alumina grains probably started to form already during deposition at 500ºC.

Also, amorphous Germanium (a-Ge) or crystalline Germanium (c-Ge) nanoparticles doped alumina films could be grown/obtained under certain deposition and annealing conditions. Those parameters are fully discussed on chapter 3.3.3, and some of those conclusions are published on [38]. It was observed that when using deposition parameters of $P_{RF} = 80W$ and $p_{AR} = 4.0 \times 10^{-3}$ mbar, together with a substrate temperature during growth of 500ºC, the composite films will already present some small Ge NCs with potential for presenting light emission properties. A similar composite film was obtained using the deposition parameters of $P_{RF} = 50W$ and $p_{AR} = 5.0 \times 10^{-3}$ mbar, but when using $P_{RF} = 50W$ and $p_{AR} = 4.0 \times 10^{-3}$ mbar no Ge NCs were observed in as-grown films. In fact, only the two former processing conditions produced as-grown samples that clearly revealed the presence of small

Ge NCs, with average size in the range of 2.5 to 3.0 nm, estimated by using the Debye-Scherrer formula after fitting the Ge diffraction peaks of the XRD spectra.

Post deposition annealing under different atmospheres was also investigated. Average Ge NCs size in between approximately 5 to 7nm was achieved when annealing at 800ºC on a low-pressure air atmosphere. Some increasing of the Ge NCs size up to about 10.5nm was observed when rising the annealing temperature from 800 to 900ºC. Ge NCs size distribution of 8.0±3nm could be calculated based on the HRTEM pictures. That value was found to be much similar for both the analysed samples (annealed using the same parameters), on which Ge NCs already existed before annealing. Ge NCs size distribution values are in accordance with the Ge NCs mean diameter values estimated by the XRD and GIXRD spectra. An higher value (~22nm) was obtained when annealing under Argon atmosphere, but this was not a consistent result since other Argon-annealed samples did not revealed any Germanium nanocrystals. All the annealing in which Ge NCs was found to exist was performed under annealing gas flow pressures equal or lower than 5×10^{-3}mbar. None of the samples annealed under Nitrogen atmosphere presented Ge NCs on their structures.

According to the EDS results, the Ge to Al concentration was determined to be about 1:3 ($C_{Ge} / C_{Al} \approx 33\%$). For the analysed samples, Ge atomic percentage values in between 14 to 20% were determined by RBS. Among those samples, RBS allowed to conclude that both the deposition parameters and the position of the sample over the target are equally important for the outcome of the Ge at.% value on each individual sample. The average density of the Ge/Al$_2$O$_3$ composite films deposited over Si substrates was calculated by RBS to be in the range of 2.32 to 2.86g/cc. For comparison, the density of ceramic Al$_2$O$_3$ is 3.97g/cc, and the density of a sapphire monocrystal is about 5.3g/cc.

It was found by in depth XPS analysis that Ge Oxide is present in the samples, but only as a surface phenomenon. In terms of uniformity and Ge concentration, XPS results indicated that similar samples are uniform and maintain the concentration in depth.

Hopefully, we could conclude about the existence of some kind of light emission that might be directly related to the Germanium nanocrystals photoemission. PL measurements indicate an emission that could be related to excitonic recombination in the Ge NCs. The temperature dependence of the PL demonstrates the confinement effect and confirmed our hypothesis, as discussed on chapter 3.3.6 and published on reference [10].

References

1. Rocksby H.P., J.Soc.Glass Tech., 1932. **16**: p. 171.

2. Ekimov, A.I., A.L. Efros, and A.A. Onushchenko, *Quantum size effect in semiconductor microcrystals.* Solid State Communications, 1985. **56**(11): p. 921-924.

3. Li, P.-W., et al., *Optical and Electronic Characteristics of Germanium Qunatum Dots Formed by Selective Oxidation of SiGe/Si-on-ininsulator.* Japanes Journal of Applied Physics, 2004. **43**(11A): p. 7788-7792.

4. Heath J.R., Shiang J.J., and A. A.P., J. Chem. Phys., 1994. **101**: p. 1607.

5. Rosseti, R.H., G.M. Gibson, and L.E. Brus, J. Chem. Phys., 1985. **83**: p. 1406.

6. Kayanuma, Y., Physical Review B, 1988. **38**: p. 9797.

7. Alivisatos, A.P., *Semiconductor Clusters, Nanocrystals, and Quantum Dots.* Science, 1996. **271**(5251): p. 933-937.

8. Park, B., et al., *Memory characteristics of MOS capacitors with Ge nanocrystal-embedded Al2O3 gate layers.* Solid State Communications, 2007. **143**(11-12): p. 550-552.

9. Yilmaz, E., I. Dogan, and R. Turan, *Use of Al2O3 layer as a dielectric in MOS based radiation sensors fabricated on a Si substrate.* Nuclear Instruments and Methods in Physics Research Section B: Beam Interactions with Materials and Atoms, 2008. **266**(22): p. 4896-4898.

10. Caldelas, P., et al., *Structural and Optical Properties of Ge Nanocrystals Embedded in Al2O3.* Journal of Nanoscience and Nanotechnology, 2008. **8**(2): p. 572-756.

11. Zhu, Y. and P.P. Ong, *Preparation and photoluminescence of thin films of Ge nanoparticles embedded in Al2O3 matrices.* Journal of Physics-Condensed Matter, 2001. **13**(18): p. 4075-4080.

12. Shah, S.I., *Sputtering: Introduction and General Discussion*, in *Handbook of Thin Film Process Technology*, I.P. Ltd, Editor. 1995.

13. GENCOA.com, *What is sputtering?*

14. http://hyperphysics.phy-astr.gsu.edu/hbase/hframe.html, *HyperPhysics.* 2005, C.R. Nave, Georgia State University.

15. Penfold, A.S., *Magnetron Sputtering*, in *Handbook of Thin Film Process Technology*, I.P. Ltd, Editor. 1995.

16. Maeda, Y., *Visible Photoluminescence from Nanocrystallite Ge Embedded in a Glassy Sio2 Matrix - Evidence in Support of the Quantum-Confinement Mechanism.* Physical Review B, 1995. **51**(3): p. 1658-1670.

17. Choi, W.K., et al., *Raman and photoluminescence characterization of Ge nanocrystals in co-sputtered Ge+SiO2 system.* Materials Science and Engineering: C, 2001. **16**(1-2): p. 135-138.

18. Sharp, I.D., et al., *Structural properties of Ge nanocrystals embedded in sapphire.* Journal of Applied Physics, 2006. **100**(11): p. -.

19. Wan, Q., et al., *Structural and electrical characteristics of Ge nanoclusters embedded in Al2O3 gate dielectric.* Applied Physics Letters, 2003. **82**(26): p. 4708-4710.

20. Jensen, J.S., et al., *Coupling between Ge-nanocrystals and defects inSiO(2).* Journal of Luminescence, 2006. **121**(2): p. 409-412.

21. Singha, A., *A hybrid model for the origin of photoluminescence from Ge nanocrystals in a SiO2 matrix.* Semicond. Sci. Technol., 2006. **21**: p. 1691-1698.

22. Choi, W.K., et al., *Formation of germanium nanocrystals in thick silicon oxide matrix on silicon substrate under rapid thermal annealing.* Journal of Crystal Growth, 2006. **288**(1): p. 79-83.

23. Wang, Y.Y., et al., *Raman scattering and room-temperature visible photoluminescence from Ge nanocrystals embedded in SiO2 thin films.* Materials Letters, 1996. **29**(1-3): p. 159-164.

24. Stoiber, M., et al., *Germanium nanoclusters in silica thin films.* Materials Science and Engineering B-Solid State Materials for Advanced Technology, 2000. **69**: p. 468-473.

25. Vaz, F., *Preparação e caracterização de filmes finos de Ti$_{1-x}$Si$_x$N$_y$, crescidos por pulverização catódica reactiva em magnetrão*, in *PhD thesis in Physics*. 2000, University of Minho: Braga.

26. http://materials.binghamton.edu/labs/xray/xray.html, *X-ray analysis of a solid*. 1997, M.S. Whittingham, Binghamton University.

27. Rolo, A.G., *Modos Vibracionais Ópticos em Nanocristais de Semicondutores: Estudos por Espectroscopias de Infravermelho e Raman.*, in *PhD thesis in Physics*. 2003, University of Minho: Braga.

28. Cullity, B.D., *Elements of X-ray Diffraction*. 2nd. ed, ed. I. Addison-Wesley Publishing Company. 1978, Reading Massachussets.

29. http://acswebcontent.acs.org/landmarks/front_t2.html, *Frontiers of Knowledge*. 2007, American Chemical Society.

30. http://www.kosi.com/raman/resources/tutorial/, *Raman Tutorial*, Kaiser Optical Systems, Inc.,.

31.   http://www.fisica.ufc.br/raman/, *Raman Scattering Laboratory*, Universidade Federal do Ceará.

32.   Barradas, N.P., C. Jeynes, and R.P. Webb, *Simulated annealing analysis of Rutherford backscattering data.* Applied Physics Letters, 1997. **71**(2): p. 291-293.

33.   http://neutron.ujf.cas.cz/vdg/home.html, *RBS - Rutherford Backscattering Spectrometry*, Laboratory of Nuclear Analytical Methods, Czech Republic.

34.   http://www.uksaf.org/tech/xps.html, *XPS - X-ray Photoelectron Spectroscopy, compiled by Christopher Walker, from the University of York.* 2007, UK Surface Analysis Forum.

35.   Materials Evaluation and Engineering, I., ed. *Handbook Of Analytical Methods For Materials*. 2006: Plymouth, MN.

36.   http://inventors.about.com/od/pstartinventions/a/Photoluminescen.htm, *Photoluminescence.*

37.   Zywitzki, O., et al., *Effect of the substrate temperature on the structure and properties of Al2O3 layers reactively deposited by pulsed magnetron sputtering.* Surface & Coatings Technology, 1996. **82**(1-2): p. 169-175.

38.   Caldelas, P., et al., *Raman and XRD studies of Ge nanocrystals in alumina films grown by RF-magnetron sputtering.* Vacuum, 2008. **82**(12): p. 1466-1469.

39.   Conde, O., et al., *HRTEM and GIXRD studies of CdS nanocrystals embedded in Al2O3 films produced by magnetron RF-sputtering.* Journal of Crystal Growth, 2003. **247**(3-4): p. 371-380.

40.   C. Lobo, R.L., S. Marcinkevicius, W. Yang, P. C. Sercel, X. Z. Liao, J. Zou and Cockayna, Physical Review B, 1999. **60**: p. 16647.

41.   Y. J. Yu, I.T.J., J. C. Woo, and W. Jhe, Applied Physics Letters, 2005. **87**: p. 143108.

42.   Varshni, Y.P., Physical Review B, 1967. **34**(149).

43.   N.V. Baidus, A.C., M. J. M. Gomes, M. I. Vasilevskiy, P. B. Demina, E. A. Esakova, and B.N. Zvonkov, Applied Physics Letters, 2005. **87**(53109).

44.   A.S. Bhatti, V.N.A., P.Swaminathan, J. S. Palmer, and J. H. Weaver., Applied Physics Letters, 2007. **90**(011903).

Annex I

Properties of Alumina, Germanium and Silicon bulk materials
(Adapted from *MatWeb -Material Property Data*, http://www.matweb.com/search/search.asp)

Germanium (Ge), 100%

A much more detailed and complete data, including temperature dependence spectra, can be found at http://www.ioffe.ru/SVA/NSM/Semicond/index.html.

Physical Properties	Metric	Comments
Density	5.3234 g/cc	
a Lattice Constant	5.65754 Å	
Volume Compressibility, 10^-10 m²/N	0.768	
Mechanical Properties		
Knoop Microhardness	7644	N/mm² Microhardness
Modulus of Elasticity	130 GPa	Average of three axes
Poisson's Ratio	0.3	Calculated
Shear Modulus	50 GPa	Average of three axes
Electrical Properties		
Electrical Resistivity	5e-005 ohm-cm	
Magnetic Susceptibility	-1.2e-007	Atomic (cgs)
Critical Superconducting Temperature	5.35 K	at 11.5 GPa pressure
Dielectric Constant	16	
Band Gap	0.67 eV	
Electron Mobility, cm²/V-s	3800	
Hole Mobility, cm²/V-s	1820	
Thermal Properties		
Heat of Fusion	478 J/g	
CTE, linear 20°C	6.1 µm/m-°C	
CTE, linear 20°C	6.1 µm/m-°C	
Specific Heat Capacity	0.3219 J/g-°C	
Thermal Conductivity	64 W/m-K	
Melting Point	937.4 °C	
Heat of Formation	291 kJ/mol	
Debye Temperature	101 °C	
Optical Properties		
Refractive Index	3.99	at 589 nm
Descriptive Properties		
CAS Number	7440-56-4	
Crystal Structure	Cubic	Diamond Structure - Space Group Fd3m

Silicon (Si), 100%

A more detailed and complete data, including temperature dependence spectra, can be found at http://www.ioffe.ru/SVA/NSM/Semicond/index.html.

Physical Properties	Metric	Comments
Density	2.329 g/cc	
a Lattice Constant	5.43072 Å	
Molecular Weight	28.086 g/mol	
Volume Compressibility, 10^-10 m²/N	0.306	
Mechanical Properties		
Knoop Microhardness	11270	N/mm² Microhardness
Modulus of Elasticity	112.4 GPa	
Compressive Yield Strength	120 MPa	
Bulk Modulus	98.74 GPa	
Poisson's Ratio	0.28	
Shear Modulus	43.9 GPa	Calculated
Electrical Properties		
Electrical Resistivity	0.01 ohm-cm	
Magnetic Susceptibility	-3.9e-006	Atomic (cgs)
Critical Superconducting Temperature	6.7 - 7.1 K	6.7-7.1 K from 12.0-13.0 GPa pressure
Dielectric Constant	11.8	
Band Gap	1.107 eV	
Electron Mobility, cm²/V-s	1900	
Hole Mobility, cm²/V-s	500	
Thermal Properties		
Heat of Fusion	1800 J/g	
CTE, linear 20°C	2.49 µm/m-°C	at 25°C
CTE, linear 250°C	3.61 µm/m-°C	at 227°C
CTE, linear 500°C	4.15 µm/m-°C	at 527°C
CTE, linear 1000°C	4.44 µm/m-°C	at 1027°C
Specific Heat Capacity	0.702 J/g-°C	
Specific Heat Capacity	0.794 J/g-°C	Gas
Thermal Conductivity	124 W/m-K	
Melting Point	1412 °C	
Boiling Point	3265 °C	
Heat of Formation	0 kJ/mol	Crystal
Heat of Formation	450 kJ/mol	Gas

Debye Temperature	372 °C	
Optical Properties		
Refractive Index	3.49	at 589 nm
Reflection Coefficient, Visible (0-1)	0.3 - 0.7	Varies irregularly with wavelength.
Descriptive Properties		
CAS Number	7440-21-3	Diamond Structure - Space Group Fd3m
Crystal Structure	Cubic	
Solubility	Insoluble in H_2O and Acid; Soluble in Alkaline	

Alumina (Al_2O_3), 99.9%

A more detailed and complete data, including temperature dependence spectra, can be found at http://www.ioffe.ru/SVA/NSM/Semicond/index.html.

Physical Properties	Metric	Comments
Density	3.96 g/cc	
Water Absorption	0 %	
a Lattice Constant	4.7591 Å	
c Lattice Constant	12.9894 Å	
Formula Units/Cell (Z)	6	
Molecular Weight	101.961 g/mol	
Weibull Modulus	Min 10	
Mechanical Properties		
Hardness, Knoop	1700 - 2200	
Hardness, Vickers	1365	
Vickers Microhardness	2085	
Hardness, Mohs	9	
Abrasive Hardness	1000	
Drilling Hardness	188808	
Tensile Strength, Ultimate	300 MPa	
Modulus of Elasticity	370 GPa	
Flexural Strength	400 MPa	
Compressive Yield Strength	3000 MPa	at 25°C; 1900 MPa at 1000°C
Poisson's Ratio	0.22	
Fracture Toughness	4 MPa-m½	
Shear Modulus	150 GPa	

Electrical Properties		
Electrical Resistivity	1e+014 ohm-cm	
Electrical Resistivity at Elevated Temperature	2.5e+006 ohm-cm	at 900°C
Magnetic Susceptibility	-3.7e-005	cm^3/mol
Dielectric Constant	9.9	
Dielectric Strength	10 kV/mm	Wide Variation Between Grades
Thermal Properties		
Heat of Fusion	1092.6 J/g	
CTE, linear 250°C	7.4 μm/m-°C	25-400°C
CTE, linear 1000°C	8.2 μm/m-°C	20-1000°C
Specific Heat Capacity	0.85 J/g-°C	
Thermal Conductivity	30 W/m-K	
Thermal Conductivity at Elevated Temperature	6.3 W/m-K	at 800°C
Melting Point	2054 °C	
Boiling Point	3000 °C	
Maximum Service Temperature, Air	1750 °C	No Load
Optical Properties		
Refractive Index	1.761	ω, Na
Refractive Index	1.769	η, Na
Descriptive Properties		
Colour	White	
Crystal Structure	Rhombohedral	Corundum

Annex II

Table of the deposition parameters

Series	Type of substrates	Base Pressure (mbar)	Power (Watt)	Deposi-tion time (min.)	Argon Pressure (mbar)	h (mm)	Subst. temp. (ºC)	Target Config. (1)
Al₂O₃ films								
AA	**Glass and FS**	**1.0×10^{-5}**	**50**	**255**	**5.5×10^{-3}**	**60**	**500**	**-**
AB	**Glass and Si(111)**	**4.0×10^{-6}**	**80**	**245**	**5.8×10^{-3}**	**60**	**500**	**-**
AC	**Glass and Si(111)**	**9.0×10^{-3}**	**50**	**270**	**4.0×10^{-3}**	**60**	**500**	**-**
AD	**Glass**	**1.5×10^{-5}**	**80**	**146**	**4.0×10^{-3}**	**60**	**500**	**-**
AE	**Glass and Si(111)**	**3.0×10^{-5}**	**80**	**180**	**2.0×10^{-3}**	**60**	**500**	**-**
AQ	Glass and Si(111)	3.5×10^{-6}	80	120	6.0×10^{-3}	60	100	-
AR	Glass and Si(111)	$<6 \times 10^{-6}$	50	240	5.8×10^{-3}	60	500	-
AS	Glass and Si(111)	3.5×10^{-6}	50	240	4.0×10^{-3}	60	500	-
AT	Glass and Si(111)	$<3 \times 10^{-6}$	50	240	2.0×10^{-3}	60	500	-
AU	Glass and Si(111)	3.0×10^{-6}	80	60	4.0×10^{-3}	60	100	-
AV	Glass and Si(111)	3.0×10^{-6}	81	240	4.0×10^{-3}	60	500	-
AX	Glass and Si(111)	2.5×10^{-6}	100	240	4.0×10^{-3}	60	500	-
AZ	Glass and Si(111)	2.5×10^{-6}	80	120	4.0×10^{-3}	60	250	-
BA	Glass and Si(111)	3.0×10^{-6}	80	45	4.0×10^{-3}	60	100	-
BB	Glass and Si(111)	8.0×10^{-6}	80	120	4.0×10^{-3}	60	100	-
Thin_Al₂O₃-1	Si(100) 2" p-type	3.0×10^{-6}	80	10	4.0×10^{-3}	60	80	-
Thin_Al₂O₃-2	Si(100) 2" n-type	3.5×10^{-6}	50	2	4.0×10^{-3}	60	80	-
Thin_Al₂O₃-3	Si(100) 2" n-type	2.0×10^{-6}	50	4	4.0×10^{-3}	60	80	-
Thin_Al₂O₃-4	Si(100) 2" n-type	$<3 \times 10^{-6}$	80	4	4.0×10^{-3}	60	80	-
Thin_Al₂O₃-5	Si(100) 2" n-type	3.0×10^{-6}	50	10	4.0×10^{-3}	60	80	-
Thin_Al₂O₃-6	Si(100) 2" n-type	2.0×10^{-6}	80	2	4.0×10^{-3}	60	80	-
Thin_Al₂O₃-7	Si(100) 2" n-type	2.0×10^{-6}	120	2	4.0×10^{-3}	60	80	-
Thin_Al₂O₃-8	Si(100) 2" n-type	1.0×10^{-6}	80	4	8.0×10^{-3}	60	80	-
Thin_Al₂O₃-9	Si(100) 2" n-type	5.0×10^{-7}	80	4	2.0×10^{-3}	60	80	-
Ge doped Al₂O₃ films								
A	Glass	3.0×10^{-6}	50	230	5.8×10^{-3}	60	100	1
B	Glass	1.0×10^{-6}	80	240	5.8×10^{-3}	60	100	1
C	Glass	1.0×10^{-6}	80	240	5.8×10^{-3}	60	RT	2
D	Glass	5.0×10^{-7}	80	240	5.8×10^{-3}	60	100	2
E	Glass	8.0×10^{-7}	50	230	5.8×10^{-3}	60	100	2
F	Glass	5.0×10^{-7}	50	230	5.8×10^{-3}	60	500	2
G	Glass	$- \times 10^{-5}$	50	230	1.0×10^{-2}	60	100	2

H	**Glass**	1.0×10^{-6}	**50**	**240**	$\mathbf{5.8 \times 10^{-3}}$	**60**	**100**	**3**
I	Glass and FS	$- \times 10^{-6}$	50	240	1.0×10^{-2}	60	100	3
J	**Glass and FS**	$- \times 10^{-5}$	**50**	**240**	$\mathbf{5.8 \times 10^{-3}}$	**60**	**500**	**3**
K	Glass and FS	5.0×10^{-7}	80	270	5.8×10^{-3}	60	100	3
O	**Glass, FS and Si(111)**	3.0×10^{-6}	**50**	**255**	$\mathbf{4.0 \times 10^{-3}}$	**60**	**500**	**3**
P	**Glass, FS and Si(111)**	1.0×10^{-6}	**50**	**255**	$\mathbf{2.0 \times 10^{-3}}$	**60**	**500**	**3**
T [1]	**Glass and Si(111)**	1.0×10^{-6}	**50**	**270**	$\mathbf{4.0 \times 10^{-3}}$	**60**	**500**	**3**
U [2]	**Glass and Si(111)**	4.5×10^{-6}	**80**	**270**	$\mathbf{4.0 \times 10^{-3}}$	**60**	**500**	**3**
V [3]	**Glass and Si(111)**	1.5×10^{-6}	**50**	**240**	$\mathbf{3.0 \times 10^{-3}}$	**60**	**500**	**3**
X [3]	**Glass and Si(111)**	1.0×10^{-6}	**80**	**270**	$\mathbf{4.0 \times 10^{-3}}$	**60**	**500**	**3**
Z [1]	**Glass and Si(111)**	6.0×10^{-6}	**50**	**255**	$\mathbf{5.0 \times 10^{-3}}$	**60**	**500**	**3**
AF	**Glass and Si(111)**	7.5×10^{-7}	**100**	**120**	$\mathbf{4.0 \times 10^{-3}}$	**60**	**500**	**3**
AG	**Glass and Si(111)**	1.0×10^{-6}	**60**	**270**	$\mathbf{4.0 \times 10^{-3}}$	**60**	**500**	**3**
AH	**Glass and Si(111)**	2.0×10^{-6}	**40**	**240**	$\mathbf{4.0 \times 10^{-3}}$	**60**	**500**	**3**
AI	Glass and Si(111)	1.0×10^{-6}	50	120	5.0×10^{-3}	60	500	3
AJ	Glass and Si(111)	1.0×10^{-6}	50	120	5.0×10^{-3}	60	500	3
AK	Glass and Si(111)	4.0×10^{-6}	80	120	6.0×10^{-3}	60	100	3
AL	Glass and Si(111)	9.0×10^{-6}	80	120	2.0×10^{-3}	60	100	3
AM	Glass and Si(111)	8.0×10^{-6}	80	130	4.0×10^{-3}	60	100	3
AN	Glass and Si(111)	7.0×10^{-7}	80	35	4.0×10^{-3}	60	100	3
AO	Glass and Si(111)	2.0×10^{-6}	79	120	4.0×10^{-3}	60	400	3
AP	Glass and Si(111)	7.0×10^{-7}	80	135	4.0×10^{-3}	60	250	3
BD	**Glass and Si(111)**	1.0×10^{-6}	**50**	**270**	$\mathbf{4.0 \times 10^{-3}}$	**60**	**500**	**3**
BE	Si(100) 2" Wafer	3.0×10^{-7}	50	10	4.0×10^{-3}	60	R.T.	3
BF	Si(100) 2" Wafer	5.0×10^{-7}	50	20	4.0×10^{-3}	60	R.T.	3
BG	Si(100) 2" Wafer	5.0×10^{-7}	50	30	4.0×10^{-3}	60	R.T.	3
BH	Si(100) 2" Wafer	5.0×10^{-7}	50	60	4.0×10^{-3}	60	R.T.	3
BI	Si(100) 2" Wafer	6.0×10^{-7}	50	60	4.0×10^{-3}	60	500	3
BJ	Si(100) 2" Wafer	5.0×10^{-7}	80	49	4.0×10^{-3}	60	500	3
BK	Si(100) 2" Wafer	4.0×10^{-7}	50	5	4.0×10^{-3}	60	R.T.	3
BL	Si(100) 2" Wafer	6.0×10^{-7}	50	10	8.0×10^{-3}	60	R.T.	3
BM	Glass and Si(111)	7.0×10^{-7}	50	90	4.0×10^{-3}	60	R.T.	3
BN	**Glass and Si(111)**	7.0×10^{-7}	**50**	**240**	$\mathbf{8.0 \times 10^{-3}}$	**60**	**500**	**3**
BO	Glass and Si(111)	4.0×10^{-7}	50	240	4.0×10^{-3}	60	250	3

[1] After deposition, sample was kept at 500ºC during 30 minutes before start cooling.
[2] After deposition, sample was kept at 500ºC during 40 minutes before start cooling.
[3] After deposition, samples were kept at 500ºC during 12 hours before start cooling.

Annex III

Table of the annealing parameters

Samples Name		Type of Subst.	Annealing parameters			
Before Annealing	After Annealing		**Temp.**	**Time** [1]	**Type of gas**	**Gas flow Pressure**
			(ºC)	(min.)		(mbar)
Al$_2$O$_3$ films						
AC12Si	AC12SiR	Si(111)	800	60	Air	<1.0×10^{-5}
AC22Si	**AC22SiR**	**Si(111)**	**800**	**60**	**Air**	**1.5×10^{-2}**
AC22SiR	**AC22SiR2**	**Si(111)**	**900**	**120**	**Air**	**1.4×10^{-2}**
AC22SiR2	**AC22SiR3**	**Si(111)**	**1000**	**450**	**Air**	***Atm.***
AE22Si	**AE22SiR**	**Si(111)**	**800**	**60**	**Air**	**1.5×10^{-2}**
AE22SiR	**AE22SiR2**	**Si(111)**	**900**	**240**	**Air**	**1.4×10^{-2}**
AE22SiR2	**AE22SiR3**	**Si(111)**	**1000**	**450**	**Air**	***Atm.***
AV12Si	AV12SiR	Si(111)	800	60	Air	<1.0×10^{-5}
AV21Si	AV21SiRA	Si(111)	800	60	Argon	2.4
AV21Si	AV21SiRN2	Si(111)	800	60	Nitrogen	2.4
AV23Si	AV23SiR2	Si(111)	900	60	air	8.0×10^{-6}
AR22Si	AR22SiR	Si(111)	800	60	air	<1.0×10^{-5}
Ge doped Al$_2$O$_3$ films						
F12	F12R	Glass	550	120	Air	3.3×10^{-3}
F22	F22R	Glass	580	60	Air	3.3×10^{-3}
H12	H12R	Glass	580	230	Air	3.3×10^{-3}
H21	H21R	Glass	560	240	Air	5.3×10^{-3}
H22	**H22R**	**Glass**	**580**	**60**	**Air**	**3.3×10^{-3}**
I12	I12R	Glass	580	230	Air	3.3×10^{-3}
J12	J12R	Glass	550	120	Air	3.3×10^{-3}
K12	K12R	Glass	550	120	Air	3.3×10^{-3}
O11	O11R	Glass	550	120	Air	3.3×10^{-3}
O12Si	**O12SiR**	**Si(111)**	**800**	**60**	**Air**	**4.6×10^{-3}**
O21	O21R	Glass	560	240	Air	5.3×10^{-3}
O23	O23R	Glass	550	120	Air	3.3×10^{-3}
P11	P11R	Glass	550	120	Air	3.3×10^{-3}

P12Si	P12SiR	Si(111)	800	60	Air	4.6×10^{-3}
T12Si	T12SiRAr	Si(111)	800	60	Argon	2.4
T21Si	T21SiR1N$_2$	Si(111)	800	60	Nitrogen	4.7
T22Si	T22SiR	Si(111)	800	60	Air	2.9×10^{-3}
U12Si	U12SiR	Si(111)	800	60	Air	2.9×10^{-3}
U21Si	**U21SiRAr**	**Si(111)**	**800**	**60**	**Argon**	**2.4**
U21Si	U21SiR1N$_2$	Si(111)	800	60	Nitrogen	4.6
U22Si	**U22SiR**	**Si(111)**	**800**	**60**	**Air**	**4.6×10^{-3}**
V12Si	V12SiR	Si(111)	800	60	Air	2×10^{-5}
V12Si	V12SiRAr	Si(111)	800	60	Argon	5×10^{-3}
V22Si	**V22SiR**	**Si(111)**	**800**	**60**	**Air**	**4.6×10^{-3}**
V22Si	**V22SiRAr**	**Si(111)**	**800**	**60**	**Argon**	**5×10^{-3}**
V21Si	V21SiR1N$_2$	Si(111)	800	60	Nitrogen	4.6
V21Si	**V21SiR2N$_2$**	**Si(111)**	**900**	**60**	**Nitrogen**	**6.0**
X22Si	X22SiR	Si(111)	800	60	Air	4.6×10^{-3}
X23Si	X23SiR1N$_2$	Si(111)	800	60	Nitrogen	4.6
X23Si	X23SiR2N$_2$	Si(111)	900	60	Nitrogen	6.0
X32Si	**X32SiRAr**	**Si(111)**	**800**	**60**	**Argon**	**5×10^{-3}**
Z21Si	Z21SiR1N$_2$	Si(111)	800	60	Nitrogen	4.7
Z21Si	Z21SiR2N$_2$	Si(111)	900	60	Nitrogen	6.0
Z22Si	**Z22SiR**	**Si(111)**	**800**	**60**	**Air**	**4.6×10^{-3}**
AF22Si	AF22SiR	Si(111)	800	60	Air	1.5×10^{-2}
AF22Si	AF22SiR2N$_2$	Si(111)	900	60	Nitrogen	6.0
AG22Si	AG22SiR	Si(111)	800	60	Air	1.5×10^{-2}
AG22Si	AG22SiR2N$_2$	Si(111)	900	60	Nitrogen	6.0
AH22Si	AH22SiR	Si(111)	800	60	Air	1.6×10^{-2}
AI21Si	AI21SiR	Si(111)	800	60	Air	1.6×10^{-2}
AJ21Si	AJ21SiR	Si(111)	800	60	Air	1.6×10^{-2}
AK22Si	AK22SiR2N$_2$	Si(111)	900	60	Nitrogen	6.0
AL22Si	AL22SiR2N$_2$	Si(111)	900	60	Nitrogen	6.0
AM22Si	AM22SiR	Si(111)	800	60	Air	1.4×10^{-2}
AO22Si	AO22SiR	Si(111)	800	60	Air	1.4×10^{-2}

AP22Si	AP22SiR	Si(111)	800	60	Air	1.4×10^{-2}
BD12Si	BD12SiR	Si(111)	800	67	Air	*Atm.*
BD12Si	BD12SiR2	Si(111)	800	60	Air	$1.0<P<2.0\times10^{-4}$
BD12Si	BD12SiR3	Si(111)	800	60	Air	1.0×10^{-5}
BD21Si	BD21SiR	Si(111)	800	60	Air	2×10^{-5}
BD22Si	**BD22SiR**	**Si(111)**	**800**	**60**	**Air**	$\mathbf{2\times10^{-5}}$
BD22Si	**BD22SiR2**	**Si(111)**	**900**	**60**	**Air**	$\mathbf{8.0\times10^{-6}}$
BD22Si	BD22SiR3	Si(111)	800	60	Air	$5.0x\ 10^{-3}$
BN12Si	BN12SiR	Si(111)	800	67	Air	*Atm.*
BN12Si	BN12SiR2	Si(111)	800	60	Air	$1.0<P<2\times10^{-4}$
BN12Si	BN12SiR3	Si(111)	800	60	Air	1.0×10^{-5}
BN22Si	**BN22SiR**	**Si(111)**	**800**	**60**	**Air**	$\mathbf{2\times10^{-5}}$
BN22Si	**BN22SiR2**	**Si(111)**	**900**	**60**	**Air**	$\mathbf{8.0\times10^{-6}}$
BN22Si	BN22SiR3	Si(111)	800	60	Air	$5.0x\ 10^{-3}$
BO12Si	BO12SiR	Si(111)	800	67	Air	*Atm.*
BO12Si	BO12SiR2	Si(111)	800	60	Air	$1.0<P<2\times10^{-4}$
BO12Si	BO12SiR3	Si(111)	800	60	Air	1.0×10^{-5}
BO22Si	BO22SiR	Si(111)	800	60	Air	2×10^{-5}
BO22Si	BO22SiR2	Si(111)	900	60	Air	8.0×10^{-6}
BO22Si	BO22SiR3	Si(111)	800	60	Air	$5.0x\ 10^{-3}$

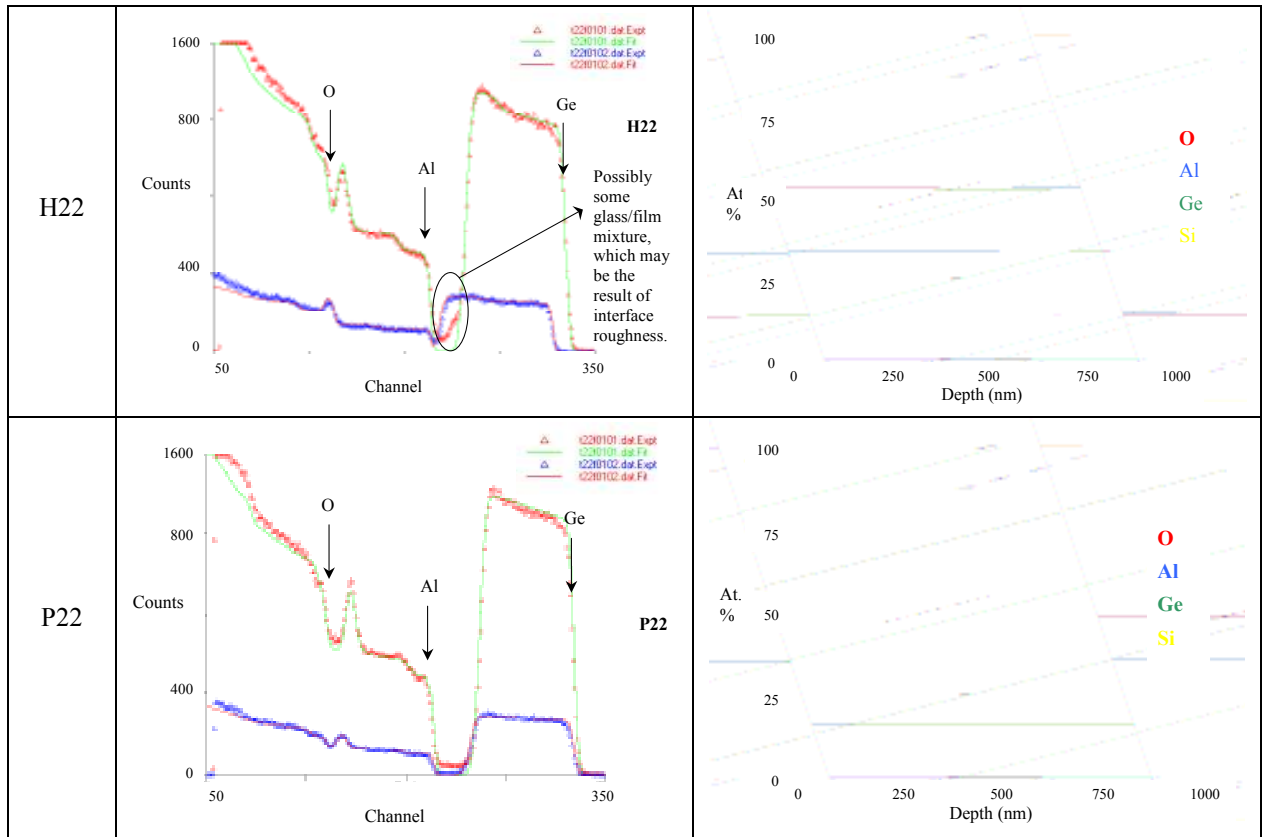[1] Annealing time refers only to time at which samples were kept at constant temperature. We must not forget that samples were maintained in the same position (inside the quartz tube) during heating and cooling processes (see the annealing ramp of figure 2.13).

Annex IV

RBS spectra

Sample	RBS spectra	Simulation results
T22Si		
U21Si		
U22Si		
U33Si		

H22		
P22		
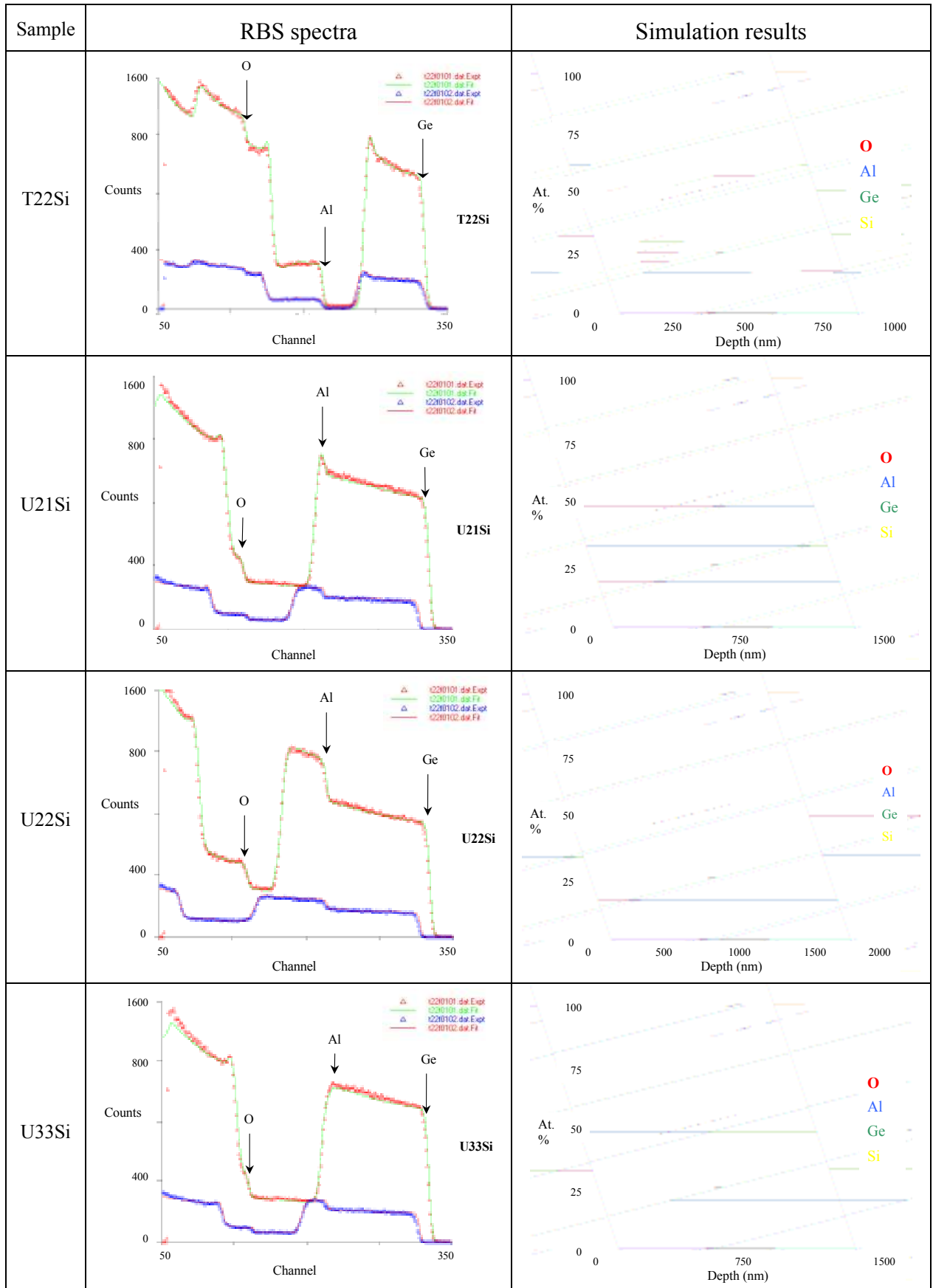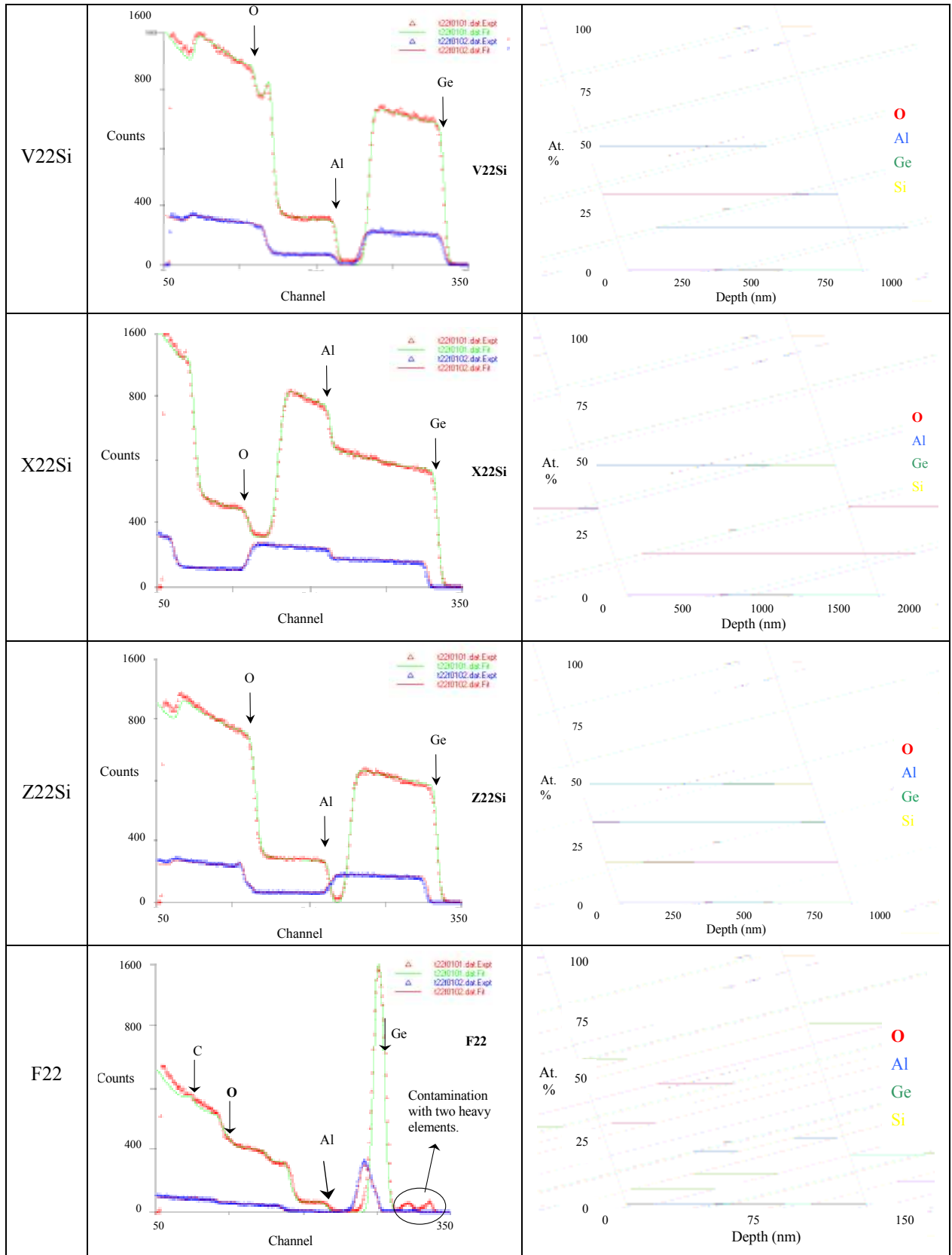
Annex V

XPS survey spectrum

Sample X22 Survey – Elements Identification

Peak Label/ID	Atomic %	BE (eV)
O 1s	38.8%	532.00
C 1s	29.6%	285.00
Al 2p	22.3%	75.00
Ge 3d	9.2%	30.00
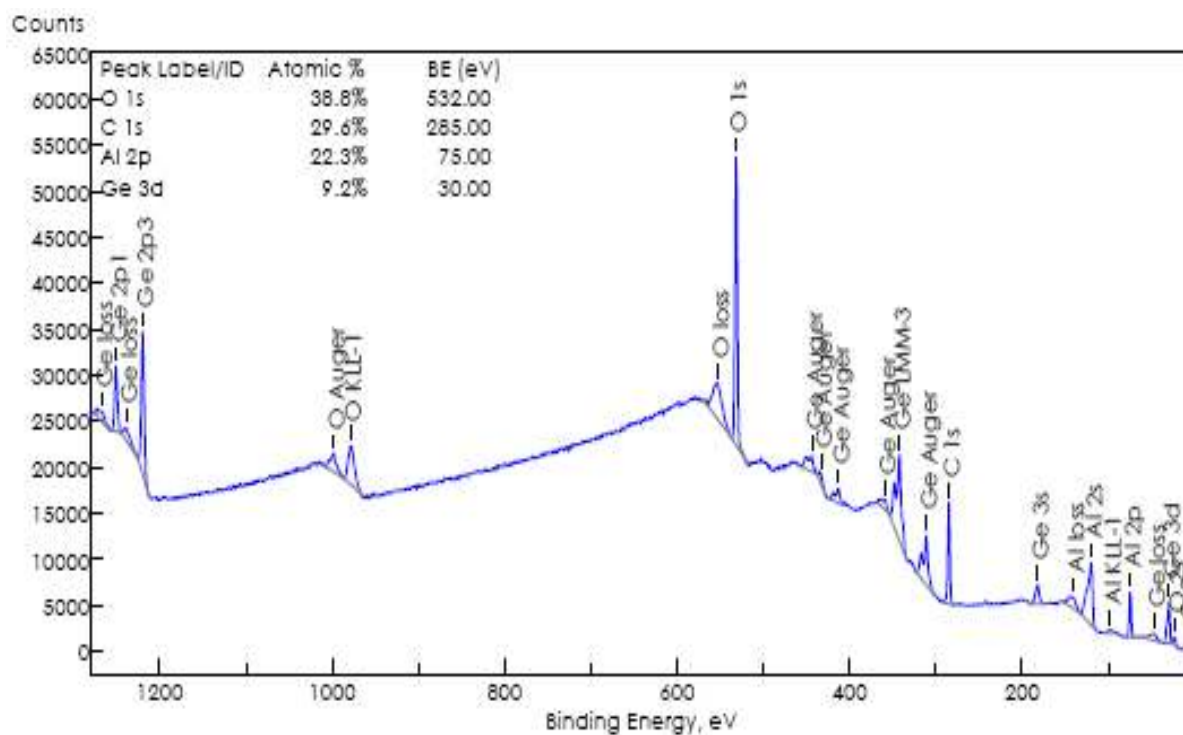
Annex VI

Table with the Ge NCs average size

(Estimated by the XRD spectra using Debye-Scherrer formula)

Ge NCs mean diameter (*D*) estimated after determining the FWHM of the X-ray diffraction peaks for each of the c-Ge reflection planes						
Sample name	*(111)*	*(220)*	*(311)*	*(400)*	*(331)*	*D* (nm)
O1.2SiR #	5,215	4,571	5,137	5,451	3,743	4,82
U2.1Si	-	1,804	2,408	-	-	2,11
U2.2Si	-	3,365	1,567	-	-	2.47
U2.2SiR	6,290	6,691	7,608	-	-	6,86
U1.2SiR	-	5,663	7,377	-	-	6,52
U1.2SiR #	6,773	6,217	7,094	6,880	3,061	6,00
V2.2Si #	1,290	-	-	-	-	1.29
V2.2SiR #	5,049	4.783	4,804	5.694	4.546	4,98
V2.2SiR	-	4,832	5,342	-	-	5,09
X2.2SiR	6,542	5,059	7,497	-	-	6,37
X32SiRAr	-	23,641	21,066	-	-	22,35
Z22Si	-	3,032	-	-	-	3,03
Z2.2SiR	-	5,180	5,413	-	-	5,30
Z2.2SiR #	6,376	4,984	5,491	6,569	4,248	5,53
AH22Si	-	2,507	2,806	-	-	2,66
BD2.2SiR	-	4,723	8,847	-	-	6,79
BD2.2SiR2	-	3,987	10,272	-	-	7,13
BN22SiR	-	4,644	8,847	-	-	6,75
BN22SiR2	-	6,381	14,433	-	-	10,41

Note – Values presented on the above table were calculated based on the samples XRD spectra applying the Debye-Scherrer formula (Eq.2.1) for each of the reasonable peaks. Samples marked with # correspond to those on which GIXRD was performed.